Extending the lifetime of hyperpolarisation

THÈSE Nᵒ 7873 (2017)

ÉCOLE POLYTECHNIQUE FÉDÉRALE DE LAUSANNE

POUR L'OBTENTION DU GRADE DE DOCTEUR ÈS SCIENCES

PAR

Xiao JI

acceptée sur proposition du jury:

Prof. S. Gerber, présidente du jury
Prof. G. Bodenhausen, Prof. J.-Ph. Ansermet, directeurs de thèse
Prof. S. JANNIN, rapporteur
Prof. M. Ernst, rapporteur
Prof. L. HELM, rapporteur

EPFL

ÉCOLE POLYTECHNIQUE
FÉDÉRALE DE LAUSANNE

Suisse
2017

读博士，最深刻的感受在于
「自己仿佛在荒原上漫游」

没有人知道这条路通向哪里
也没有人知道这条路有没有尽头

To my family...
献给我的家人......

Abstract

In nuclear magnetic resonance (NMR), one of the most serious inherent challenges is the low sensibility of nuclear transitions. In order to enhance the signal of NMR experiments, the technique of dynamic nuclear polarisation (DNP) was introduced in the 1950s, leading to a high field prototype apparatus in the 1990s for solid-state applications under MAS conditions. In 2003, the coupling between low-temperature polarisation and room temperature detection also came into reality, which is known as dissolution-DNP (d-DNP). In this thesis, we present a new sample formulation for d-DNP experiments. Also, a new scheme for separating the preparation of hyperpolarised materials from the detection apparatus is proposed, which would allow us to overcome the usual requirement that the apparatus for hyperpolarisation and the device for signal detection have to be in close proximity.

A numerical model based on the finite element method (FEM) is proposed to study the dynamics of nuclear magnetic energy in both conventional spin glasses and biphasic d-DNP samples. This method permits a visualisation of the process of the build-up of polarisation and of the relaxation of magnetisation during a DNP experiment. Based on such calculations, we could estimate the optimal experimental parameters for the preparation of hyperpolarised samples, including but not limited to the chemical composition of the samples, the length of spin locking pulses, and the duration of intervals between spin locking pulses in pulse sequences.

An interesting conclusion from our simulations is that, under suitable conditions of storage, the lifetime of the hyperpolarisation can be extended to hours or even days in carefully designed biphasic samples. This allows us to propose two experimental approaches aiming at drawing benefit from such an attenuated relaxation.

One method deals with molecules of interest (MOIs) that are in crystalline form at room temperature and normal pressure. Such powders can be impregnated with radical-doped organic glass-forming solvents that have an orthogonal solubility. Under DNP conditions, the magnetisation is transferred from the single electron of the polarising agent (PA) to the nuclei in glassy organic solvents. The nuclear polarisation is then relayed to the particles of MOI. We can further confine the nuclear hyperpolarisation overnight in a moderate static magnetic field in a liquid helium bath.

On the other hand, for MOIs that are liquid or even gaseous at room temperature and normal pressure, we propose a spin-labelled solid matrix with interconnecting pores. The fluids can be filled into the pores of the matrix. Under DNP conditions, the

DNP process begins from the bulk of the polarising matrix, and then passes to the fluids that are frozen in the pores.

Résumé

Un des inconvénients inhérents de la résonance magnétique nucléaire (RMN) est la faible sensibilité des transition des noyaux. La polarisation nucléaire dynamique a été introduite en vue d'augmenter l'intensité des signaux de la RMN dans les années cinquante. Un prototype à hauts champs pour des applications dans l'état solide fut réalisé au début des années 1990. Puis il devint possible de combiner la polarisation à basse température et la détection des signaux à température ambiante dès 2003 sous le nom de polarisation nucléaire dyamique par dissolution *PND-d* pour *dissolution-DNP*. Dans ce manuscrit, nous présentons une nouvelle méthode de la prépatarion des échantillons pour les expériences de type *PND-d*. Nous montrons aussi une nouvelle approche qui permet de coupler la préparation de matériaux hyperpolarisés et les appareils de détection sans exiger la proximité physique de du polariseur et du détecteur.

Un modèle numérique par éléments finis est proposé pour l'étude de la dynamique de l'énergie magnétique nucléaire dans un échantillon classique vitreux ainsi que dans une formulation biphasique. Ces simulations nous permettent de visualiser non seulement la montée en polarisation mais encore la relaxation de la polarisation nucléaire tout au long du processus de *DNP*. Avec les résultats de ces calculs, on peut envisager une optimisation des paramètres expérimentaux, tels que la constitution chimique d'un échantillon, la durée de l'impulsion, ou bien la longeur de l'intervalle entre des verrouillqges des spins dans une séquence.

D'après les simulations, nous avons trouvé que, dans des conditions appropriées, le temps de vie de l'hyperpolarisation d'un échantillon biphasique peut être prolongé à plusieurs heures, voire même à plusieurs jours. Deux approches sont démontrées qui permettent de profiter de cette relaxation ralentie.

Dans la première approche, les molécules d'intérêt sont sous forme cristalline à température ambiante et pression normale. Les poudres de ces molécules sont imprégnées avec des liquides contenant des radicaux qui forment un verre à basse température, dont le solvant possède une solubilité orthogonale par rapport à celle des poudres des molécules d'intérêt. Sous conditions de *DNP*, le transfert de l'aimantation intrevient d'abord entre les spins électroniques de l'agent polarisant et les noyaux du solvant. Dans un deuxième temps, une redistribution spatiale de l'énergie magnétique des noyaux se produit à travers l'échantillon, ce qui donne lieu à une accumulation de l'énergie magnétique nucléaire dans les cristaux contenant les molécule d'intérêt. Une fois polarisés, ces poudres peuvent conserver leur aimantation nucléaire dans

un champ magnétique modéré dans un bain de l'hélium liquide pendant plus de 12 heures.

Pour conserver la polarisation dans des substances à l'état liquide ou gazeux à température ambiante, nous avons développé une matrice poreuse dopée de radicaux. Les fluides peuvent pénétrer dans les pores au sein de ces matrices. Après la solidification de ces fluides à basse température, les molécules d'intérêt peuvent être polarisées par la matrice par diffusion de spin.

Mots clefs: RMN, PND, la formulation d'échantillons, diffusion de spin, simulation numérique

Contents

Contents

Contents

List of Abbreviations

μw microwave.

CP cross polarisation.

d-DNP dissolution DNP.

DNP dynamic nuclear polarisation.

ESR electron spin resonance.

FEM finite element method.

MAS magic-angle spinning.

MOI molecule of interest.

MRI magnetic resonance imaging.

NMR nuclear magnetic resonance.

PA polarising agent.

RF radio frequency.

RFP radical free phase.

RRP radical rich phase.

TEMPO (2,2,6,6-tetramethylpiperidin-1-yl)oxidanyl.

1 Introduction

1.1 Scope of This Work

Since Overhauser and Slichter first demonstrated the possibility of hyperpolarising nuclear spins in metals by transferring the magnetisation from conducting electrons in the vicinity as a source [1, 2, 3, 4], the concept of Dynamic Nuclear Polarisation (DNP) has become one of the most interesting aspects in the community of modern NMR. An important reason is that the magnetisation of nuclear spins could thus be enhanced with respect to its thermal equilibrium by a factor given by the ratio of the gyromagnetic ratios between electronic spin and the nuclear spins, γ_{e^-}/γ_n, which is of 2 orders of magnitude. The coupling of DNP and NMR/MRI therefore attracts the attention of the whole community, because of the large enhancement in sensitivity.

In the field of modern high field NMR, the microwave-driven DNP technique was first coupled with solid-state NMR by Griffin's group under MAS conditions in the 1990s [5]. The DNP-MAS technique was then further promoted in the fields of structural biology [6, 7, 8, 9], surface chemistry[10, 11, 12, 13, 14, 15, 16, 17, 18], inorganic materials [19, 20, 21], pharmaceutical industry[22, 23], and many other fields.

On the other hand, in 2003, Jan Henrik Ardenkjær-Larsen *et al.* reported the breakthrough on coupling low temperature DNP with room temperature liquid state NMR[24, 25], which is named as dissolution-DNP (d-DNP). A standard d-DNP system usually consists of two independent superconducting magnets. One serves as a polariser, aiming at hyperpolarising the molecules of interest (MOI). The other magnet operates at room temperature and serves as detector for NMR/MRI experiments[26, 27, 28, 29]. As we know, after hyperpolarisation, the huge magnetisation generated in the polariser relaxes at the rate of longitudinal relaxation. Though various schemes have been proposed to fight this fast decay [30], the physical distance between the polariser and the detection apparatus has to be as small as possible.

The complexity of the whole d-DNP system hampers the general applications of

this promising technique. First, because the lab needs be equipped with a sophisticated and expensive polarizing system. Second, because the system involves low temperatures (1.2-4.2 K) and requires trained scientists with special expertise.
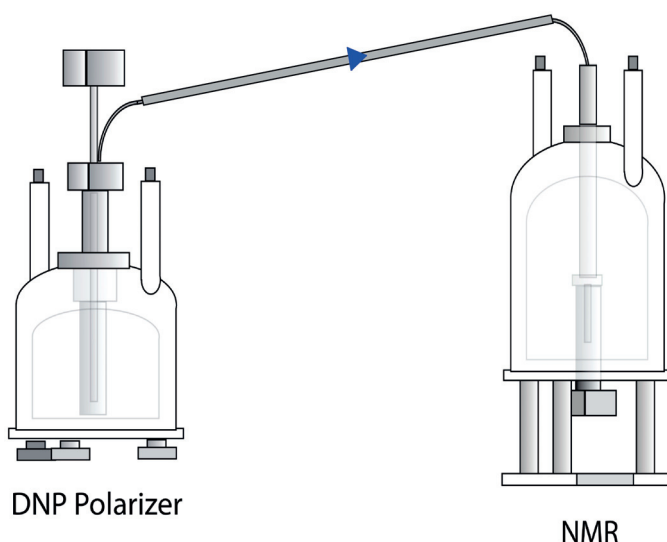
Figure 1.1 – An illustration of the conventional spatial coupling between DNP polariser and the liquid-state NMR apparatus. The blue triangle indicates the direction of the transfer of the hyperpolarised fluid after dissolution. The thick straight tube between the polariser and the NMR apparatus represents the magnetic tunnel of transport. (Cited from [31])

In order to broaden the access to the d-DNP technique and extend its audience, it is our primary objective to develop a scheme in which a spatial decoupling between the polariser and the detection apparatus is possible. Inspired by the impregnation method in the sample preparation of MAS-DNP and d-DNP experiments[7, 13, 16, 22, 32], we proposed a biphasic sample formulation for d-DNP experiments.

The central goal of this thesis is to visualise the practice of *Transportable D-DNP with Biphasic Samples*. A strong emphasis is put on the study of the redistribution of hyperpolarisation between different phases and different nuclear spins. In particular, simulations based on the Finite Element Method (FEM) are introduced to predict the flow of magnetic energy within the network of protons and carbons, in analogue with respect to the diffusion of thermal energy during heat transfer.

To begin with, we present a short comparison between two sample formulations, the homogeneous spin glass with MOI as solute, and the heterogeneous mixture with the MOI as a separate phase.

In the chapter 2, we consider the FEM approach for the simulation of diffusion in a biphasic sample under DNP conditions. First, we demonstrate how the spin diffusion can be linked with the mathematical models of the flow of magnetic energy inside the sample with the help of spin-temperature theory. Then we illustrate some numerical results on the dynamics of DNP build-up, of cross-polarisation, and of nuclear relaxation in the biphasic sample. The results discussed in chapter 2 shall be used to guide our experimental application of the biphasic formulation in d-DNP experiments.

Based on the calculations presented in chapter 2, we developed two different biphasic approaches to transportable hyperpolarisation. The first approach focuses on polarising the MOI in crystalline form by impregnation of a solution of polarising agent, which we shall describe in chapter 4. In the chapter 5, we are to deal with another approach opposite to the chapter 4, that is, to polarise a liquid using a solid porous polarising matrix.

1.2 Some Basic Concepts

In the following section, we briefly introduce some concepts used in NMR and in DNP, especially those encountered in the thermodynamic description of DNP process. Details can be found in the general text books on magnetic resonance [33, 34, 35, 36, 37, 38].

1.2.1 NMR Part

Density Operator

From the quantum mechanical point of view, we can characterize the state of an system of spins by the density operator of the system, which is defined as:

$$\hat{\rho}(t) \overset{def}{=\!=} \sum_i p_i(t)|\boldsymbol{\phi}_i\rangle\langle\boldsymbol{\phi}_i| \tag{1.1}$$

where $\hat{\rho}(t)$ is the density operator of the system at the moment t, $\boldsymbol{\phi}_i$ is the function that depicts the ith state of the system, and p_i is the probability of observing the ith state of the system.

The diagonal terms of the density operator are called the populations terms, and the off-diagonal terms are the coherence terms.

Evolution of the System

For a system with an initial condition defined by the density operator $\hat{\rho}(0)$, we can claim that it stays in its initial state, if it is not exposed to any interactions.

Otherwise, the dynamics of the system, or of the density operator, is determined by the *quantum mechanical master equation*:

$$\frac{d}{dt}\hat{\rho}(t) = -i\left[\hat{\mathbf{H}}(t), \hat{\rho}(t)\right] - \hat{\hat{\mathbf{R}}}\left(\hat{\rho}(t) - \hat{\rho}_{eq}\right) \tag{1.2}$$

where $\hat{\mathbf{H}}(t)$ is the spin Hamiltonian, representing all the coherent interactions that influence the system, $\hat{\hat{\mathbf{R}}}$ is the relaxation superoperator that treats the interaction between the spin system and the lattice, and the term $\hat{\rho}_{eq}$ is the time-independent density operator in the equilibrium state.

Hamiltonian of the System

Consider a two-spin system, where there is an electron, spin $\hat{\boldsymbol{E}}$, and nuclear spin $\hat{\boldsymbol{N}}$. For simplicity we can write the total stationary Hamiltonian of the system ($\hat{\mathbf{H}}_{Tot}$) as the sum of all major interactions in the laboratory frame in the system:

$$\hat{\mathbf{H}}_{Tot} = \hat{\mathbf{H}}_Z + \hat{\mathbf{H}}_D + \hat{\mathbf{H}}_{HF} + \hat{\mathbf{H}}_{Other} + \hat{\mathbf{H}}_{RF} + \hat{\mathbf{H}}_{\mu w} \tag{1.3}$$

in which $\hat{\mathbf{H}}_Z$ represents all the Zeeman interactions between the main static magnetic field and the spin, $\hat{\mathbf{H}}_D$ refers to all the dipolar coupling terms among spins in the system, $\hat{\mathbf{H}}_{HF}$ is for the hyperfine interactions that couple the electronic spins with the nuclei, and $\hat{\mathbf{H}}_{Other}$ includes all the other major interactions in the system, such as nuclear quadrupolar interaction, electronic zero-field splitting, and so on. The last term is for the radiofrequency pulses and microwave irradiation.

Zeeman interactions   The total Zeeman Hamiltonian is the sum of Zeeman interaction among all the spins that are placed in the static magnetic field, $\mathbf{B}_0$, both electrons, $\hat{\mathbf{H}}_{Z,e}$, and nuclei, $\hat{\mathbf{H}}_{Z,n}$:

$$\hat{\mathbf{H}}_{Z,tot} = \hat{\mathbf{H}}_{Z,e} + \hat{\mathbf{H}}_{Z,n} \tag{1.4}$$

$$= -\sum_i \gamma_e \mathbf{B}_0 \cdot \mathbf{g}_i \cdot \hat{\mathbf{E}} - \sum_k \gamma_n \mathbf{B}_0 \cdot \boldsymbol{\delta}_k \cdot \hat{\mathbf{N}} \tag{1.5}$$

where γ_e and γ_n are the gyromagnetic ratios for electrons and nuclei, respectively, $\mathbf{B}_0$ is the static magnetic field vector, $\mathbf{g}_i$ is the g-tensor of the ith electon, $\boldsymbol{\delta}_k$ is the tensor of chemical shift anisotropy for the kth nucleus.

When we discuss situations where the static magnetic field strength is around 6.7 Tesla, the Zeeman interaction is the dominant interaction of the system.

Dipolar interactions When we talk about dipolar coupling terms, we include both the dipolar couplings among electron spin pairs as well as the nuclei spin pairs:

$$\hat{\mathbf{H}}_{D,tot} = \hat{\mathbf{H}}_{D,e} + \hat{\mathbf{H}}_{D,n} \tag{1.6}$$

$$= \sum_{i \neq j} \hat{\mathbf{E}}_i \cdot \mathbf{D}_{i,j}^e \cdot \hat{\mathbf{E}}_j + \sum_{k \neq l} \hat{\mathbf{N}}_k \cdot \mathbf{D}_{k,l}^n \cdot \hat{\mathbf{N}}_l \tag{1.7}$$

$$= \sum_{i \neq j} \frac{\mu_0 \gamma_e^2 \hbar}{4\pi r_{i,j}^3} \left[\hat{\mathbf{E}}_i \cdot \hat{\mathbf{E}}_j - \frac{3}{r^2} (\hat{\mathbf{E}}_i \cdot \mathbf{r}_{i,j})(\hat{\mathbf{E}}_j \cdot \mathbf{r}_{i,j}) \right]$$
$$+ \sum_{k \neq l} \frac{\mu_0 \gamma_n^2 \hbar}{4\pi r_{k,l}^3} \left[\hat{\mathbf{N}}_k \cdot \hat{\mathbf{N}}_l - \frac{3}{r^2} (\hat{\mathbf{N}}_k \cdot \mathbf{r}_{k,l})(\hat{\mathbf{N}}_l \cdot \mathbf{r}_{k,l}) \right] \tag{1.8}$$

where $\mathbf{D}_{i,j}^e$ is the dipolar coupling tensor between the ith and the jth electronic spin, $\mathbf{D}_{k,l}^n$ is the dipolar coupling tensor between the kth and the lth nuclear spin. μ_0 is the magnetic permeability constant, $\hbar$ is the Plank constant, $r_{i,j}$ is the distance between the ith and the jth electronic spin, and $r_{k,l}$ is the distance between the kth and the lth nuclear spin, $\mathbf{r}_{i,j}$ and $\mathbf{r}_{k,l}$ are the spatial vectors that connect the positions of pairs of free electron and of pairs of nuclei, respectively.

In our system, the two dipolar interactions are both of crucial importance for DNP process: The electron-electron dipolar coupling helps spreading the partial saturation feature across the absorptive ESR line shape through the spectral diffusion mechanism. The nucleus-nucleus dipolar coupling helps propagating the hyperpolarisation from

the nuclei in the vicinity of electron spins to the whole bulk through spatial spin diffusion.

Hyperfine interaction   The hyperfine interaction comprises two parts, the isotropic part due to the Fermi contact interaction between an unpaired electron and the nuclei to which the electron is directly attached, and the anisotropic part due to the dipolar interaction between the electron and nuclei:

$$\hat{\mathbf{H}}_{HF,tot} = \hat{\mathbf{H}}_{HF,iso} + \hat{\mathbf{H}}_{HF,aniso} \tag{1.9}$$

$$= \sum_{i,k} a_{i,k} \cdot \hat{\mathbf{E}}_i \cdot \hat{\mathbf{N}}_k + \sum_{i,l} \hat{\mathbf{E}}_k \cdot \mathbf{A}^d_{i,l} \cdot \hat{\mathbf{N}}_l \tag{1.10}$$

$$= -\sum_{i,k} \frac{2}{3} \mu_0 \gamma_e \gamma_n h |\Psi(0)|^2 \hat{\mathbf{E}}_i \hat{\mathbf{N}}_k$$
$$- \sum_{i,l} \frac{\mu_0 \gamma_e \gamma_n h}{4\pi r^3_{i,l}} \left[\hat{\mathbf{E}}_i \cdot \hat{\mathbf{N}}_l - \frac{3}{r^2} (\hat{\mathbf{E}}_i \cdot \mathbf{r})(\hat{\mathbf{N}}_l \cdot \mathbf{r}) \right] \tag{1.11}$$

where the $a_{i,k}$ represents the scalar for the Fermi contact interaction between the ith electron and the kth nucleus that is directly bound to the electron i, and the tensor $\mathbf{A}^d_{i,l}$ depicts the dipolar part of the hyperfine coupling of a spin pair of one electron i and one nucleus l.

The isotropic part of hyperfine coupling plays an important role in modifying the absorptive ESR line shape of radical. The dipolar part of hyperfine coupling links the electrons and all the nuclei in neighbourhood, which is the major factor for the transfer of hyperpolarisation from electrons to nuclei.

Rearrangement of dipolar terms   If we rearrange the dipolar terms between two spins $\hat{\mathbf{I}}$ and $\hat{\mathbf{S}}$, which can be either an electron or a nucleus, with raising and lowering operators ($\hat{\mathbf{I}}_+$, $\hat{\mathbf{I}}_-$, $\hat{\mathbf{S}}_+$, and $\hat{\mathbf{S}}_-$) and in spherical coordinates, we would have:

$$\hat{\mathbf{H}}_D = -\frac{\mu_0 \gamma_I \gamma_S h}{4\pi r^3} (\hat{\mathbf{A}} + \hat{\mathbf{B}} + \hat{\mathbf{C}} + \hat{\mathbf{D}} + \hat{\mathbf{E}} + \hat{\mathbf{F}}) \tag{1.12}$$

with

$$
\begin{cases}
\hat{\mathbf{A}} = (1 - 3\cos^2\theta) \cdot \hat{\mathbf{I}}_z\hat{\mathbf{S}}_z \\
\hat{\mathbf{B}} = -\frac{1}{4}(1 - 3\cos^2\theta) \cdot \left(\hat{\mathbf{I}}_+\hat{\mathbf{S}}_- + \hat{\mathbf{I}}_-\hat{\mathbf{S}}_+\right) \\
\hat{\mathbf{C}} = -\frac{3}{2}\sin\theta\cos\theta\, e^{-i\phi} \cdot \left(\hat{\mathbf{I}}_+\hat{\mathbf{S}}_z + \hat{\mathbf{I}}_z\hat{\mathbf{S}}_+\right) \\
\hat{\mathbf{D}} = -\frac{3}{2}\sin\theta\cos\theta\, e^{i\phi} \cdot \left(\hat{\mathbf{I}}_z\hat{\mathbf{S}}_- + \hat{\mathbf{I}}_-\hat{\mathbf{S}}_z\right) \\
\hat{\mathbf{E}} = -\frac{3}{4}\sin^2\theta\, e^{-2i\phi} \cdot \hat{\mathbf{I}}_+\hat{\mathbf{S}}_+ \\
\hat{\mathbf{F}} = -\frac{3}{4}\sin^2\theta\, e^{2i\phi} \cdot \hat{\mathbf{I}}_-\hat{\mathbf{S}}_-
\end{cases}
\tag{1.13}
$$

where θ is the polar angle of the spherical coordinate system, and ϕ is the azimuthal angle.

We know that, after diagonalisation, the term $\hat{\mathbf{A}} + \hat{\mathbf{B}}$ commutes with the Zeeman Hamiltonian of the system, and we call it the secular part of dipolar Hamiltonian $\hat{\mathbf{H}}'_D$. The intensity of $\hat{\mathbf{H}}'_D$ indicates the intensity of the *local dipolar field* among spins. The sum of the other terms is called the non-secular part $\hat{\mathbf{H}}''_D$.

Other interactions   In the system we still have a lot of other interactions, for instance the electron zero-field splitting, the Heisenberg exchange interaction, the nuclear scalar couplings and the nuclear quadrupolar interaction. Notwithstanding, on account of that, in the scope of this thesis, we only use monoradicals like TEMPO and its derivatives ($E = 1/2$) for doping the DNP sample and the concentration of radicals in our typical DNP sample is on the order of 10 to 100 mmol/L (equivalent to 0.1% to 1% in molar percentage), the zero-field splitting does not exist and the exchange interactions can be well neglected. Besides, the nuclear scalar coupling is way smaller than all the other interactions. As a result, we only keep the nuclear quadrupolar interaction in our consideration:

$$
\begin{aligned}
\hat{\mathbf{H}}_{other} &= \hat{\mathbf{H}}_Q \\
&= \sum_k \hat{\mathbf{N}}_k \cdot \mathbf{Q}_k \cdot \hat{\mathbf{N}}_k \tag{1.14} \\
&= -\sum_k \frac{eQ}{2N_k(2N_k - 1)h} \hat{\mathbf{N}}_k \cdot \mathbf{V}_k \cdot \hat{\mathbf{N}}_k \tag{1.15}
\end{aligned}
$$

where N_k is the spin quantum number of the kth nuclear spin, e is the elementary charge, Q is the nuclear quadrupole moment, and $\mathbf{V}_k$ is the electric field gradient tensor.

When the sample is free of quadrupolar nuclear spins, this term does not exist in the total Hamiltonian. When the presence of quadrupolar nuclear spins are abundant, they might serve as one of the sources of nuclear relaxation of hyperpolarisation even in a liquid helium bath.

Radiofrequency pulses and microwave irradiation This term is also composed of two parts: the radiofrequency part mainly works on nuclear spins and the microwave part operates on the electrons.

$$
\begin{aligned}
\hat{\mathbf{H}}_{\mu w} + \hat{\mathbf{H}}_{RF} = & -\sum_i 2\gamma_e B_{1,i}^{\mu w} \hat{E}_{x,i} \cos(\omega_{\mu w} t) \\
& -\sum_k 2\gamma_n B_{1,k}^{RF} \hat{N}_{x,k} \cos(\omega_{RF} t)
\end{aligned}
\tag{1.16}
$$

where $B_{1,i}^{\mu w}$ is the strength of microwave field at the position of the ith electronic spin, $\omega_{\mu w}$ is the frequency of microwave field, $B_{1,k}^{RF}$ is the strength of radiofrequency field at the position of the kth nuclear spin, and ω_{RF} is the frequency of radiofrequency field.

The microwave irradiation mainly serves for the partial saturation of ESR line shape. The radiofrequency is used for not only the transfer of hyperpolarisation between different nuclei by cross polarisation but also for signal detection.

In the end, the simplified total stationary Hamiltonian writes:

$$
\hat{\mathbf{H}}_{Tot} = \hat{\mathbf{H}}_{Z,e} + \hat{\mathbf{H}}_{Z,n} + \hat{\mathbf{H}}_{D,e} + \hat{\mathbf{H}}_{D,n} + \hat{\mathbf{H}}_{HF,iso} + \hat{\mathbf{H}}_{HF,aniso} + \hat{\mathbf{H}}_Q + \hat{\mathbf{H}}_{\mu w} + \hat{\mathbf{H}}_{RF} \tag{1.17}
$$

Relaxation Supermatrix

Like we use the Hamiltonian of the system to approximate the coherent evolution of the system, we rely on the relaxation superoperator to estimate the incoherent part.

Under the assumption that the semi-classical theory of relaxation is valid, the system of spins is coupled to the environment by some time-dependent stochastic fluctuations that have a vanishing average over time, which was first introduced by Bloch and Wangsness and later extended by Redfield as the famous *Bloch-Wangsness-Redfield theory*.

$$\hat{\hat{\mathbf{R}}}\big(\hat{\rho}(t) - \hat{\rho}_{eq}\big) = \int_0^\infty d\tau \left[\overline{\hat{\mathbf{H}}_1(t), \left[\exp(-i\hat{\mathbf{H}}_0\tau)\hat{\mathbf{H}}_1(\tau - t)\exp(i\hat{\mathbf{H}}_0\tau), \big(\hat{\rho}(t) - \hat{\rho}_{eq}\big)\right]} \right]$$

(1.18)

where $\hat{\mathbf{H}}_1(t)$ is a time-dependent stochastic Hamiltonian that describes the random motions with zero time-average, $\hat{\mathbf{H}}_0(\tau)$ is the static coherent part of the spin system.

1.2.2 DNP Part

In principle, there are four major mechanisms that can explain the transfer of polarisation from electronic spins to nuclear spins:

- Overhauser Effect

- Solid Effect

- Cross Effect

- Thermal Mixing

In the following section, we limit ourselves to a concise introduction of the main DNP process in our d-DNP experiments, the thermal mixing.

Spin Temperature   When all off-diagonal terms of the density matrix of the spin system vanish, the system is a canonical ensemble, where the distribution of the populations of the eigenstates of the spin system conform to the Boltzmann distribution. As an analogue for the concept of temperature in a canonical internal equilibrium, we can use a time-dependent spin temperature to describe the time-dependent distribution of the populations of the spin system [39, 40]. In addition, with the concept of spin temperature, we can also define the *internal energy* as well as the temperature-dependent *heat capacity* of the spin system.

For a spin system with total Hamiltonian $\hat{\mathbf{H}}_0$, we can express the corresponding density matrix of the system as a function of the inverse spin temperature T_S:

$$\hat{\mathbf{H}}_0 = \sum_i \hat{\mathbf{H}}_i \tag{1.19}$$

$$\implies \hat{\rho} = \frac{\exp\left[-\frac{\hbar\hat{\mathbf{H}}_0}{kT_S}\right]}{\mathrm{Tr}\left[\exp\left[-\frac{\hbar\hat{\mathbf{H}}_0}{kT_S}\right]\right]} \tag{1.20}$$

$$= \frac{\exp\left[-\sum_i \frac{\hbar\hat{\mathbf{H}}_i}{kT_{S,i}}\right]}{\mathrm{Tr}\left[\exp\left[-\sum_i \frac{\hbar\hat{\mathbf{H}}_i}{kT_{S,i}}\right]\right]} \tag{1.21}$$

where $\hat{\mathbf{H}}_i$ indicates an independent constant of motion of the system, $kT_{S,i}$ is the spin temperature related to the ith reservoir, $\hbar$ is the Plank constant, and k is the Boltzmann constant.

If we use the inverse spin temperature T_{IS}, the expression has a more concise form:

$$\begin{cases} T_{IS} & \overset{def}{=\!=\!=} \frac{\hbar}{kT_S} \\[2ex] \hat{\rho} & = \frac{\exp\left[-\sum_i T_{IS,i}\hat{\mathbf{H}}_i\right]}{\mathrm{Tr}\left[\exp\left[-\sum_i T_{IS,i}\hat{\mathbf{H}}_i\right]\right]} \end{cases} \tag{1.22}$$

A Taylor expansion can help us transform the matrix exponential into a series:

$$\hat{\rho} = A \times \exp\left[-\sum_i T_{IS,i}\hat{\mathbf{H}}_i\right] \tag{1.23}$$

$$= A \times \left[\hat{\mathbf{1}} + \frac{(-1)^k}{k!}\left[-\sum_i T_{IS,i}\hat{\mathbf{H}}_i\right]^k\right] \tag{1.24}$$

where A is a scalar factor for normalisation.

In the high temperature approximation, where $||T_{IS,i}\hat{\mathbf{H}}_i|| \ll 1$, we can keep only the first order terms and neglect the contributions of all higher order terms, which gives us the conventional results:

$$\hat{\rho} = A \times \left[\hat{\mathbf{1}} - \sum_i T_{IS,i}\hat{\mathbf{H}}_i\right] \tag{1.25}$$

where $\hat{\mathbf{1}}$ is the operator of unity.

From eq. (1.25), we can see that each spin temperature corresponds to one of the constants of the motion inside the whole spin system. In thermal equilibrium, all these spin temperatures equal to the macroscopic temperature of the lattice. When the system is out of equilibrium, the spin temperature is no longer obliged to be the same as the lattice temperature, and then each spin temperature can evolve in an independent way.

Thermal Mixing   Similar to the heat transfer between two objects with different initial temperatures, the transfer of energy can also take place among the electron Zeeman system, the electron dipolar system, and the nuclear Zeeman system. This flow of energy eventually results in a steady state where the spin temperatures of the three different reservoirs are identical, which is called *Thermal Mixing*.

The occurrence of thermal mixing requires two conditions:

- The ESR line width is broader than the NMR frequency;

- The dipolar coupling among electron spins is strong enough that the electronic spin diffusion is much faster than electronic longitudinal relaxation, which permits the establishment of a single spin temperature of the electronic dipolar system.

Once the conditions of thermal mixing are fulfilled, in the presence of microwave irradiation, the DNP process can take place, as shown in fig. 1.2:
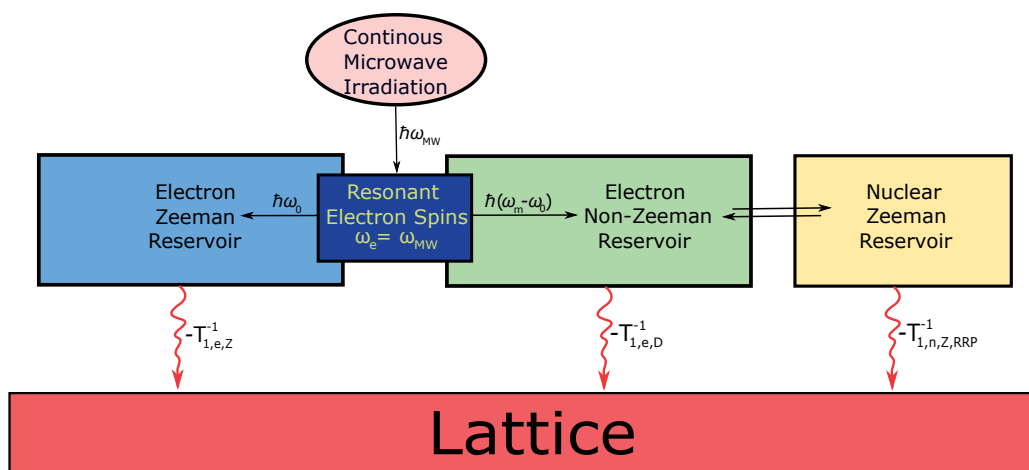

Figure 1.2 – An illustration of the thermal mixing process in a homogeneous spin glass for DNP

In the first place, the microwave irradiation saturates the electron spin packet on resonance with respect to the frequency of the irradiation, which spontaneously changes the distribution of populations in the electron Zeeman manifold. At the same time, due to the dipolar interactions among the electrons, magnetic energy exchanges among the spin packets with similar energies, which leads to a partial saturation of the whole line-shape. This partial saturation then results in the evolution of spin temperature in the electron dipolar reservoir. As mentioned above, the ESR line width is broader than the NMR frequency, we might say that the whole nuclear reservoir is immersed inside the electron dipolar reservoir. The nuclear polarisation evolves consequently towards the same steady-state with respect to the non-Zeeman electron order, and eventually the electron Zeeman manifold.

1.3   Practical Aspects of D-DNP Experiments

In this section, we present a short picture of how d-DNP experiments are conducted. Typically, they consists of four stages:

1.3.1   Sample preparation

Before starting d-DNP experiments, we have to first find a suitable sample that is in its optimal state for the transfer of polarisation between electron spins and nuclei. As we see, most MOI do not contain paramagnetic species as a source of hyperpolarisation. It is natural for us then to dope pure MOIs or solutions of MOIs with polarising agents. The key of a successful sample lies in the optimisation of hyperfine couplings between doped unpaired electrons and the nuclei. Let's begin with an idealised model with a single electron spin.

The fig. 1.3 illustrates how the nuclei in close vicinity to an electronic spin (within *ca.* 1 nm) experience a hyperfine splitting that is no less than 1 MHz, and this dipolar coupling drops to about 10 kHz when the radius of neighbouring pair extends to around 2 nm. On the other hand, from eq. (1.6), we see that the average intensity of local dipolar fields of protons in a fully protonated solid is on the order of 10-100 kHz.

In this system, the DNP can happen in two ways. One way, which is direct, happens as the joint consequence of the anisotropic part of the hyperfine coupling and the constant microwave irradiation. The other way, which is less straight-forward, occurs when extra nuclei act as intermediates: the intermediate nuclei first gets polarised through the direct effect, then by the exchange of nuclear magnetic energy (*i.e.* by spin diffusion) among like spins, the target nucleus acquires a polarised state.

From those distinct strengths of the dipolar fields shown in fig. 1.3 we can infer that, for nuclear spin packets that are in close vicinity of the polarising agent, the large dipolar part of the hyperfine interaction permits its rapid polarisation. Meanwhile,
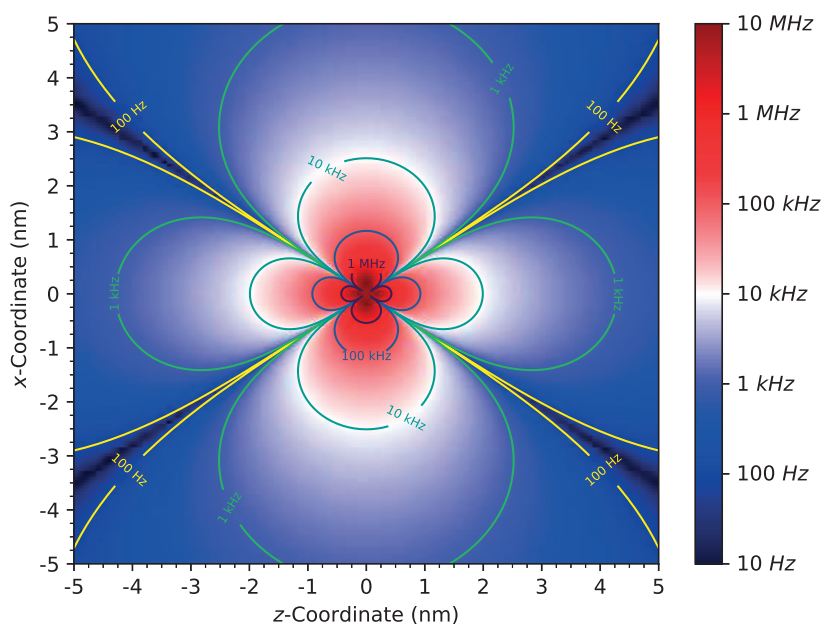
Figure 1.3 – The intensity of the dipolar field that results from the anisotropic hyperfine interaction around an electronic spin

the large hyperfine interaction also forbids these nuclei from participating into the indirect polarising process by playing the role of polarised intermediates. This is because the frequency of the NMR absorption of such nuclei is largely distinct from the frequency of the nuclei in the bulk. According to the Fermi's Golden Rule, the transition probability of coherent energy transfer becomes almost negligible.

When it comes to the nuclear spins that resides at a medium distance from the polarising agents, the dipolar field of the hyperfine couplings and the dipolar field of the network of likespins are almost of the same order of magnitude. The comparable intensity of two dipolar fields suggests that these kinds of nuclear spins are still in thermal contact with the bulk nuclei. Therefore, they are able to receive the polarisation from electron spins at a reasonable rate (10-100 kHz) without loosing the transitional role that links the flow of magnetic energy from paramagnetic centres throughout the sample.

Meanwhile, when a nucleus has a position in the region where the dipolar field from HFI is smaller with respect to the nuclear local dipolar field, its probability of being directly polarised would be significantly smaller than nuclei than for nuclei in the two above-mentioned categories. It is then a reasonable conjecture that the nuclear spins of this category are mainly polarised through the indirect effect.

In a real sample, where the spins far outnumbers the one-spin model specified

above, the story complicates itself in an exponential manner. The very first one comes from the heterogeneity of the sample, which is introduced by radical doping. As a result of thermodynamics, when we launch the radical-doped MOI or solution of MOI into the polariser, this multi-component mixture freezes to become a solid. More specifically, under most circumstances, the uniform liquid sample freezes into a heterogeneous poly-crystalline mixture, where each chemical compound belongs to the clusters of its own phase. Such a phase separation has two negative influences on the DNP performance of the sample. First, since the dipolar interaction between polarising agent and nuclei only works at short distances, under the condition of phase separation the grains of free radicals can only affects a very limited volume around themselves, leaving the largest part subject to the indirect polarisation transfer. On the other hand, within the clusters of radicals, the distances between free electrons are on the sub-nanometric scale. The intensity of electron-electron dipolar fields is on the order of tens and even hundreds of megahertz. The anisotropic part of hyperfine splittings is negligible compared to such huge entanglements between electron spins, which directly leads to a poor performance in the DNP process. Aiming at preventing a phase separation during sample freezing from occurring, people in the community places high interests on maintaining the random distribution of all species of molecules by freezing the sample into a glassy form.

As a result, when we are searching for a suitable d-DNP sample, generally we have two approaches. Either we flash-freeze the mixture of radicals and MOIs directly to obtain the spin glass, before the crystallisation and phase-separation take places in the sample. This direct vitrification is often adopted when we wish to polarise the molecules that has distinct transition between glassy phases and crystalline phases, e.g. pyruvate acid [24], *ortho*-tertphenyl [41], amorphous powders of spin-labelled amorphous proteins [42], or radical-functionalised porous material[43, 44]. Or we dissolve the MOI in a mixed solvent that consists of a good solvent that favours of the MOI solubility, as well as a glassy agent to prevent the occurrence of crystallisation and phase-separation during the freezing process. Seeing that most of the chemicals do not possess a kinetically stable vitreous phase, we are thus obliged to prepare the d-DNP sample of these MOIs with the help of vitrifying media[45, 46, 47].

Recently, the Cesàro's group also proposed a new mechanical method: crystalline substances and polarising agents are mixed for co-grinding[48]. The crystalline structure of the MOI is reported to be crushed into a vitreous phase for DNP experiments. Although this method could be considered as an important progress in the preparation of kinetically stable d-DNP samples in uniformly vitrified phases, by virtue of the removal of the glassy agent, this method, admittedly, is confined in the Dogma that demands the glassy state of DNP samples. Besides, such approach is unable to solve the inherent drawback of homogeneous spin glasses: the fast nuclear relaxation induced by paramagnetic impurities, which severely deteriorate the final polarisation arriving at the detection devices after sample dissolution.

1.3.2 Build-up of hyperpolarisation

Direct build-up

Formulated with the appropriate composition, the DNP sample is sent into the polariser for the DNP process.

First, the sample is fully cooled down in a liquid helium bath at 1.2K in a static magnetic field. In our experimental set-up, the unpaired electrons can reach a polarisation of 99.5% in a static magnetic field of 6.7 T. With a continuous microwave irradiation of 87.5 mW ranging from 187 GHz to 189 GHz*, the high electron polarisation is transferred to the nuclei.
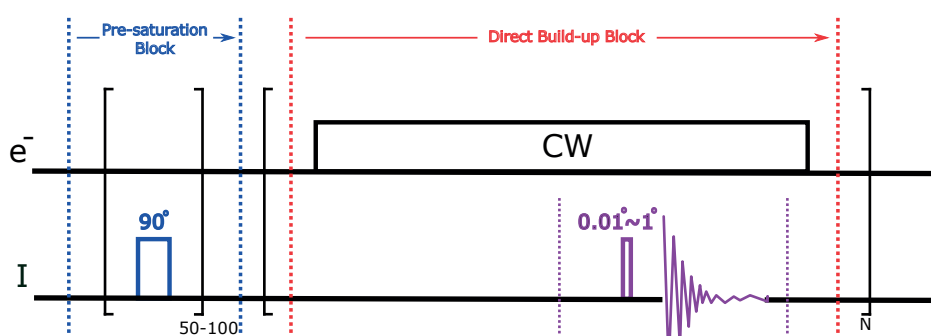

Figure 1.4 – The pulse sequence used for direct build-up of polarisation.

We can find in fig. 1.4 that a direct DNP build-up involves two basic blocks: the presaturation block and the direct build-up block. In the presaturation block, we use a series of 90 deg RF pulses to saturate all the polarsiation that has been previously accumulated in the system. In the direct build-up block, the nuclear spins constantly receive energy from other nuclear spins. At the end of each block, we perform a pulse-acquisition with very small flip-angles, which does not destroy the hyperpolarisation in the nuclear spin reservoir while it gives us enough information on the evolution of system. A typical example of a direct build-up curve can be found in fig. 1.5.

CP build-up

When we are interested in the hyperpolarisation of low-γ nuclei like ^{13}C or ^{15}N *etc.*, the conventional way is to directly polarise these nuclei with trityl radicals. A brilliant example is reported by Golman *et al.* [49]. In this paper, they have doped 1-^{13}C-pyruvic acid with Tris(8-carboxy-2,2,6,6,-tetra(methoxyethyl)benzo[1,2-d:4,5d']*bis*(1,3)dithiole-4-yl)methyl sodium salt at the concentration of 15 mmol·L−1, and subsequently injected this hyperpolairsed molecule into the hind leg of a pig so as to visualise real-time metabolic processes.

---

*The acual frequency in a specific experiment depends heavily on the nature of radical as well as on the mode of the hyperpolarisation (positive or negative) that we expect.
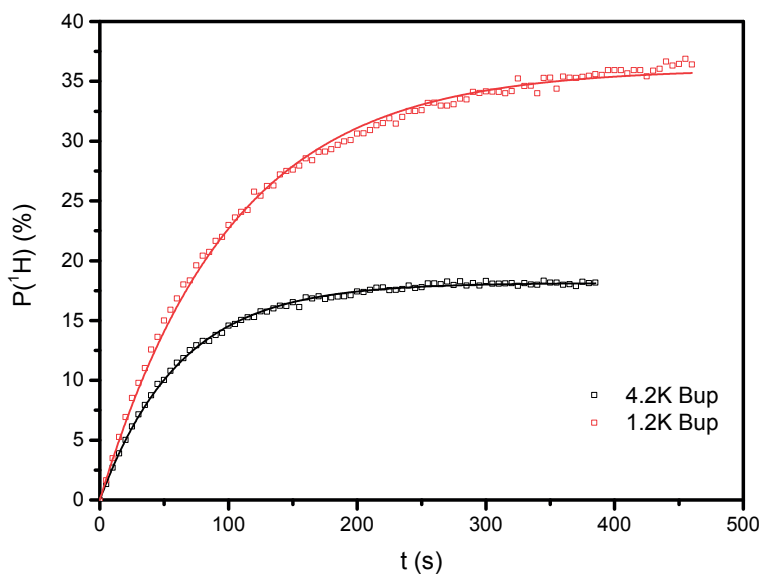
Figure 1.5 – The ^1H build-up of DNP process in a solution of 1-^{13}C Sodium Acetate in mixed solvent of 10% H_2O, 40% D_2O, 50% d^8 Glycerol at concentration of 3 mol·L^{-1}. The black squares indicate the acquisition points of experimental data during the build-up at 4.2K, and the red squares stand for the experimental data of the build-up at 1.2K. The solid lines are monoexponential fits to the experimental data.

Such a DNP process in a radical-doped mixture permits us to enter a promising new area of research. Notwithstanding, because of the low susceptibility of low-γ nuclei, compared with the build-up process of ^1H, the direct DNP approach suffers from drawbacks like long polarising times and low final polarisation. Various attempts have been proposed to ameliorate the performance, such as using carefully designed biradicals [50] or co-doping with paramagnetic metal ions. When these methods are combined, it is possible to achieve a carbon polarisation of 50% at 3.35 T and 70% at 4.64 T, but the build-up rate is not necessarily shortened.

With the help of multi-channel RF coils, we can then perform the cross-polarisation (CP) under the Hartmann-Hahn condition to polarise low-γ nuclei from hyperpolarised protons in the sample [51, 52, 53, 54, 55, 56]. The main advantage of this CP scheme is that the build-up of low-γ nuclei now depends on the build-up rate of the protons, which is significantly faster.

As illustrated in fig. 1.6, the polarisation first accumulates in the proton Zeeman reservoir, and then CP equalise the polarisation between protons and low-γ nuclei. In view of protecting the hyperpolarisation in both channels from the fast transverse relaxation after CP, two adiabatic half passage pulses are applied to reoriente the magnetisation vector back so as to be parallel with respect to the static field. Then we repeat the two blocks of proton build-up and of cross-polarisation, until the
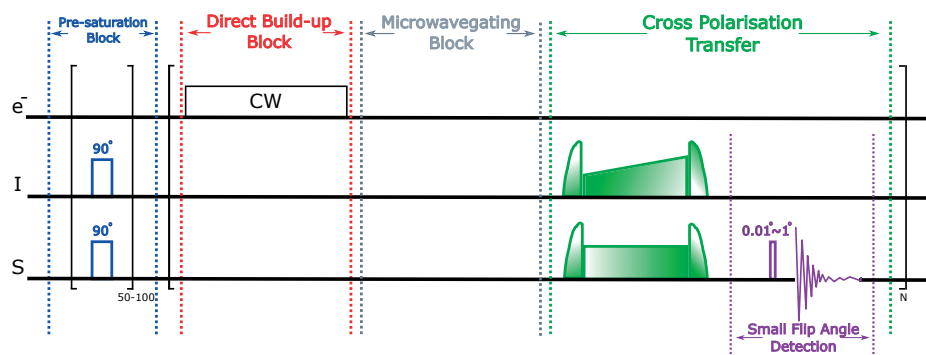
Figure 1.6 – The pulse sequence used in CP build-up of polarisation.

polarisation of low-γ nuclei reaches its maximum. At the end of each of the two blocks, we also place a pulse-acquisition block with small flip-angle on the low-γ channel, so as to follow the build-up process, which is demonstrated in fig. 1.7
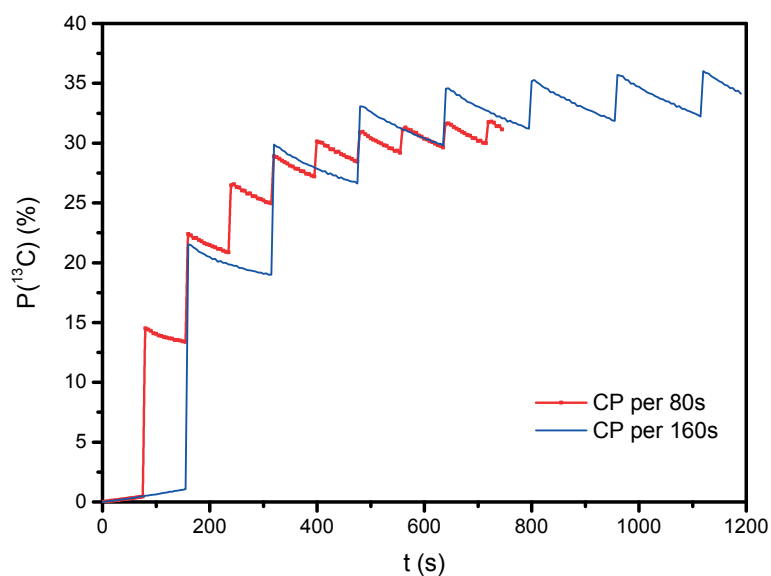
Figure 1.7 – The ^{13}C CP build-up of DNP process in a solution of 1-^{13}C Sodium Acetate in mixed solvent of 10% H_2O, 40% D_2O, 50% d^8 Glycerol at concentration of 3 $mol \cdot L^{-1}$. The red line indicates the evolution of ^{13}C polarisation during CP build-up at $1.2K$, where the interval of ^1H build-up between two CP blocks lasts 80 seconds. The blue line represents the evolution of ^{13}C polarisation of the same sample with a interval of 160 seconds between two CP blocks.

1.3.3 Sample dissolution and transfer

When the rate of nuclear relaxation approaches the rate of polarisation transfer from radicals to nuclei, the build-up process reaches a steady state. No more net nuclear

polarisation can be added to the system, even if the DNP process keeps going on. Once this DNP limit is attained, we can thus stop the polarising process. In order to make use of the hyperpolarised sample, overheated water is then shed onto the frozen spin glass for its dissolution. Then the solution is pushed out of the polariser with overpressured inert gas and transferred to the apparatus for signal detection. It is worthy to note that, because of the fast nuclear relaxation in low field, the pipeline for the transfer of the hyperpolarised solution is protected by a magnetic tunnel[57].

1.3.4 Signal detection

After the injection of the hyperpolarised fluid into the container awaiting the apparatus for sample detection, we can start experiments for NMR/MRI. The scope of research includes but is not limited to the analysis of sample composition [58, 59], enzymatic reactions [60, 61], protein-ligand interaction [62, 63], oncology [64, 65] and *in-vivo* imaging for physiological studies [27, 66, 67]

1.4 Transportable Relay DNP and New Sample Formulation

Though the d-DNP is a powerful tool, the demanding requirements of the hyperpolarising system on both hardware and staff severely hinders the general application of this technique. A natural question then comes to our mind: Can we physically decouple the polarising system from the detecting system?

In the initial stage of the development of the d-DNP technique, people have attempted to take the polarised sample out of the polariser. Their endeavour, however, did not yield any success. The major reason of lies in the features of nuclear relaxation of hyperpolarised samples.

As we can imagine, under typical conditions of DNP build-up, where the sample is placed in magnetic field of 6.7 T and immersed in a liquid helium bath of 1.2 K, the relaxation of nuclear magnetic energy is very slow: The $T_{1,^1H}$ is on the order of $10^2 - 10^3$ s, the $T_{1,^{13}C}$ is on the order of $10^3 - 10^4$ s. Such long nuclear relaxation times are mainly due to two reasons. First, the low temperature of the environment forbids almost all microscopic motions in the sample, which results in a very limited number of phonon modes and thus an inefficient coupling between nuclear magneton and phonon. In addition, at such temperatures, the electrons spins are almost fully polarised due to their inherent high magnetic moments with an average T_{1,e^-} on the order of $10^{-1} - 10^1$ s. Under such conditions, the fluctuating dipolar fields, as a result of anisotropic hyperfine couplings, are largely suppressed, and so are the contributions of paramagnetic relaxation.

If we now lift the hyperpolarised sample from the ideal condition of low temperature and high field to room temperature in the Earth's field, the scenario of relaxation changes drastically. The first issue we have to deal with is the relaxation rate at high temperature. As the temperature of hyperpolarised spin glasses increases, the molecular motions, such as stretching, scissoring, rocking, wagging, or twisting, gradually came back to life from the initial frozen state. Also, the absolute value of the electron polarisation shrinks as the temperature goes up, which favours the fluctuations of local dipolar fields in the radical-doped spin glasses. On the other hand, the hyperpolarisation experiences a different spin dynamics in low field (*ca.* the Earth's field) than in high field. Typically, when the magnitude of the external magnetic field during the transport of the hyperpolarised sample is of the same level as the local dipolar field in the spin glass, peculiar phenomena may happen. For instance, the nuclear thermal mixing equalises the spin temperature of all nuclear species at a speed that is on the same order as the transverse relaxation rate R_2. Therefore, the key of transportable hyperpolarisation lies in minimising the relaxation rate of nuclear magnetisation.

As previously stated, the nuclear relaxation caused by molecular motions can be reduced by storing the hyperpolarised sample in a liquid helium bath, and the contributions of nuclear thermal mixing can be removed by keeping the sample in a permanent magnet during storage. All these strategies, however, cannot significantly reduce the fluctuations of local dipolar fields from doped polarising agents. The paramagnetic relaxation becomes the main leak of nuclear polarisation.

The solution to paramagnetic relaxation can be found by exploiting the short-range nature of dipolar interaction. A quick revisit of fig. 1.3 tells us that, the paramagnetic centres can only exert their influence on nuclear spins within an envelope of limited range. The idea of constructing an artificial segregation in space between the radicals and the MOIs came to our minds. In principle, the molecules of the polarising agents are expelled from the clusters of the MOIs, so that the MOI can only receive hyperpolarisation through spatial spin diffusion. At the same time, the aggregates of MOIs are immune to the paramagnetic relaxation during storage/transportation, because the fluctuations of local dipolar fields due to distant free electrons is now negligible.

In practice, we use an artificial phase-separation to realise the above-stated principle: the glassy solution of radical forms the *Radical Rich Phase* (RRP), while the MOI alone stays in a distinct *Radical Free Phase* (RFP). The two individual phases are only connected by thermal contact at their interface. Thanks to the reduction of thermal exposure between electronic spins and the MOIs in the RFP, the paramagnetic relaxation is eliminated, and thus the lifetime of hyperpolarisation of MOI is significantly extended. With the prolonged lifetime of hyperpolarisation, transportation of hyperpolarised MOI now becomes possible.
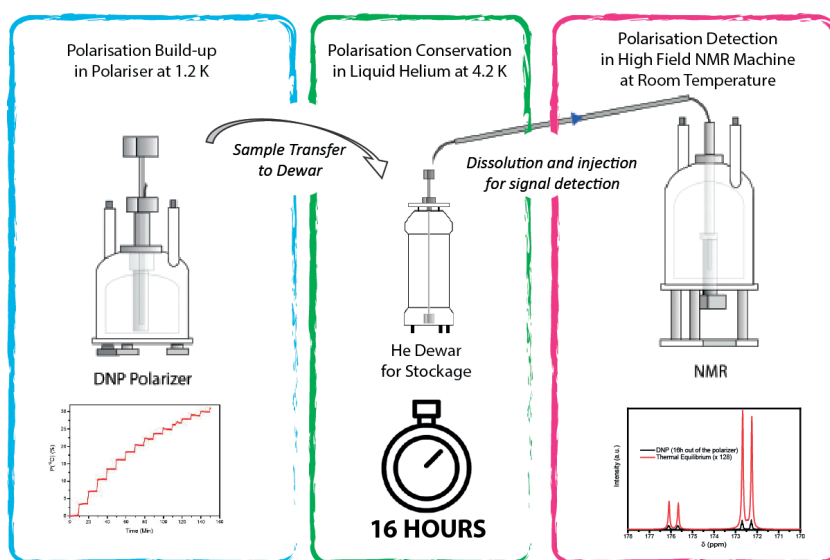
Figure 1.8 – An illustration of transportable d-DNP. The blue box indicates the stage of polarisation build-up. The build-up curve(red line) here shows the process of diffusion-relayed DNP. The green box shows a 16-hour-long storage of the hyperpolarised sample. In the red box, the result of signal detection is shown in the spectrum at the bottom. The signal of hyperpolarised amino acid (red line) is around 648 times stronger than the thermal signal at room temperature (black line, 128 times magnified)

2 Modelling Diffusion-Relayed DNP in Biphasic Samples

In a biphasic sample, the build-up of the nuclear polarisation comprises three steps: First, the direct contact between an unpaired electron and nuclei in its vicinity, so that hyperpolarisation builds up in the radical-rich phase (RRP). Then the polarisation flows into the radical free phase (RFP) due to the spatial inhomogeneity of polarisation. Since the spin diffusion is the bottleneck step of the DNP process, the build-up rate of hyperpolarisation and the final polarisation at steady state could both be unsatisfactory. In order to equip ourselves with at least qualitative, preferably with quantitative insight into the physical parameters of biphasic samples, we shall discuss in this chapter the development of a numerical approach that allows the visualisation of the spatial propagation of nuclear polarisation during the diffusion-delayed DNP process in biphasic samples.

Since the 1950s, various schemes based on pure quantum mechanics have been proposed for evaluating the behaviour of spin diffusion [68, 69, 70, 71, 72, 73]. All of these analytical methods demand significant efforts for their mathematical treatment. In addition, we can only obtain straightforward expressions when the spin lattice remains simple and the geometry not too complicated. Consequently no detailed attempts of this sort will be presented in this chapter.

Like all the coherent processes, the diffusion of spins can be simulated by first-principle approaches on a quantum-mechanical basis [74, 75, 76, 77, 78, 79, 80, 81]. Needless to say, we can expect a quasi-exact solutions from such a formalism, except some inevitable errors due to the nature of numerical analysis, like truncation errors. Unfortunately, this approach can hardly be applied in our case: the diameter of particles of molecules of interest (MOI) that we use is nano-metric, even micro-metric. This meansthat we have at least 10^5 molecules inside a particle. A system consisting of such an enormous number of spins remains a challenge for modern computational technology, letting aside that we have not yet included the RRP as an additional phase.

Inspired by the hydrodynamic approach proposed by D. Greenbaum *et al.* [82], we

present an attempt based on the classic theory of heat conduction. The finite element method (FEM) is applied to visualise the picture, where the diffusion of magnetic spin is associated with the evolution and propagation of magnetic energy in spin reservoirs. With this method, we hope that a rational design of the biphasic samples for d-DNP experiments will eventually be possible.

2.1 The Basic Thermodynamic Concepts

In the frame of spin temperature theory, we use eq. (1.25) to approximate the thermo-dynamics of the spin system that conforms to the high-temperature assumption.

As the DNP process proceeds, the nuclear spins are so well polarised that the inverse spin temperatures of the constants of motions are becoming significant, and we can no longer neglect the higher terms in the series expansions of exponential functions of the Hamiltonian. Therefore, we are obliged to find a suitable measure of thermodynamics parameters in the system, so as to replace the (inverse) spin temperature. Detailed discussions can be found in the book by Wenckebach [83].

2.1.1 Spin temperature theory in measure of polarisation

Consider a simple system of spin $I = 1/2$ which merely has a Zeeman splitting. If we express the density operator in the high temperature approximation, we then have:

$$\hat{\rho} = A \times \left[\hat{\mathbf{1}} - T_{IS,z} \hat{\mathbf{H}}_z \right] \tag{2.1}$$

On the other hand, we can also reconstruct the density operator of the same system using the concept of *spin polarisation*, which is a dimensionless quantity defined as the difference of population between two energy levels:

$$P \overset{def}{=\!=\!=} \frac{p_- - p_+}{p_+ + p_-} \tag{2.2}$$

where P is the polarisation of spin I in this system with a range $P \in [-1, 1]$, p_+ is the population of particle on the eigenstate with higher energy, and p_- is the population of particle on the eigenstate with lower energy. All the three variables are functions of the inverse spin temperature T_{IS} and can be time-dependent.

The density operator is then:

$$\begin{cases} P = \tanh\left(\frac{1}{2} T_{IS} \gamma B_0\right) \\ \hat{\rho} = \frac{1}{2} \cdot \begin{pmatrix} 1-P & 0 \\ 0 & 1+P \end{pmatrix} \end{cases} \tag{2.3}$$

Defining $\hat{\mathbf{P}}_z$ as the polarisation operator of the system, we can then rewrite the density operator of this two-level system in a linear form in analogy to the expression of the high temperature approximation.

$$\begin{cases} \hat{\mathbf{P}}_z \overset{def}{=\!=\!=} P \cdot \hat{\mathbf{I}}_z \\ \hat{\rho} = \frac{1}{2}(\hat{\mathbf{I}} - \hat{\mathbf{P}}) \end{cases} \tag{2.4}$$

Though eq. (2.1) and eq. (2.4) have similar forms, it is worthy noting that eq. (2.4) is a general formula that is valid beyond the limits of the high-temperature approximation. The only constraint of eq. (2.4) is that the matrix representation of the density operator of the spin system must not have any off-diagonal terms. Since typical transverse relaxation times (T_2) of the electronic spins are on the order of nanoseconds and those of nuclei are on the order of milliseconds to seconds, the constraints perfectly match with the time-scale of this research (from minutes to hours).

The molar capacity of the magnetic energy in terms of polarisation (C_p) can be defined as the amount of magnetic energy required to polarise a mole of spins from 0 to 100 %:

$$C_p \overset{def}{=\!=\!=} \frac{1}{2} \cdot \hbar \gamma B_0 \cdot N_A \tag{2.5}$$

Where $\frac{1}{2} \cdot \hbar \gamma B_0$ refers to the energy that is emitted or absorbed by a spin in a field B_0 in units of Joule, c is the spin density in mole per liter, and N_A is the Avogadro's constant.

In the following sections, we shall be using the *polarisation* rather than the *(inverse spin temperature* as the measure of thermodynamics of the system.

2.2 Diffusion of magnetic energy in direct Diffusion-Relayed DNP

Our objective in this section is to find a suitable method of describing the time-dependent behaviour of high-γ nuclei, for instance ^1H, during the process of direct Diffusion-Relayed DNP.

2.2.1 Parabolic Partial Differential Equation for Diffusion of Energy

In accordance with the conventional practices for the study of heat conduction, we can restate the quantum mechanical phenomenon of spin diffusion in the form of a spatial redistribution of magnetic energy as a function of time by a parabolic partial differential equation(PDE):

$$
\begin{cases}
d_a(\boldsymbol{r}) \cdot \dfrac{\partial P(\boldsymbol{r}, t)}{\partial t} = \nabla \cdot \big(\kappa(\boldsymbol{r}) \, \nabla P(\boldsymbol{r}, t)\big) & \text{(2.6a)} \\[2mm]
D(\boldsymbol{r}) = \kappa(\boldsymbol{r})/d_a(\boldsymbol{r}) & ,\boldsymbol{r} \in \Omega = \Omega_{RRP} \bigcup \Omega_{RFP} \quad \text{(2.6b)} \\[2mm]
d_a(\boldsymbol{r}) = C_p(\boldsymbol{r}) \cdot c(\boldsymbol{r}) & \text{(2.6c)}
\end{cases}
$$

where Ω is the entire geometric region, which consists of both RRP (Ω_{RRP}) and RFP (Ω_{RFP}), $\boldsymbol{r} = \sum_i x_i \cdot \boldsymbol{e}_i$ refers to the position vector, $\boldsymbol{e}_i$ are basic vectors of space ,d_a, the scalar damping factor, corresponds to the energy that we need to polarise all the nuclei in one cubic metre of sample, which is equal to the product of molar capacity of magnetic energy and the molar concentration of nuclear spin per cubic metre. D, the spin diffusivity, is a scalar number in an isotropic media, while it is a second-rank tensor in anisotropic media. κ, by a comparison with its counterpart in thermal conduction, refers to the spin conductivity: the speed of spatial propagation in a nuclear spin reservoir under a polarisation gradient of 1 m^{-1}. It can be either a scalar or a tensor according to the properties of medium. It is worthy to note that all these physical properties can be different from one phase to the other.

The boundary conditions of the system are listed below:

$$
\begin{cases}
\dfrac{\partial}{\partial \boldsymbol{n}} P(\boldsymbol{r}, t) = 0, \forall \boldsymbol{n} \in \partial\Omega_{Out} & \text{(2.7a)} \\[2mm]
\lim_{\boldsymbol{r} \to \partial\Omega_{In}} P(\boldsymbol{r} \in \Omega_{RFP}, t) = \lim_{\boldsymbol{r} \to \partial\Omega_{In}} P(\boldsymbol{r} \in \Omega_{RRP}, t) & \text{(2.7b)} \\[2mm]
- \lim_{\boldsymbol{r} \to \partial\Omega_{In}} \kappa_{RFP} \cdot \nabla P(\boldsymbol{r} \in \Omega_{RFP}, t) = \lim_{\boldsymbol{r} \to \partial\Omega_{In}} \kappa_{RRP} \cdot \nabla P(\boldsymbol{r} \in \Omega_{RRP}, t) & \text{(2.7c)} \\[2mm]
P(\boldsymbol{r}, t = 0) = 0, \forall \boldsymbol{r} \in \Omega & \text{(2.7d)}
\end{cases}
$$

where $\partial\Omega_{Out}$ is the geometric boundary between the whole sample (Ω) and the environment, while $\partial\Omega_{In}$ is the interface between the Ω_{RRP} and the Ω_{RFP}, and $\boldsymbol{n}$ is a vector normal to the boundary.

eq. (2.7a) is the Neumann condition that ensures the adiabaticity of the whole system. This is the direct result of the absence of coherent transfer of magnetic energy between the macroscopic sample and its environment. eq. (2.7b) and eq. (2.7c) describe the behaviour on the biphasic interface. The former implies that the two distinct phases share the same value of the nuclear polarisation at the interface, which follows the requirement of continuity. The latter follows the conservation of magnetic energy between the two distinct phases. The initial condition of the system is set to be uniformly zero (see eq. (2.7d)), which corresponds to our experimental conditions where all thermal polarisations are being eliminated by pre-saturation at the beginning of the build-up sequence, as shown in fig. 1.4.

2.2.2 Coupling Spin Diffusion with DNP

Revisiting the DNP model

We can see that the pure diffusion equation in eq. (2.6) and eq. (2.7) is only valid in an energy-conserving system. As illustrated in section 2.2.2, the actual case of DNP, however, does not meet these criteria. When the nuclear polarisation builds-up, we have an inward flow of nuclear energy from the non-Zeeman electron reservoir to the nuclear reservoir of RRP.
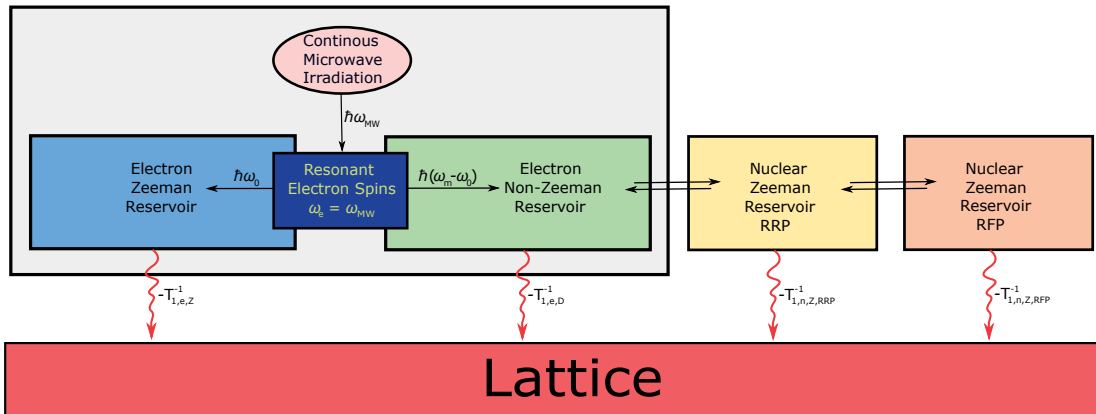
Figure 2.1 – An illustration of spin diffusion relayed DNP within a biphasic sample

Therefore, we have to find a method to describe the flow of magnetic energy between the electron dipolar reservoir and the nuclear Zeeman reservoir in the RRP.

In section 2.2.2 we can see that, we added an extra nuclear spin reservoir, which contains only the nuclei directly coupled with electrons. In order to simplify the model, we can now treat the whole electron system together with the microwave irradiation as

a black box, whose function is the source of build-up and/or paramagnetic relaxation in the RRP, as illustrated in section 2.2.2.
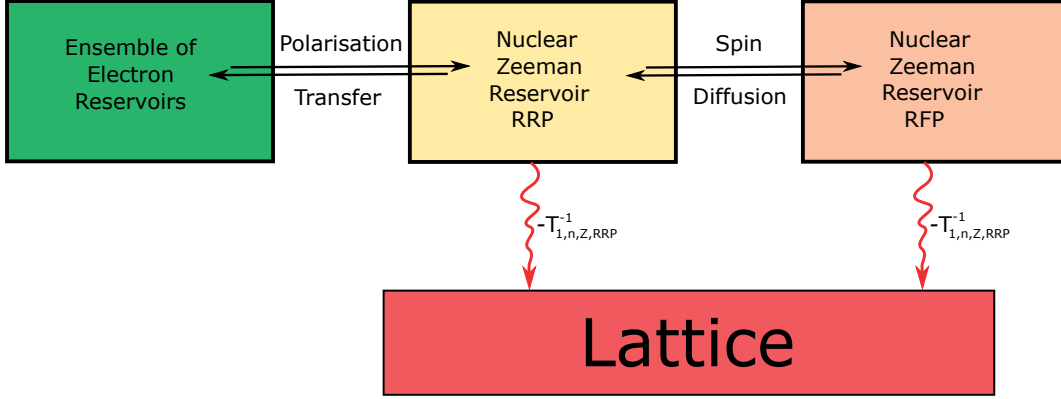

Figure 2.2 – An illustration of the simplified thermodynamic model of spin diffusion relayed DNP

Accordingly, we will have to amend the governing PDE of the system: A time/space-and-space-dependent source term $Q(\boldsymbol{r}, t)$ should be introduced.

$$d_a(\boldsymbol{r}) \cdot \frac{\partial}{\partial t} P(\boldsymbol{r}, t) = \nabla \cdot \left(\kappa(\boldsymbol{r}) \nabla P(\boldsymbol{r}, t) \right) + Q(\boldsymbol{r}, t) \tag{2.8}$$

Since $Q_i(\boldsymbol{r}, t)$ is still unknown, before solving the PDE, we need to determine the exact expression of source term.

Construction of Source Term

We start by considering the simplest case, where there is only a homogeneous RRP. We also introduce a further assumption that the spatial propagation of the polarisation within the nuclear spin reservoir is fast, so that the build-up of nuclear polarisation can be treated as homogeneous throughout the whole sample. In a normal d-DNP sample, the proton spin-diffusivity is on the order of 10^{-15} m^{2}s^{-1}[84]. When the concentration of the radicals is around 50 mM, the average distance between two radicals is around 10^{-8}m. In such a sample, the average characteristic time of spin diffusion is on the order of 1s, which is roughly of the same order of magnitude as the electronic longitudinal relaxation time. Therefore, this assumption could be reasonable.

In this example, we can thus infer that the spatial gradient of the nuclear polarisation vanishes: $\nabla \cdot (\kappa_i \nabla P(\boldsymbol{r}, t)) \equiv 0$, and the governing PDE reduces to:

$$\begin{cases} d_a \cdot \frac{\partial}{\partial t} P(t) = Q(t) \\ D = \frac{\kappa}{d_a} \\ d_a = C_p \cdot c \\ \frac{\partial}{\partial \boldsymbol{n}} P(t) = 0, \forall \boldsymbol{n} \in \partial\Omega \end{cases} \tag{2.9}$$

As shown in fig. 1.5, the build-up behaviour of the nuclear polarisation, $P(t)$, has a mono-exponential growth with a vanishing initial value:

We can then deduce the analytical expression of the source term $Q(t)$ for RRP under the assumption of a homogeneous mono-exponential growth:

$$\begin{cases} Q_{RRP}(t) = Q_{RRP,const} - Q_{RRP,lin}(t) \\ Q_{RRP,const} = q_{RRP} \times P_{\infty,RRP} \\ Q_{RRP,lin}(t) = q_{RRP} \times P_{RRP}(t) \\ q_{RRP} = \frac{d_{a,RRP}}{\tau_{Bup,RRP}} \end{cases} \tag{2.10}$$

where the constant part $Q_{RRP,const}$ represents the constant inward energy flow into the nuclear reservoir, and $Q_{RRP,lin}(t)$ represents time-dependent energy sink that refers to the rate of relaxation within the nuclear reservoir.

For the RFP, since the value of the polarisation at thermal equilibrium is negligible compared to the hyperpolarisation, we can drop the thermal equilibrium term for simplicity without significant loss of precision. The source term of RFP is then a simple analogue as in eq. (2.10):

$$\begin{cases} Q_{RFP}(t) = Q_{RFP,const} - Q_{RFP,lin}(t) \\ Q_{RFP,const} = q_{RFP} \times P_{\infty,RFP} = 0 \\ Q_{RFP,lin}(t) = q_{RFP} \times P_{RFP}(t) \\ q_{RFP} = \frac{d_{a,RFP}}{\tau_{Bup,RFP}} \end{cases} \tag{2.11}$$

So wehave obtained a complete PDE description of the dynamics of the system.

Spatial Discretisation of PDE

Because the RRP does not have the same spin concentration as the RFP, the spin diffusivity is different in the two phases. The direct consequence of such discontinuous physical properties is that, as previously stated in eq. (2.7c), the spatial distribution of the hyperpolarisation can only be continuous at the interface to the first order. The direct spatial discretisation of Laplacian, which is a second-order derivative of space, would lose its physical meaning. To solving this problem, we transform this classical second-order PDE to its corresponding weak form.

To begin with, we multiply both sides of the governing PDE by a test function $v(\boldsymbol{r})$:

$$
d_a(\boldsymbol{r}) \cdot \frac{\partial}{\partial t} P(\boldsymbol{r}, t) \cdot v(\boldsymbol{r}) = \nabla \cdot \big(\kappa(\boldsymbol{r}) \nabla P(\boldsymbol{r}, t) \big) \cdot v(\boldsymbol{r})
$$
$$
+ Q(\boldsymbol{r}, t) \cdot v(\boldsymbol{r}) \qquad\qquad , \boldsymbol{r} \in \Omega \qquad (2.12)
$$

Then we can perform integration on both side:

$$
\int_{\Omega} d_a(\boldsymbol{r}) \cdot \frac{\partial}{\partial t} P(\boldsymbol{r}, t) v(\boldsymbol{r}) dV = \int_{\Omega} \nabla \cdot \big(\kappa(\boldsymbol{r}) \nabla P(\boldsymbol{r}, t) \big) v(\boldsymbol{r}) dV
$$
$$
+ \int_{\Omega} Q(\boldsymbol{r}, t) \cdot v(\boldsymbol{r}) \cdot dV \qquad (2.13)
$$

With the *Divergence Theorem*, we then obtain the weak form of PDE:

$$
\int_{\Omega} d_a(\boldsymbol{r}) \cdot \frac{\partial}{\partial t} P(\boldsymbol{r}, t) v(\boldsymbol{r}) dV = \int_{\partial\Omega} \kappa(\boldsymbol{r}) v(\boldsymbol{r}) \cdot \nabla P(\boldsymbol{r}, t) \cdot dS
$$
$$
- \int_{\Omega} \kappa(\boldsymbol{r}) \nabla P(\boldsymbol{r}, t) \nabla v(\boldsymbol{r}) \cdot dV
$$
$$
+ \int_{\Omega} Q(\boldsymbol{r}, t) \cdot v(\boldsymbol{r}) \cdot dV \qquad (2.14)
$$

2.2.3 Simplification of the Model

In the previous subsection, we have formulated the dynamics of the nuclear reservoir during direct diffusion-relayed DNP in terms of a parabolic PDE with a series of constraints. The solution to this PDE is, however, not very straight-forward. The reason

lies primarily in the highly complex geometrical features of the biphasic samples.

From a macroscopic point of view, the RFP is the ensemble of grains of MOI. Since they result from mechanical grinding, the shapes of grains are all highly irregular. In addition, the random packing of thousands of irregular grains makes the situation even more complicated. It is the objective of this section to reduce the complexity of the geometry of our physical model.

As a the biphasic sample can be considered to be composed of an RFP comprised of MOI crystallites that are immersed in the RRP, *i.e.*, a solution of PA, we adopt a core-shell model where the RFP is placed inside a shell of RRP.
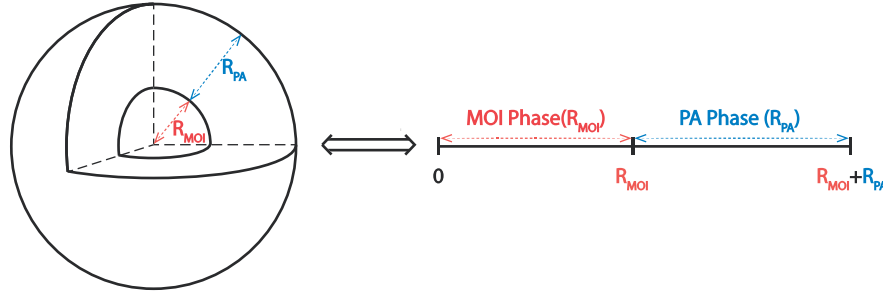

Figure 2.3 – An illustration of spherical core-shell model.

As shown in the right part of section 2.2.3, the random distribution of the RFP crystallites dispersed in the RRP is treated as a biphasic core-shell model. The radius of inner core, R_{MOI}, is the spherical-equivalent radius of RFP particles, which corresponds to a sphere of the same volume with respect to the mean volume of crystallites of MOI. The mean volume of the RFP crystallites can be determined by other techniques, such as scanning electron microscopy, X-ray computed microtomography, laser granulometry, or sieve analysis *etc.*. Since the volume ratio between the shell and the core equals the volume of solid powder of MOI and the volume of solution of PA. R_{PA}, can then be calculated from the sample formulation:

$$R_{PA} = \sqrt[3]{\frac{3\left(\frac{m_{MOI}}{\rho_{MOI}} + V_{PA}\right)}{4\pi}} - R_{MOI} \tag{2.15}$$

where m_{MOI} is the mass of the MOI powder, ρ_{MOI} is the theoretical density of MOI in crystalline form, and V_{PA} is the volume of solution of PA added in the biphasic sample.

With the spherical symmetry, we can even reduce the model into a one-dimensional model as the left part of section 2.2.3, under the condition that both the RRP and the RFP be isotropic and the tensor of spin diffusivity reduces into a scalar.

2.3 The Dynamics in Diffusion-Relayed CP-DNP

In the preceding section, we have established a simplified one-dimensional description of direct diffusion-relayed DNP under a series of assumptions:

- The build-up of nuclear polarisation be uniform throughout space;
- The complex geometry of sample could be expressed in a simple core-shell model;
- The spin-diffusivity be isotropic.

Now it is our job to extend the mathematical description to Diffusion-Relayed CP-DNP of low-γ nuclei. Since the sequence of Diffusion-Relayed CP-DNP(fig. 1.6) can be decomposed into a serial combination of direct Diffusion-Relayed DNP block and a CP block, our following narration is also divided into two parts. Here we limit the discussion in a nuclear system with only ^1H and ^{13}C, while the general principle can be applied to other nuclei.

2.3.1 The dynamics in direct DNP blocks

All the principles we developed in the preceding section still apply here:

$$
\begin{cases}
\boldsymbol{d_a}(\boldsymbol{r}) \circ \frac{\partial}{\partial t} \boldsymbol{P}(\boldsymbol{r}, t) = \nabla \left(\boldsymbol{\kappa}(\boldsymbol{r}) \circ \left(\nabla \boldsymbol{P}(\boldsymbol{r}, t) \right) \right) + \boldsymbol{Q}(\boldsymbol{r}, t) \\
\boldsymbol{\kappa}(\boldsymbol{r}) = \boldsymbol{D}(\boldsymbol{r}) \circ \boldsymbol{d_a}(\boldsymbol{r}) \\
\boldsymbol{d_a}(\boldsymbol{r}) = \boldsymbol{C_p}(\boldsymbol{r}) \circ \boldsymbol{c}(\boldsymbol{r})
\end{cases}
\tag{2.16a}
$$

$$
\frac{\partial}{\partial \boldsymbol{n}} \boldsymbol{P}(\boldsymbol{r}, t) = 0, \forall \boldsymbol{n} \in \partial \Omega_{Out}
\tag{2.16b}
$$

$$
\lim_{\boldsymbol{r} \to \partial \Omega_{In}} \boldsymbol{P}(\boldsymbol{r} \in \Omega_{RFP}, t) = \lim_{\boldsymbol{r} \to \partial \Omega_{In}} \boldsymbol{P}(\boldsymbol{r} \in \Omega_{RRP}, t)
\tag{2.16c}
$$

$$
- \lim_{\boldsymbol{r} \to \partial \Omega_{In}} \kappa_{RFP} \cdot \nabla \boldsymbol{P}(\boldsymbol{r} \in \Omega_{RFP}, t) = \lim_{\boldsymbol{r} \to \partial \Omega_{In}} \kappa_{RRP} \cdot \nabla \boldsymbol{P}(\boldsymbol{r} \in \Omega_{RRP}, t)
\tag{2.16d}
$$

$$
\boldsymbol{P}(\boldsymbol{r}, t = 0) = 0, \forall \boldsymbol{r} \in \Omega
\tag{2.16e}
$$

where $\boldsymbol{P}(\boldsymbol{r}, t) = \left(P^H(\boldsymbol{r}, t), P^C(\boldsymbol{r}, t) \right)^\top$ is the polarisation vector of nuclear system, $\boldsymbol{Q}(\boldsymbol{r}, t) = \left(Q^H(\boldsymbol{r}, t), Q^C(\boldsymbol{r}, t) \right)^\top$ is the vector of source term, $\boldsymbol{d_a}(\boldsymbol{r}, t) = \left(d_a{}^H(\boldsymbol{r}, t), d_a{}^C(\boldsymbol{r}, t) \right)^\top$ is the vector of the damping factor, $\boldsymbol{\kappa}(\boldsymbol{r}, t) = \left(\kappa^H(\boldsymbol{r}, t), \kappa^C(\boldsymbol{r}, t) \right)^\top$ is the vector of the spin conductivity, $\boldsymbol{D}(\boldsymbol{r}, t) = \left(D^H(\boldsymbol{r}, t), D^C(\boldsymbol{r}, t) \right)^\top$ is the vector of the spin diffusivity, $\boldsymbol{C_p}(\boldsymbol{r}, t) = \left(C_p{}^H(\boldsymbol{r}, t), C_p{}^C(\boldsymbol{r}, t) \right)^\top$ is the vector of the heat capacity, and $\boldsymbol{c}(\boldsymbol{r}, t) = \left(c^H(\boldsymbol{r}, t), c^C(\boldsymbol{r}, t) \right)^\top$ is the vector of the spin concentration.

The binary operator $\circ$ here denotes the Hadamard product of tensors, which is defined as an entry-wise product of two tensors of the same dimension. For $\boldsymbol{x} = (x_1, \cdots, x_n)^\top$ and $\boldsymbol{y} = (y_1, \cdots, y_n)^\top$, we have $\boldsymbol{x} \circ \boldsymbol{y} \overset{def}{=\!=} (x_1 y_1, \cdots, x_n y_n)^\top$

Like what we did in eq. (2.14), in our numerical treatment, the governing PDE is also converted in its weak form.

$$
\begin{cases}
\int\limits_{\Omega} d_a{}^H(\boldsymbol{r}) \cdot \frac{\partial}{\partial t} P^H(\boldsymbol{r},t) v(\boldsymbol{r}) dV & = \int\limits_{\partial\Omega} \kappa^H(\boldsymbol{r}) v(\boldsymbol{r}) \cdot \nabla P^H(\boldsymbol{r},t) \cdot dS \\
& \quad - \int\limits_{\Omega} \kappa^H(\boldsymbol{r}) \nabla P^H(\boldsymbol{r},t) \nabla v(\boldsymbol{r}) \cdot dV \\
& \quad + \int\limits_{\Omega} Q^H(\boldsymbol{r},t) \cdot v(\boldsymbol{r}) \cdot dV \\
\int\limits_{\Omega} d_a{}^C(\boldsymbol{r}) \cdot \frac{\partial}{\partial t} P^C(\boldsymbol{r},t) v(\boldsymbol{r}) dV & = \int\limits_{\partial\Omega} \kappa^C(\boldsymbol{r}) v(\boldsymbol{r}) \cdot \nabla P^C(\boldsymbol{r},t) \cdot dS \\
& \quad - \int\limits_{\Omega} \kappa^C(\boldsymbol{r}) \nabla P^C(\boldsymbol{r},t) \nabla v(\boldsymbol{r}) \cdot dV \\
& \quad + \int\limits_{\Omega} Q^C(\boldsymbol{r},t) \cdot v(\boldsymbol{r}) \cdot dV
\end{cases}
$$

It is worthy to note that, for a diffusion-assisted DNP block that follows a CP block, the initial value should be the result of the precedent CP block.

2.3.2   The dynamics in CP blocks

Theoretically, during the whole CP process, the build-up and relaxation of polarisation, the spin diffusion and the equilibration of nuclear magnetic energy between two nuclear reservoirs all occur simultaneously. The thermal mixing under the nuclear Hartmann-Hahn condition (on the order of a few milliseconds) proceeds, however, much faster than both the build-up of nuclear polarisation and its diffusion of nuclear polarisation (both occur on time scales on the order of 100-1000 seconds). In the treatment of CP, we can therefore neglect both the build-up and spin diffusion. The nuclear thermal mixing during spin-locking can be described by the master equation:

$$
\frac{\partial}{\partial t} \boldsymbol{P} = \mathbf{W} \cdot \boldsymbol{P} \tag{2.17}
$$

where $\mathbf{W}$ is the matrix of transition probability.

An explicit expression of transition matrix can be obtained after some easy algebra[85, 35]:

$$
\mathbf{W} = \begin{pmatrix} -\frac{1}{T_{1\rho}^H} - \overline{b_{H-C}} \cdot \frac{c^C}{c^H + c^C} & \overline{b_{H-C}} \cdot \frac{c^C}{c^H + c^C} \\ \overline{b_{H-C}} \cdot \frac{c^H}{c^H + c^C} & -\frac{1}{T_{1\rho}^C} - \overline{b_{H-C}} \cdot \frac{c^H}{c^H + c^C} \end{pmatrix} \tag{2.18}
$$

where $T_{1\rho}^H$ and $T_{1\rho}^C$ are the longitudinal relaxation times in the rotating frame of proton and of carbon-13, c^H and c^C are the spin densities of the protons and of carbon-13, and b_{H-C} is the average heteronuclear dipolar coupling between protons and carbon-13.

The initial condition of the CP block is always set equal to the numerical result of preceding direct build-up block.

It is worthy to note that this discussion focuses at the simple Hartmann-Hahn type experiment: no advanced schemes, such as, RAMP ,*etc.*, are considered.

2.4 Determination of Numerical Values of Physical Properties

Before launching numerical simulations, we still have to define the values of all above-mentioned parameters that are required for the numerical simulations. Here we only briefly introduce the formulae of the calculations. All the quantities in SI units are detailed in appendix A.1.1. The choice of the parameters can be somewhat idealised, since they merely serve as a point of departure of some qualitative discussions.

Molar Energy Capacity
The value of the capacity of magnetic energy per one mole of spins can be derived from eq. (2.5). This value is $5.69 \cdot 10^{-2}$ J·mol^{-1} for protons, and $1.43 \cdot 10^{-2}$ J·mol^{-1} for carbon-13.

Spin density
The value of the spin density in each phase can be calculated from eq. (2.19).

$$\begin{cases} c^H \stackrel{def}{=\!=\!=} \frac{n^H \rho \cdot 10^6}{M_M} \\ c^C \stackrel{def}{=\!=\!=} \frac{\rho \cdot 10^6}{M_M}(n^C + 0.011 \cdot n^{C'}) \end{cases} \qquad (2.19)$$

where c^H and c^C are the spin densities of protons and carbon-13, ρ is the density at standard conditions of a given compound, M_M is the molecular mass of a given compound, n^H is the number of protons in the molecular formula of a given compound, n^C is the number of labelled carbon-13 nuclei in the molecular formula of a given compound, $n^{C'}$ is the number of carbon-13 in natural abundance in the molecular formula of the compound.

When treating a mixture, like the PA in the RRP, the spin density of this glassy mixture is taken to be the weighted arithmetic mean of the spin densities of all components based on their relative volumetric percentage. This approximation is based on two

assumptions: one is that during the phase transition from the liquid state to the frozen glass the volume of the solvents does not vary in a significant manner. On the other hand, the partial molar volume of each component in the mixture is negligible, so that the volume of the mixture can be considered as a linear addition of all components. Generally speaking, for the a mixture of toluene and THF at a volumetric ratio of of 8:2, as in the RRP we wish to simulate, these conditions are met without significant errors.

Damping factor

The damping factor of each phase can be determined by multiplying its molar energy capacity and its spin density, as indicated in eq. (2.6b).

Spin diffusivity

The value of the spin diffusivity can be determined by different methods: either by experimental measurements [86, 87, 84], by theoretical calculations from the first-principle [80], or by empirical estimation. In our context, we focus on an empirical estimate.

This estimate starts from the spin diffusivity of protons in polystyrene measured by Meyer *et al.* [84], which is $D_{PS}^H = 3.8 \cdot 10^{-15}$ m^2·s^{-1}. Based on the cubic scaling rule[88] and assuming that all solids that we treat in this simulation are amorphous, we can access to the numerical values of other glassy solids:

$$D^H = D_{PS}^H \cdot \sqrt[3]{\frac{c^H}{c_{PS}^H}} \tag{2.20}$$

Of course, the spin diffusivity in anisotropic crystalline environments should be described by a tensor rather than by a scalar value.

The estimation of the spin diffusivity of carbon-13 can be obtained from a less direct way. According to the dimensional analysis by Abragam [33], the spin diffusivity can be calculated from the transition probability (W) and the average minimal distance between two like-spins ($\overline{a}_{min}$):

$$D = W \cdot \overline{a}_{min}^2 \tag{2.21}$$

In a sample of adamantane, Bronniman *et al.*[89] have measured the transition probability among nuclei of aliphatic carbon-13 nuclei under proton-driven spin diffusion in a sample of adamantane at natural abundance as $W_{Adamantane} = 0.781\text{s}^{-1}$. From the density of adamantane we can derive the Wigner–Seitz radius [90] of ^{13}C spins:

$$\frac{4\pi}{3}\left(\frac{\overline{a}_{min}}{2}\right)^3 \frac{\rho \cdot N_A \cdot 0.011}{M_M} = 1$$
$$\implies \overline{a}_{min} = 3.8 \cdot 10^{-9}\text{m} \tag{2.22}$$

Now we have $D_{Adamantane} = 8.56 \cdot 10^{-18}$ m$^2 \cdot$s^{-1}.

As reported by Goldman and Jacquinot [91], the proton-driven spin diffusivity follows the proportionality of D is proportional to $N^{4/3}$. We can derive the proton-driven spin diffusivity as a function of the concentration of the low-γ spins:

$$D^C = D^C_{Adamantane} \cdot \left(\frac{c^C}{c^C_{Adamantane}}\right)^{4/3} \tag{2.23}$$

Because of the inhomogeneous broadening of the absorption line shape, for example due to CSA broadening, the spin diffusivity should generally be smaller than the value predicted by eq. (2.23).

When it comes to estimating spin diffusivity in crystals, as stated in previous paragraphs, we can not directly adopt the scaling rule. The remedy also comes from the dimensional analysis in eq. (2.21). As a primary approximation, however, we start by assuming that the spin diffusion in crystals obeys the same scaling rule as in those glassy matrices, so as to obtain a value as a point of departure of qualitative results.

Spin conductivity
By analogy to the thermal conductivity in heat conduction, the spin conductivity is defined as the product of spin diffusivity and the total damping factor, as in eq. (2.6c).

Build-up time constants
The time constants of build-up processes can be determined by mono-exponential fits of experimental data. Normally, for a water-glycerol based sample, this constant is roughly on the order of 100-300 seconds, depending on the proton concentration and the radical concentrations in the sample. For a toluene based sample, this time constant is on the order of 30-120 seconds. In the RFP, there are no radicals, and the solid of MOI cannot be polarised. This concept is thus not applicable.

The actual time constant used in simulation is set to be 65.4 s for protons, based on experimental observations. For carbon-13, we assume the time constant to be 1800 s.

Longitudinal Relaxation Times in the Laboratory Frame

Since the nuclear longitudinal relaxation times vary as a function of the polarisation of the electronic spins in their neighbourhood, the longitudinal relaxation times that are used in the numerical simulations refer specifically to the time constants of the nuclear spins in the absence of microwave irradiation, reflecting the situation where our experiments were conducted. For the RRP, the longitudinal relaxation times of protons are obtained from the saturation-recovery experiments, and they are found to be on the order of 100 s. For the crystalline RFP, since the longitudinal relaxation times of protons are usually too long to be measured from experiments, and we arbitrarily assume $T_1(^1H) = 6000$ s. Further, for ^{13}C, the the longitudinal relaxation times in the RRP are around 2400 s, and the the longitudinal relaxation times in the RFP is assumed to be in the vicinity of 36000 s

Maximum Polarisation
The maximum polarisation can be fitted from the data of a build-up experiments. It represents the value of the asymptote line, towards which the exponential growth approaches. In an initial stage, we determine $P(^1H) = 68\%$ for the proton polarisation in the RRP from experimental fits. According to the theory of thermal mixing of the DNP process, all species of nuclear spins arrive at a common spin temperature in the steady state, so we can determine the carbon-13 polarisation to be $P(^{13}C) = 21\%$.

Heat Source
The numerical values of the heat source are estimated from the eq. (2.11), along with all the above-mentioned values.

Average Dipolar Coupling
The average dipolar coupling is used to describe the speed of transfer of nuclear magnetic energy between distinct nuclear spin reservoirs during the process of cross polarisation. This parameter can be determined either by experiments for different spin-locking times during the CP process, or simply approximated from the formula of dipolar interactions (eq. (1.6)) with data from X-ray diffraction.

In our simulations, the average dipolar coupling in the RRP is set to be equal to the heteronuclear dipolar coupling for a one-bond distance, around 9000 Hz. In the XRD structure of (1-^{13}C)-sodium pyruvate, the nearest distance between a labelled carbonyl group and A methyl proton is around 2.7 angstroms, so that the corresponding b_{H-C} is around 2000 Hz. In the (U-^{13}C)-glycine, there are both aliphatic and carbonyl carbons, and we adopted an arithmetic average of 5500 Hz

The average dipolar coupling can also be obtained by fitting to the dynamics of the

CP process, as discussed by Bornet *et al.*[92].

Longitudinal Relaxation Times in the Rotating Frame
The longitudinal relaxation times in the rotating frame have a significant influence on the final result of cross polarisation. According to experimental observations, the $T_{1\rho}$ is on the range of 100-microseconds to 10-milliseconds, depending on the cristallinity of the solid phase, the electron polarisation, and many other factors. As a rough attempt, we use some typical values for the qualitative simulations. The data for protons in the RRP are obtained from reference [92]. The values of $T_{1\rho}^C$, for the moment,are set to be identical with respect to $T_{1\rho}^H$

For the values of $T_{1\rho}$ in the RFP, it is considered to be long enough to be neglected on the time-scale of the CP process in a liquid helium bath, because of the negligible magnetron-phonon couplings in highly periodical structures at low temperatures.

2.5 Results of Numerical Simulations and Discussion

2.5.1 Time-dependent distribution of the proton polarisation during diffusion-relayed DNP process

Having built-up the physical model underlying our numerical simulations, in this section we focus on the qualitative features concerning the diffusion-relayed DNP process. We start with three examples in fig. 2.4, fig. 2.6, and fig. 2.5. On a first glance, we see that the build-up rate of the proton polarisation in the system is closely connected with three factors in the experiments: the size of the particles in the RFP, the volumetric ratio between the PAs and the MOIs, and the deuteration level of the RRP. We collected the extensive dataset from simulations to investigate the roles of these factors.

From the fig. 2.7, we can see that the diffusion-relayed DNP process permits a satisfactory build-up in particles of spin glasses, on the condition that the diameter of equivalent spheres of the RFP does not exceed 1 μm. In this case, after a 30-minute-long DNP process, the polarisation of the MOI can almost reach almost the same level as the RRP itself. If the diameter of the MOI grains grows, the maximum polarisation that we can obtain during the process gradually decreases. Meanwhile, we starts to observe a multi-exponential patterns in the calculated build-up curve of the whole system.

On the other hand, the spin diffusion has its inherent limits. As we can see in fig. 2.7, the build-up of hyperpolarisation in the particles with diameters above 5 μm is not very efficient within a reasonable time span, *ca.* 30 minutes. This might be explained by considering that the penetration of hyperpolarisation into the RFP can not exceed

a depth of 5 μm, which leads us to an estimate an upper limit of the particle size for optimal performance in diffusion-relayed DNP experiments.

Similar numerical researches has also been conducted by varying the thickness of the RRP layer (see fig. 2.8). Interestingly, the results of these simulations shows that we do not really require a very thick shell of RRP that coats the crystalline grains. In order to obtain the best performance in a particle with a radius of 5 μm, a layer of RRP with thickness of 300 nm is often more than enough. Beyond such a thickness, any surplus of RRP hardly contributes to polarising the particles of MOI. We can thus consider two different regimes: when the thickness of the layer of the PA is less than 100 nm, the process of hyperpolarisation is mainly limited by the overall cooling power of the RRP; when the thickness of the layer of the PA is greater than 300 nm, the diffusion-relayed DNP process is mainly controlled by the efficiency of spin diffusion.

As indicated in fig. 2.8, the distinct build-up profiles due to spin-diffusion in two equivalent spin glasses also raised much interest for the role of concentration of proton spins in multi-phasic spin diffusion. The equivalent spin glass of glycine (fig. 2.8b) is more sensitive to the thickness of RRP layer than an equivalent spin glass of sodium pyruvate (fig. 2.8a). This observation lead to further numerical experiments to study the influence of spin concentrations on spatial diffusion in biphasic systems. When considering the same final polarisation levels and the polarisation time constants for RRPs for different extents of deuteration, we obtained fig. 2.9 .

From the tendencies in fig. 2.9a and fig. 2.9b, we can see that the highest hyper-polarisation in the RFP is obtained for the least deuterated case. This phenomenon could be explained by two reasons. First, since we chose the identical build-up time constants for all the five cases, according to eq. (2.10) and eq. (2.6), the higher concentration of spin in the RRP, the higher the cooling power that we can benefit from to polarise the whole system. Second, the rate of the spatial propagation of nuclear magnetic energy depends on the spin concentration, since the spin diffusivity is proportional to the cubic root of the proton concentration. This means that a higher proton concentration allows a thicker layer of RRP to be involved in the build-up process of the MOI particles, which in turn enhances the performance of overall build-up of the RFP.

By revisiting the transmission boundary condition of this biphasic problem eq. (2.7c), we could gain some semi-quantitative insights. In order to maintain the conservation of magnetic energy in the system, the outward flow of magnetic energy from the RRP must be equal to the inward flow into the RFP. By definition, the amplitude of the flow is the product of the gradient of nuclear polarisation and the spin conductivity, where the latter is proportional to the spin density to the power of 4/3. As a result, a higher spin density favours the energy flow from the RRP to the RFP at the interface, and therefore accelerates the spin diffusion.

The conditions of actual scenarios, however, are not exactly the same as those

of the above-mentioned simulations. The most significant discrepancy is due to that we do not always have identical values of the polarisation when the deuteration level is altered. Generally speaking, when keeping the same concentration of radical and when working at the same temperature of the helium bath, we always have less polarisation in RRP when the deuteration level is decreased. The choice of the chemical composition of the system thus requires some careful consideration. a trial-and-error approach can yield a compromise between cooling power in thermal mixing and spin diffusion.

As shown in fig. 2.9a, as long as the proton concentration in the RRP being higher than the proton concentration of the RFP, the utility of a further increase of proton spin density in RRP becomes less appealing. The main limiting factor in this case is the flow at the interface rather than the generation of hyperpolarisation in the RRP. We can then play with the deuteration level in the RRP to achieve a better and faster polarisation level in RRP at steady-state, which ensures a optimised gradient of the nuclear polarisation and consequently an optimised flow of energy. On the contrary, for an MOI phase like glycine, which has a relatively high proton concentration, we have reasons to perform more experimental attempts searching for the optimal experimental condition.

In the ideal situation, we should have the fastest proton diffusion for high proton concentration and a high final polarisation in RRP. The trade-off between the deuteration and the final polarisation in RRP could be applied when the MOI is not rich in protons. For the same object, the diameter of the MOI particles would be no more than 5 μm. Otherwise, the proton spin diffusion would become utterly inefficient.
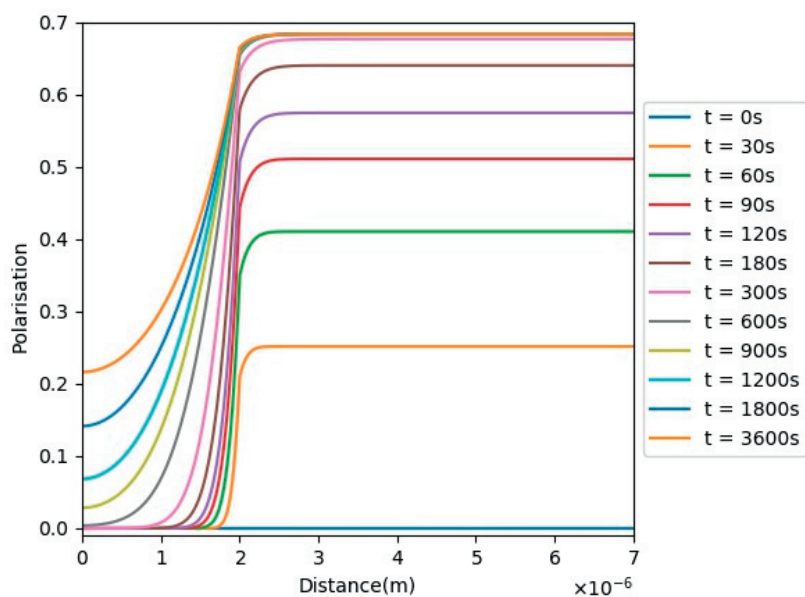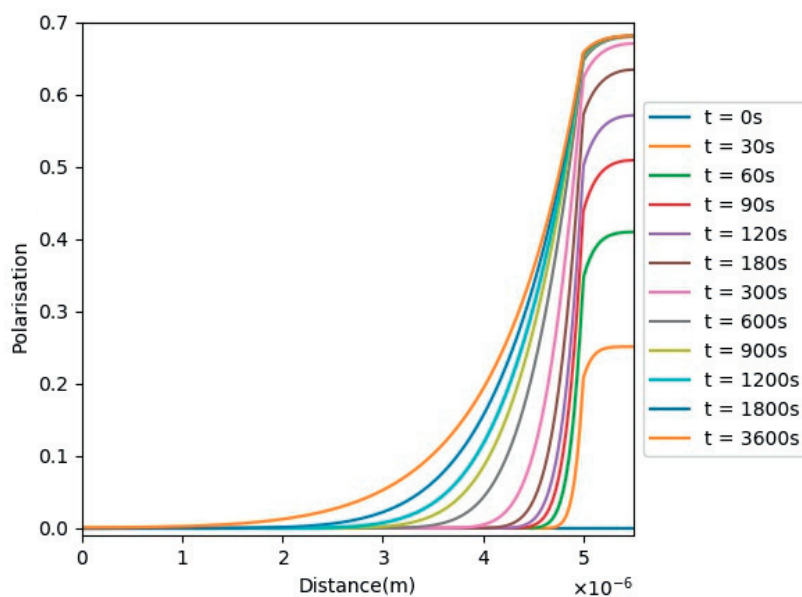
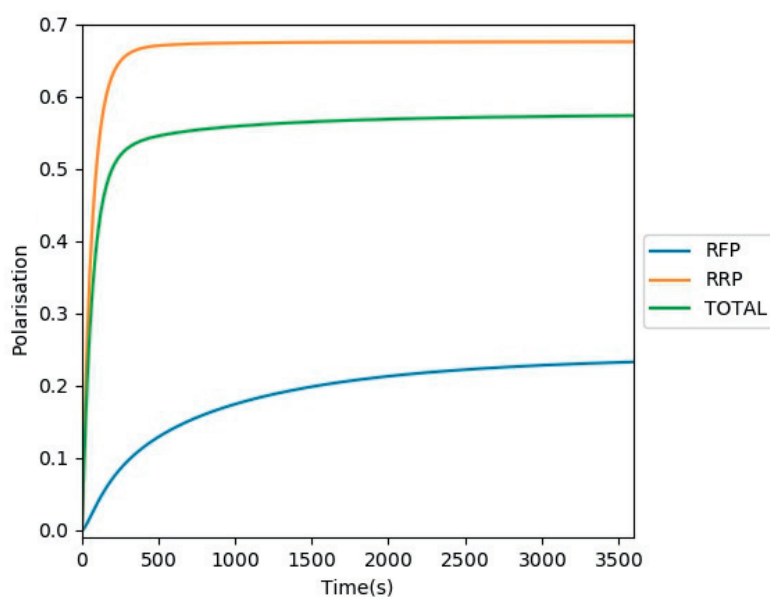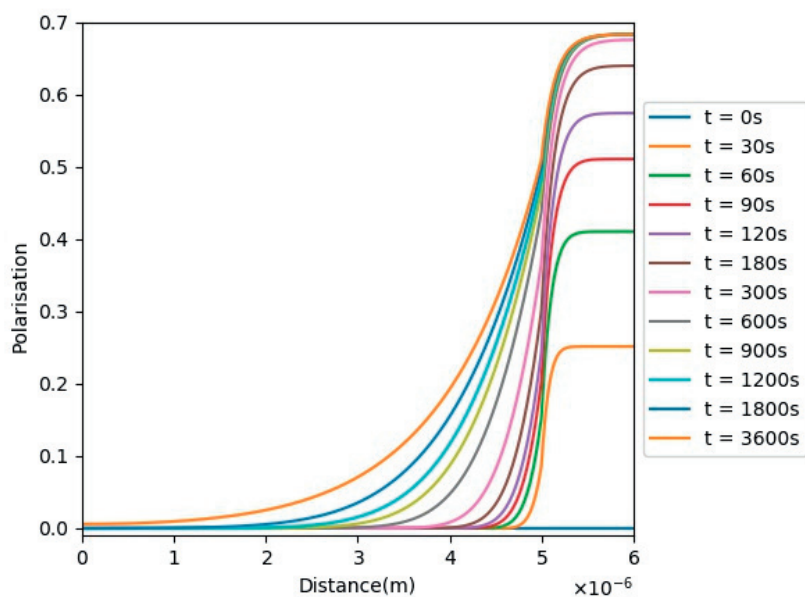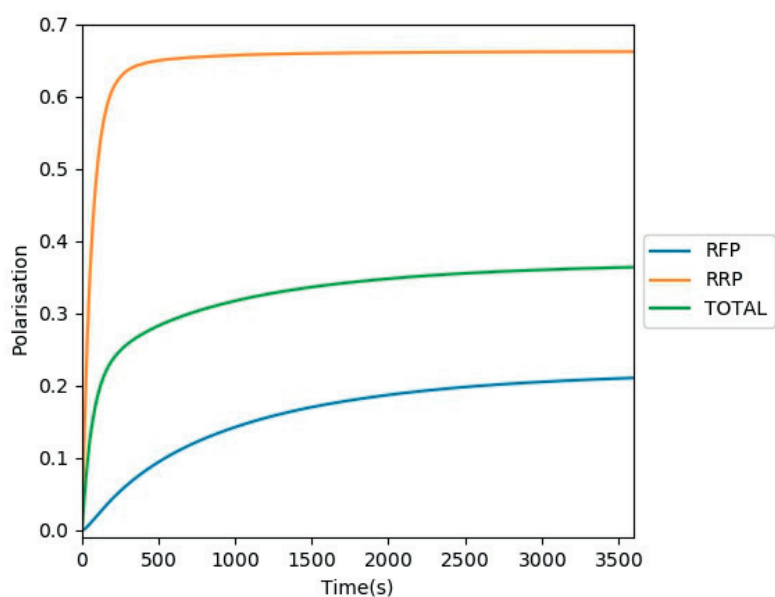(a) Spatial distribution of proton hyperpolarisation.
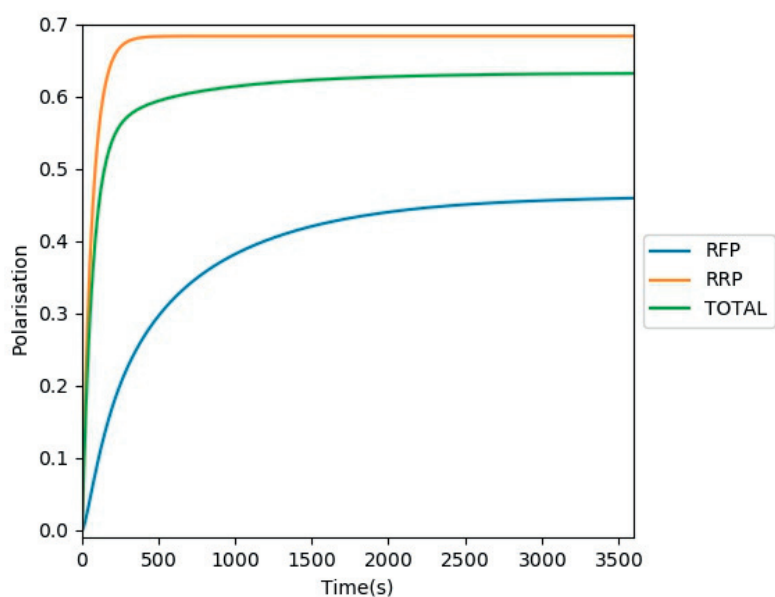
(b) Build-up curves of proton hyperpolarisation

Figure 2.4 – Simulated time-dependent propagation of proton hyperpolarisation during the diffusion relayed DNP.The RFP is an equivalent spin glass of sodium pyruvate, where the proton spin density is 33 mol·L^{-1}. The RRP is a 100% protonated spin glass, where the proton spin density is 110 mol·L^{-1}. The effective Wigner–Seitz radius is 2.5 µm for the RFP and the effective thickness is 5 µm for RRP.

(a) Spatial distribution of proton hyperpolarisation.

(b) The Build-up curves of proton hyperpolarisation

Figure 2.5 – Simulated time-dependent propagation of proton hyperpolarisation during diffusion-relayed DNP.The RFP is a equivalent spin glass of glycine, where the proton spin density is 107 mol·L^{-1}. The RRP is a 100% protonated spin glass, where the proton spin density is 110 mol·L^{-1}. The effective Wigner–Seitz radius is 5 µm for the RFP and the effective thickness is 500 nm for the RRP.

(a) Spatial distribution of proton hyperpolarisation.

(b) Build-up curves of proton hyperpolarisation

Figure 2.6 – Simulated time-dependent propagation of proton hyperpolarisation during the diffusion relayed DNP.The RFP is a equivalent spin glass of glycine, where the proton spin density is 107 mol·L^{-1}. The RRP is a 50% protonated spin glass, where the proton spin density is 55 mol·L^{-1}. The effective Wigner–Seitz radius is 2 µm for the RFP and the effective thickness of 1 µm for the RRP.
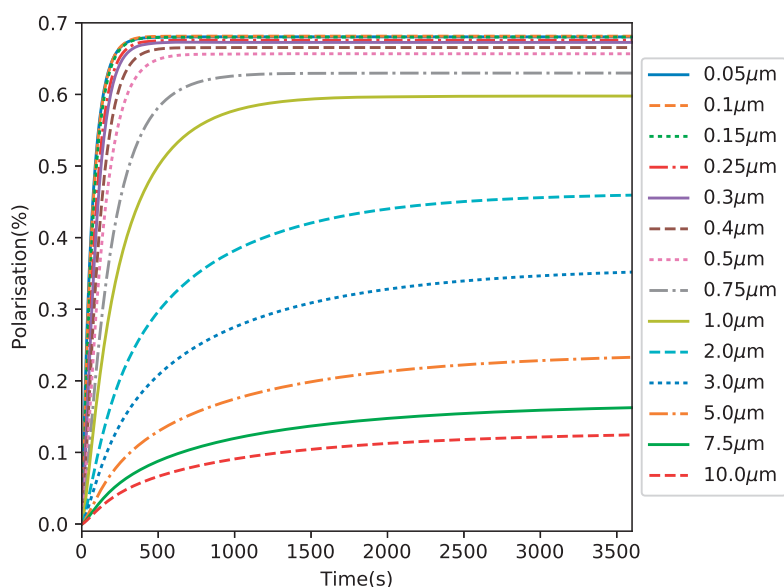
(a) Time-dependence of the proton polarisation of an equivalent spin glass of sodium pyruvate.
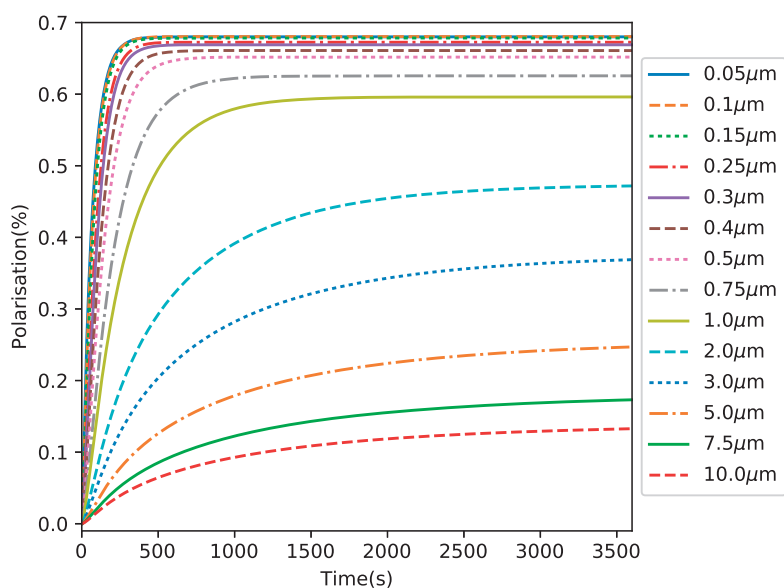
(b) Time-dependence of the proton polarisation of an equivalent spin glass of glycine.

Figure 2.7 – Simulated time-dependent build-up curves of proton polarisation in particles of RFP with different radii. The thickness of RRP shell is constant and equal to 5 µm in all simulations. Both phases are considered as fully protonated.
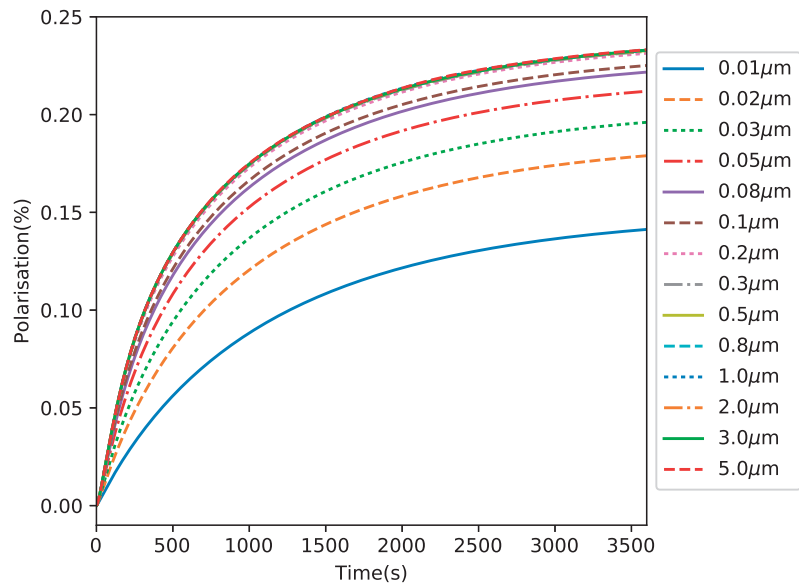
(a) Time-dependence of the proton polarisation of an equivalent spin glass of sodium pyruvate.
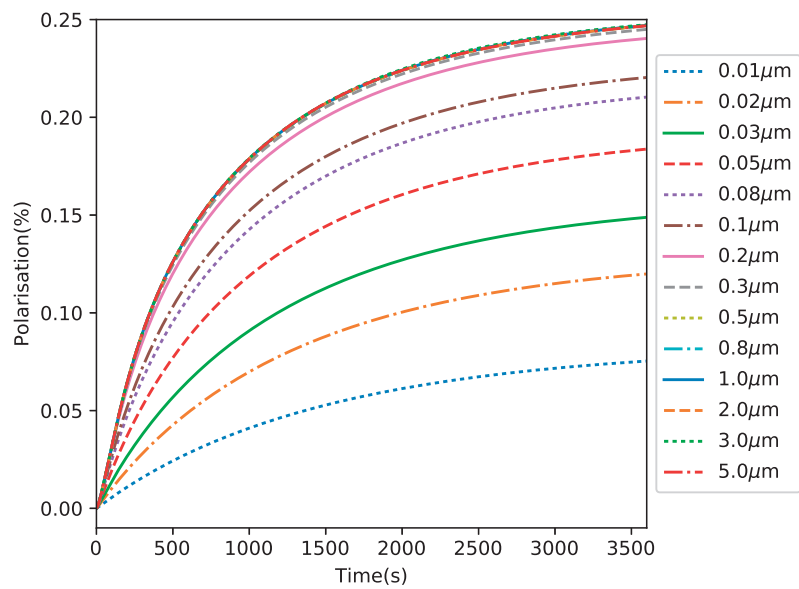

(b) Time-dependence of the proton polarisation of an equivalent spin glass of glycine.

Figure 2.8 – Simulated time-dependent build-up curves of proton polarisation in particles of RFP as a function of the thickness of the layer of RRP. The radius of the MOI particles is equal to 5 μm in all simulations. Both phases are considered as fully protonated.
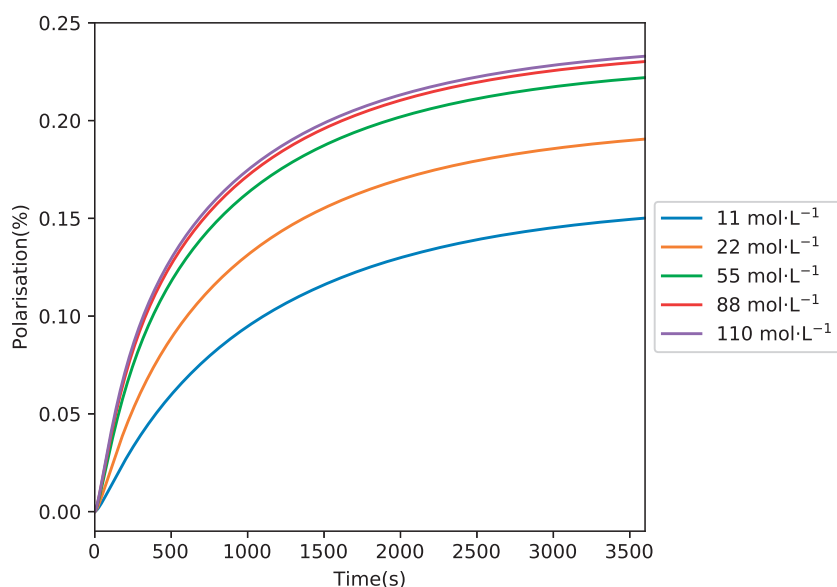
(a) Time-dependence of the proton polarisation of an equivalent spin glass of sodium pyruvate.
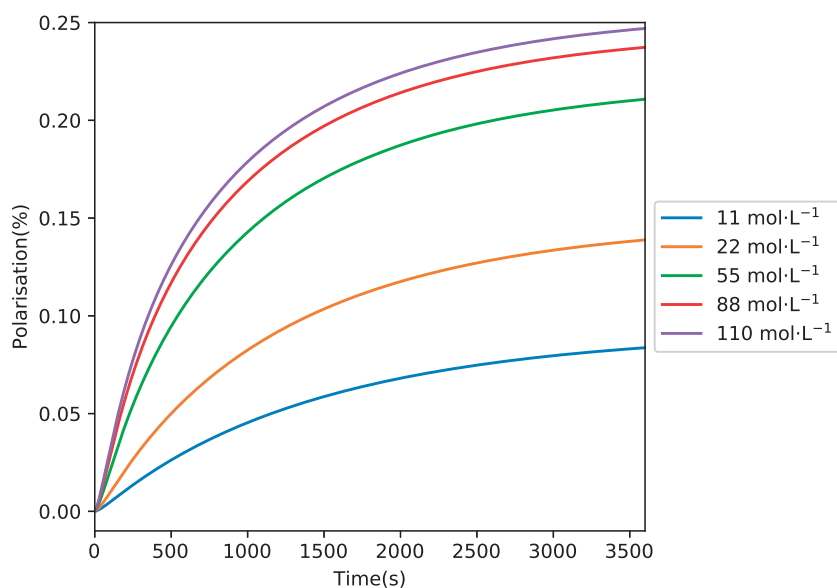

(b) Time-dependence of the proton polarisation of an equivalent spin glass of glycine.

Figure 2.9 – Simulated time-dependent build-up curves of proton polarisation in particles of RFP for different proton concentrations in the RRP. The radius of RFP core is constant and equal to 5 µm and the thickness of RRP layer is 1 µm in all the simulations. All the RFPs are fully protonated.

2.5.2 Time-dependent distribution of nuclear polarisation during diffusion-relayed CP-DNP process

The evolution of the nuclear polarisation during one block of the CP-DNP process

Our attention will now focus on the combination of proton diffusion with the thermodynamic model of CP, so as to visualise the details of the CP-build-up process. Before diving into the global performance of whole CP-DNP process, we first examine how the system evolves in a single block (as illustrated in fig. 2.13).

According to the classic thermodynamic model of cross polarisation, the spin temperatures of two nuclear spin reservoirs converge towards to a common value under the influence of longitudinal relaxation in the rotating frame. In our case, the evolution is a bit more complicated. Due the high radical concentration in the RRP, $T_{1,\rho}^{RRP}$ is much shorter than $T_{1,\rho}^{RFP}$. This directly leads to a difference between two independent evolution profiles of the hyperpolarisation in the two phases respectively. In view of obtaining the highest possible carbon polarisation in the RFP at the end of the composite process, we guess, at this moment, that the best spin-locking contact time for spin-lock, which equals to 2.5 ms, remains the same throughout the experiment. Using this value, we can simulate complete build-up profiles at intervals of 300 seconds between two consecutive CP blocks, as shown in fig. 2.11.

The evolution of nuclear polarisation during the whole CP-DNP process

The effect of the interval between CP contact in CP-DNP process From fig. 2.11, we can see that the polarisation in the RRP reaches its equilibrium on a very short time-scale. On the other hand, the carbon-13 polarisation inside the grains of the MOI grows more slowly. This slow increase arrives at a steady state when the spatial replenishment of the proton polarisation by proton spin diffusion between the two phases becomes comparable compared to the loss during the transfer of magnetic energy between the two nuclear reservoirs. As the accumulation of proton polarisation in the RFP by diffusion is also time-dependent, our next simulations focuses on the effect of the length of interval between two successive CP blocks.

fig. 2.12a shows the evolution of the carbon-13 polarisation in the RFP during the CP-DNP build-up for different intervals within a fixed overall duration of two hours. The envelope of the CP-DNP build-up curve demonstrates the dependence of the final yield of carbon-13 polarisation on the time-interval between CP. Evidently, the longer the interval, the higher the overall carbon-13 polarisation in the MOI would be.

This argument is supported by the envelope of the proton build-up curve. Since in the RFP the longitudinal relaxation time is very long compared to the time-scale of the spin-locking, we can almost neglect the loss of relaxation during the spin-lock of cross polarisation. In a polarising experiment with infinite time, the envelope of proton

polarisation right before the contact of cross polarisation will eventually coincide with the envelope of the proton polarisation right after spin-lock. In fig. 2.12c, we can see that over a two-hour-long evolution, the two envelopes for the five-minute CP intervals starts to merge, while the pair of lines indicate that for the thirty-minute intervals they are still away from each other. We can then safely conclude that, shorter intervals between CP contacts might perform better as a compromise between time and polarisation. Nevertheless, to maximise the polarisation in the RFP, aiming at remote polarisation, long gaps between consecutive spin-locks and a long overall duration of the experiments would be necessary. A reasonable interval of 300-900 s would be enough.

The influence of average particle size of the MOI on the performance of CP-DNP process As in section 2.5.1, we are also interested in the relation between particle size and the performance of CP-DNP process.

The simulated CP-DNP build-up curves in fig. 2.13 strongly favours the particles with a diameter smaller than 1 μm, which nicely corresponds with the simulations of direct proton spin diffusion.

For particles with small diameters, since the direct proton spin diffusion is very efficient, so that we do not need long intervals between consecutive CP contacts to replenish the magnetic energy in proton manifold of the RFP. Larger particles require longer intervals to build up the proton polarisation. Once the diameter of the particles exceeds 10 μm. the intervals between consecutive CP contacts no longer plays an important role, because in this regime, the efficiency of proton spin diffusion becomes the dominant factor.
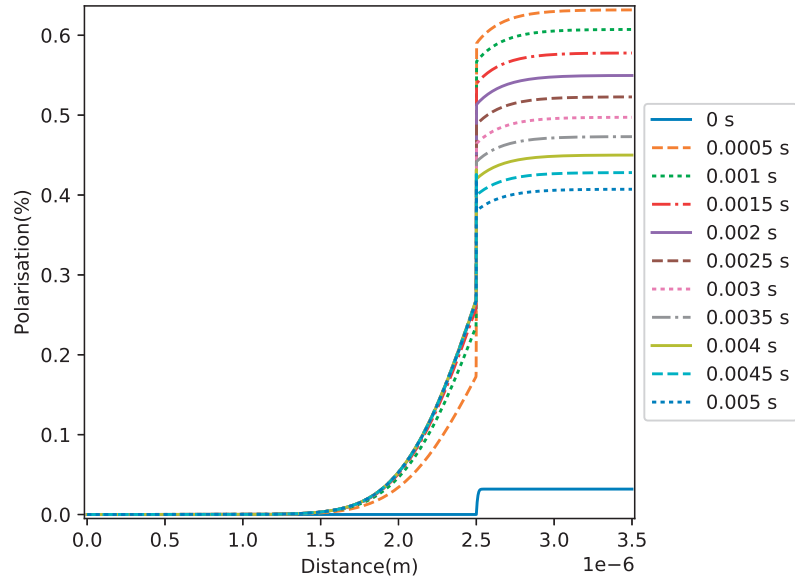
(a) Evolution of spatial distribution of carbon-13 polarisation in a biphasic model.
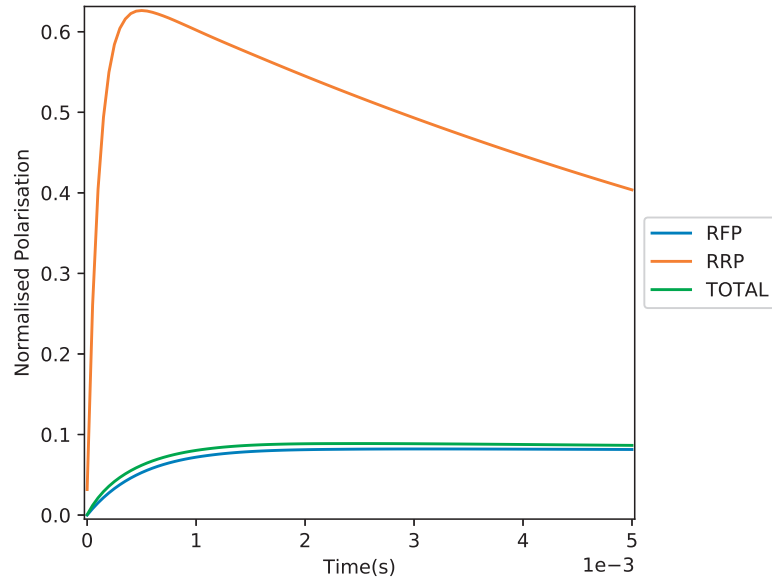
(b) Time-dependence of carbon-13 polarisation in a biphasic model.

(c) Evolution of spatial distribution of carbon-13 polarisation in a biphasic model.
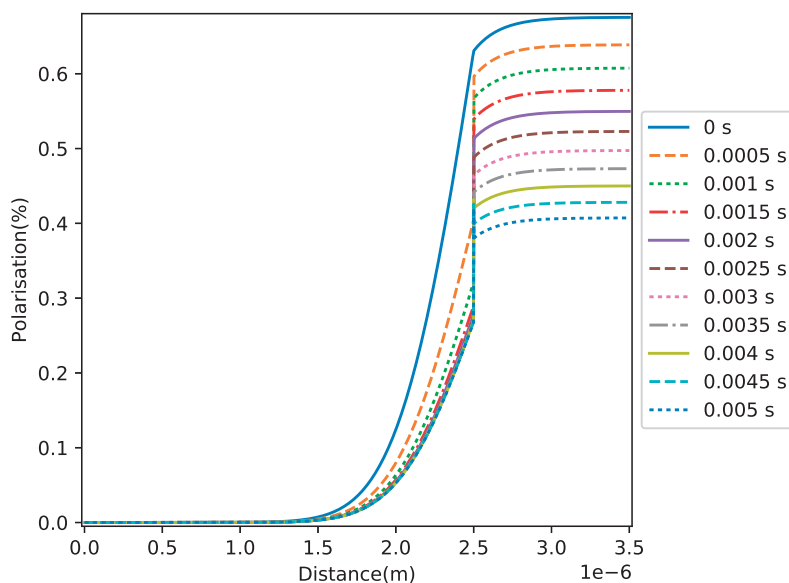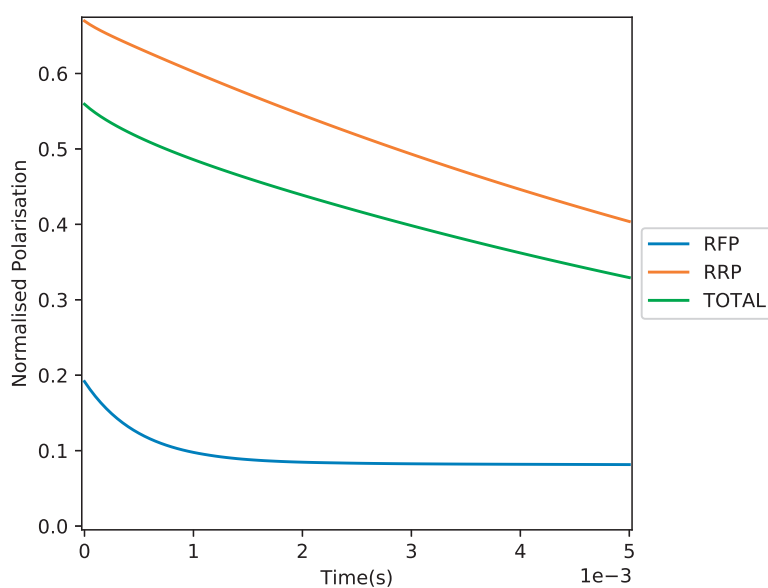

(d) Time-dependence of carbon-13 polarisation in a biphasic model.

Figure 2.10 – Simulated time-dependence of carbon-13 and of proton polarisation during a single CP block. Fig (a): Spatial distribution of the ^{13}C polarisation at different moments. Fig (b): Evolution of the ^{13}C polarisation as a function of the duration of spin-locking. Fig (c): Spatial distribution of ^1H polarisation at different moments. Fig (d): Evolution of ^1H polarisation as a function of the duration of spin-locking. The RFP is an equivalent spin glass of sodium pyruvate. The radius of the RFP core is constant as 2.5 µm and the thickness of the RRP layer is 1 µm in all simulations. Both phases are fully protonated.
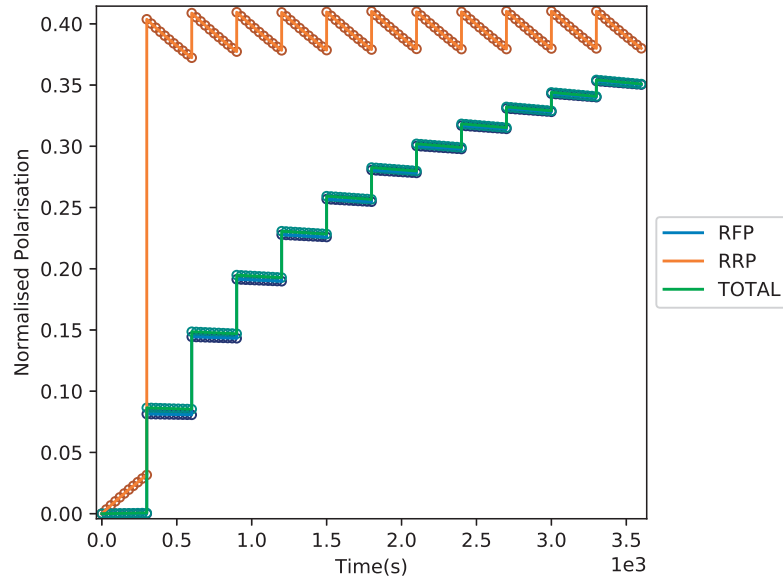
(a) Evolution of the carbon-13 polarisation during a multiple contact CP-DNP experiment.
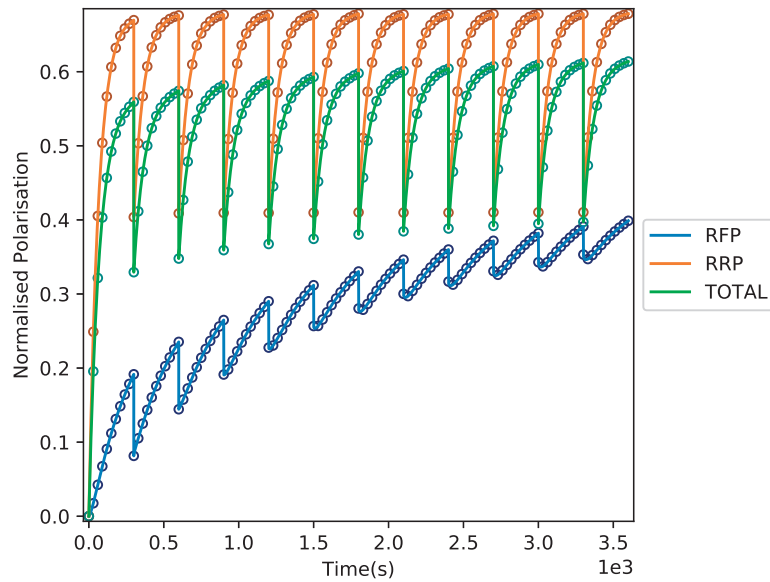
(b) Evolution of the proton polarisation during a multiple contact CP-DNP experiment.

Figure 2.11 – Simulated CP-DNP build-up curves for an interval of 300 seconds between two consecutive CP blocks. The RFP is an equivalent spin glass of sodium pyruvate. The radius of the RFP particle is 2.5 µm and the thickness of RRP layer is 1 µm all simulations. Both phases are fully protonated.
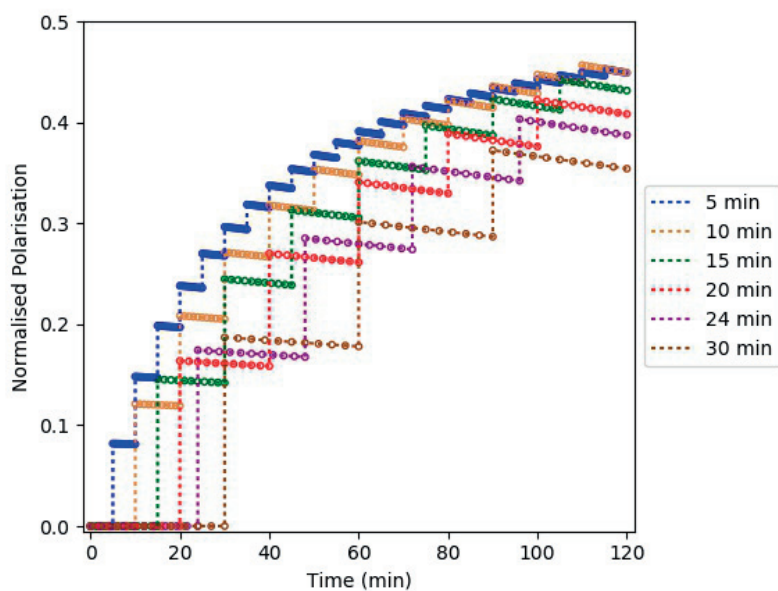
(a) Simulated build-up curves of the carbon-13 polarisation of two-hour-long multiple-contact CP-DNP process for different intervals between consecutive CP contacts.
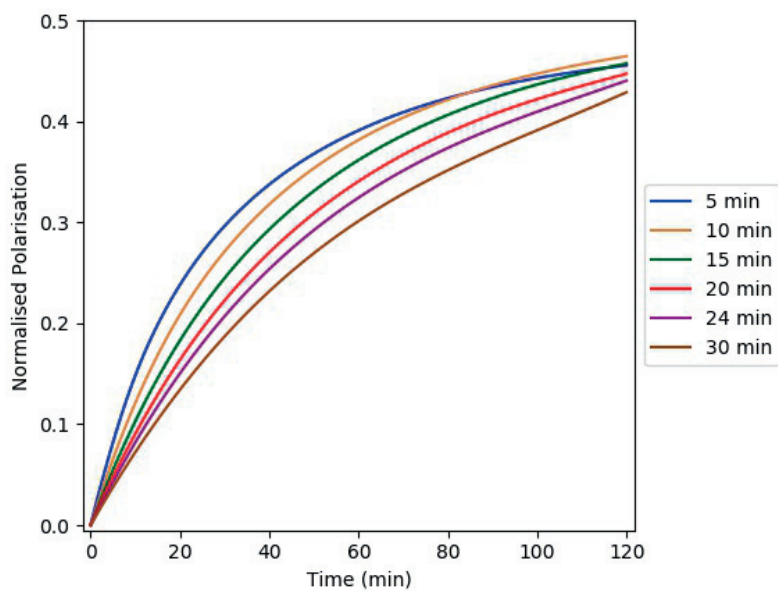
(b) Envelope of simulated build-up curves of the carbon-13 polarisation of two-hour-long multiple-contact CP-DNP process for different intervals between consecutive CP contacts.
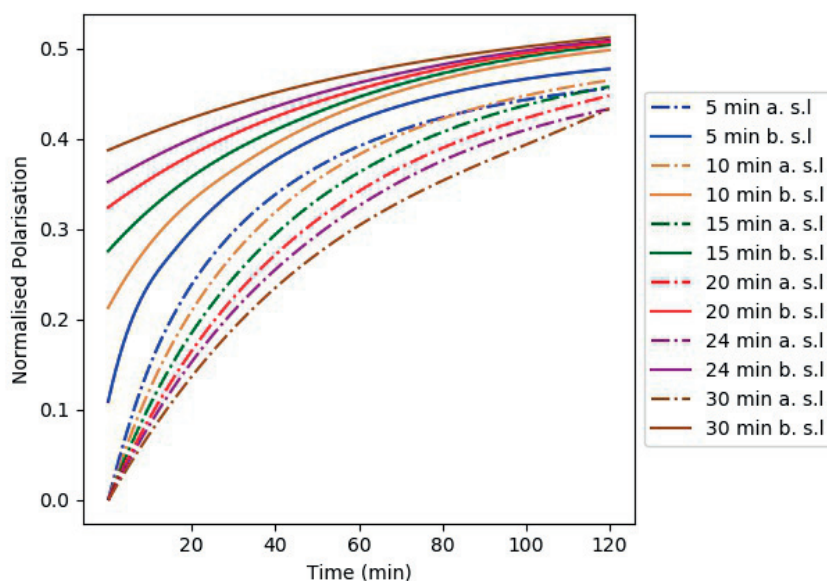
(c) Envelope of simulated build-up curves of the proton polarisation of two-hour-long multiple-contact CP-DNP process for different intervals between consecutive CP contacts.

Figure 2.12 – Simulated build-up curves of two-hour-long multiple-contact CP-DNP process for different intervals between consecutive CP contacts. Fig (a): Time-dependence of carbon-13 polarisation in the RFP. Fig(b):Envelopes of the carbon-13 build-up curves, showing the carbon-13 polarisation at the end of each CP contact. Fig (c): Envelopes of the proton build-up curves. The solid lines refer to the proton polarisation just before spin-locking (b. s.l.). The dashed-dotted lines indicate the envelope of the proton polarisation immediately after spin-lockings (a. s.l.). The RFP is an equivalent spin glass of sodium pyruvate. The radius of the RFP core is 2.5 μm and the thickness of the RRP layer is 1 μm in all simulations. Both phases are fully protonated.
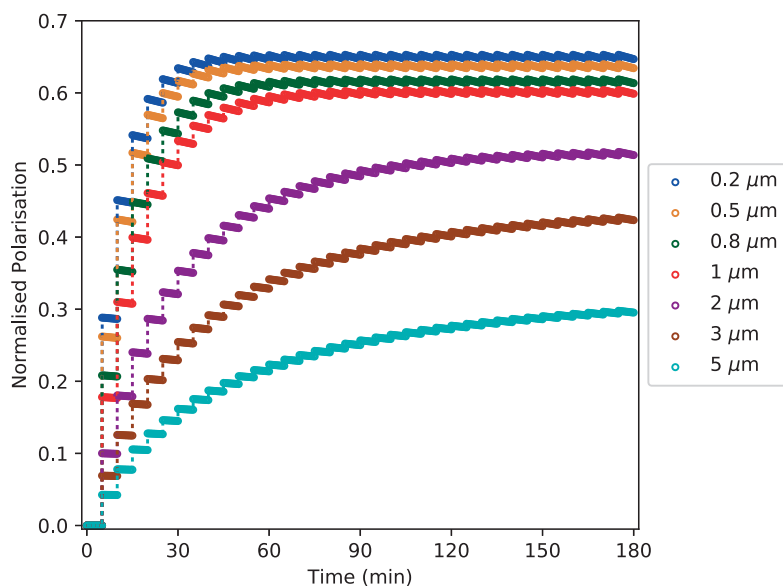
(a) Simulated build-up curves of the carbon-13 polarisation for different diameters of RFP particles.
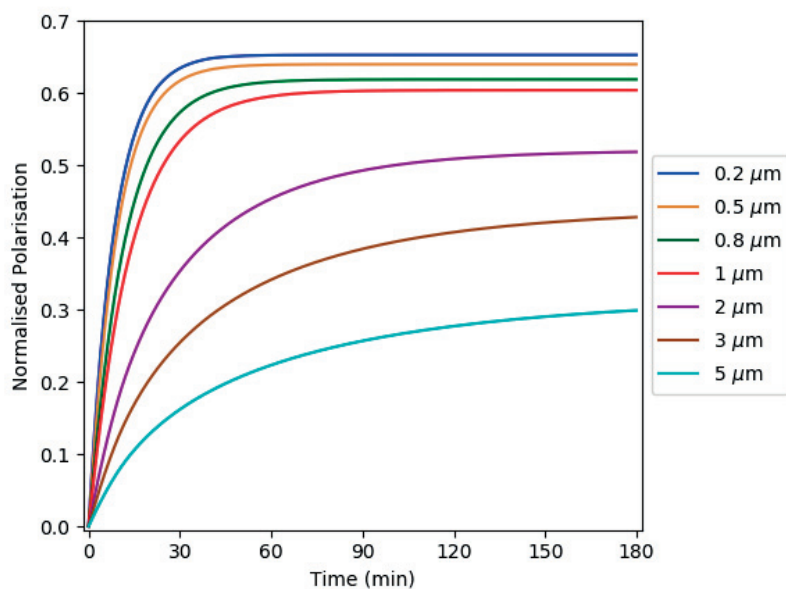
(b) Envelop of the simulated build-up curves of the carbon-13 polarisation for different diameters of RFP particles.
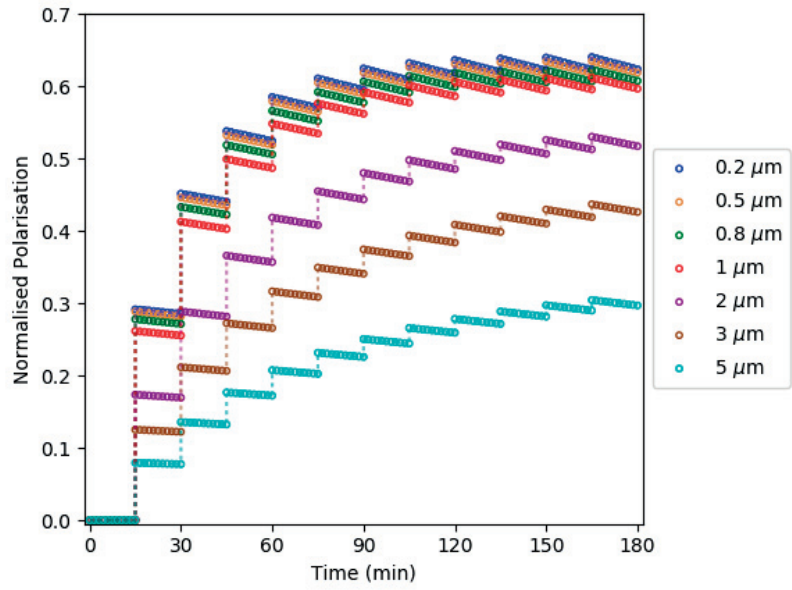
(c) Simulated build-up curves of the carbon-13 polarisation for different diameters of RFP particles.
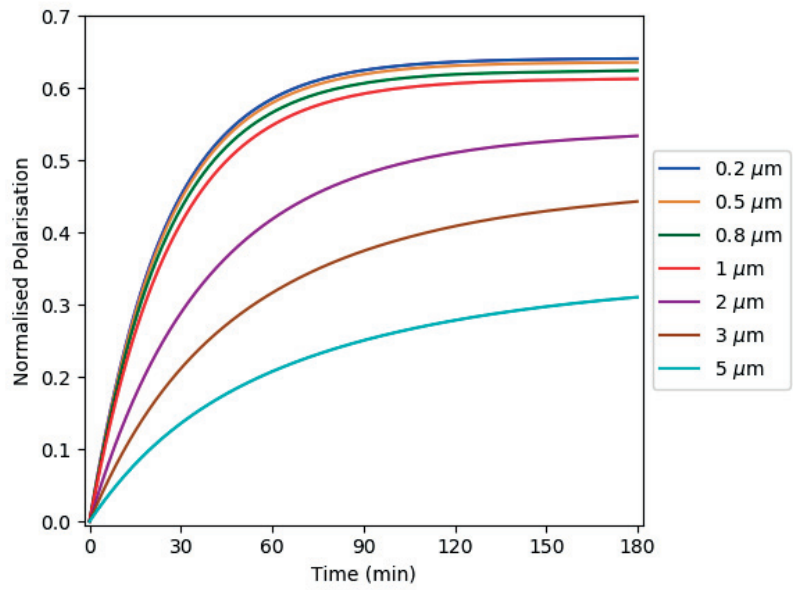
(d) Envelop of the simulated build-up curves of the carbon-13 polarisation for different diameters of RFP particles.
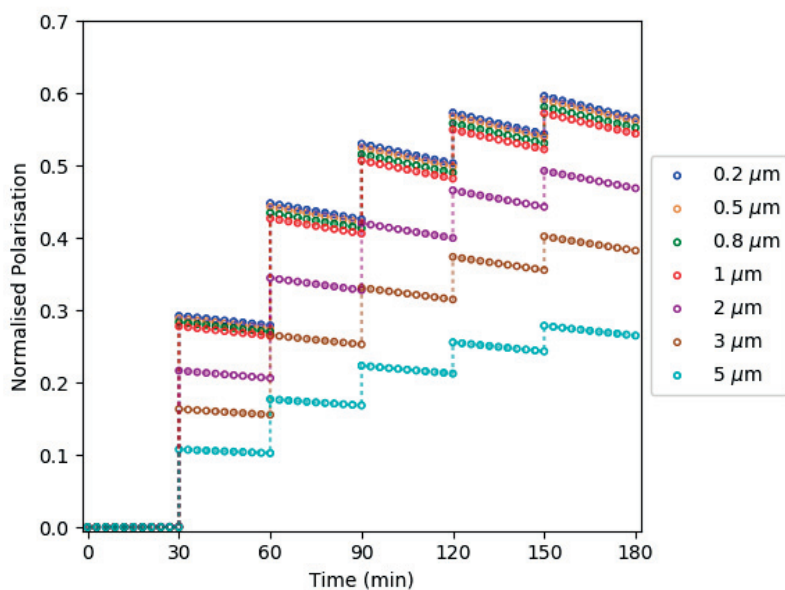
(e) Simulated build-up curves of the carbon-13 polarisation for different diameters of RFP particles.
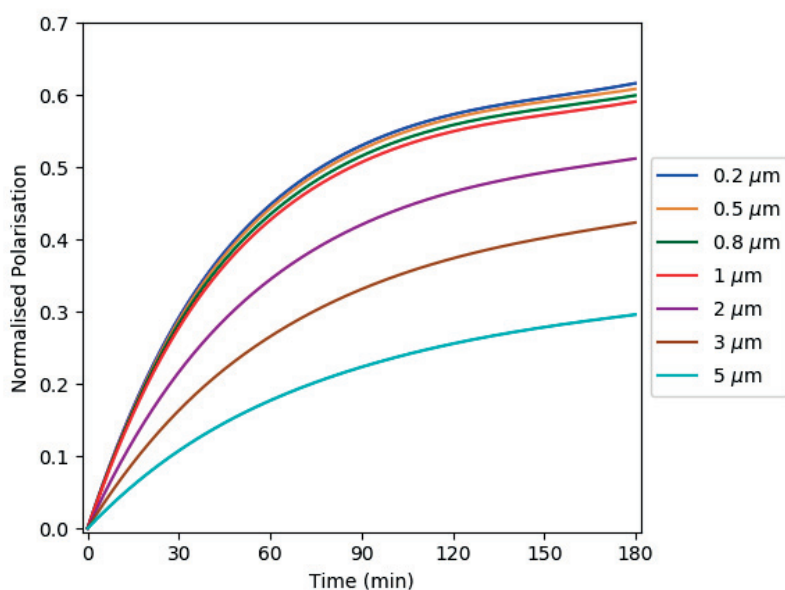
(f) Envelop of the simulated build-up curves of the carbon-13 polarisation for different diameters of RFP particles.

Figure 2.13 – Simulated time-dependence of carbon-13 polarisation in the RFP during multiple-contact CP-DNP processes with different intervals between consecutive CP contacts and different radii of the RFP particles. In figure (a) and (b), the CP interval is 300 s, in figure (c) and (d), the CP interval is 900 s, and in figure (e) and (f), the CP interval is 1800 s. The RFP is an equivalent spin glass of sodium pyruvate. The radius of RFP core is 2.5 µm and the thickness of RRP layer is 1 µm in all simulations. Both phases are fully protonated.

2.5.3   Relaxation in hyperpolarised biphasic samples

The last topic in this section will be the relaxation of the hyperpolarisation on long time-scales.

The simulation we conduct here follows the CP-DNP build-up in the previous subsection: we take the last points in the time domain of fig. 2.13 as the initial condition, then calculate the evolution of the polarisation, both proton and carbon-13 nuclei, during an interval of 10 hours for relaxaiton. The results are plotted in fig. 2.14 and fig. 2.15.

The main loss of proton polarisation in the RFP in our scenario is due to the spin diffusion driven by the spatial inhomogeneity of the polarisation. This spatial inhomogeneity pushes the nuclear magnetic energy carried by the proton spins from the RFP to the RRP. Once the magnetic energy arrives at RRP, it is rapidly consumed by fast paramagnetic relaxation in RRP.

When the equivalent spherical diameter of particle is less than 2 μm, the relaxation rates in the RFP and in the RRP are similar. The spatial segregation of the two phases does not play a significant role in slowing down nuclear relaxation. For bigger particles, whose spherical-equivalent radius is more than 5 micrometres, the polarisation may enjoy a prolonged lifetime. The gradient of the polarisation drives the flow of magnetic energy in both ways: both inward towards the core of the RFP particles, which had been less polarised; and outward to the RRP that had been rapidly relaxed due to paramagnetic PAs. Even in the most favourable cases, the proton hyperpolarisation vanishes within 3 hours.

As we can expect, the carbon-13 polarisation in the RRP decays to zero in 1 hour. On the other hand, the carbon-13 polarisation in the RFP survives much longer, and decays with the same long time constant regardless of the difference in particle size.

A closer look at the spatial distribution of carbon-13 polarisation gives us more details. As suggested by fig. 2.15b, fig. 2.15d, and fig. 2.15f, after complete relaxation of carbon-13 hyperpolarisation in RRP, there exists an important gradient of carbon-13 polarisation at the interface between the RRP and the RFP. In contrast to the proton paths, the outward flow of carbon-13 magnetic energy through carbon-13 spin diffusion from the RFP to the RRP is not efficient. Furthermore, from fig. 2.15a, fig. 2.15c, and fig. 2.15e we can observe a tendency that, in large crystallites, the enriched carbon-13 polarisation migrates towards the centre of particle rather the opposite. This can be easily explained with the huge contrast of ^{13}C concentration in two phases, and consequently the contrast of spin diffusivity of carbon-13 in either phase. Although there exists a huge gradient of carbon polarisation at the interface, the miserable spin conductivity in the RRP does not permit a high total flow of magnetic energy. Therefore the relaxation of carbon 13 spins at low temperature only depends on the inherent properties of auto-relaxation. Biphasic spin diffusion does not have a

leading role.

(a) Spatial distribution of proton hyperpolarisation during relaxation.
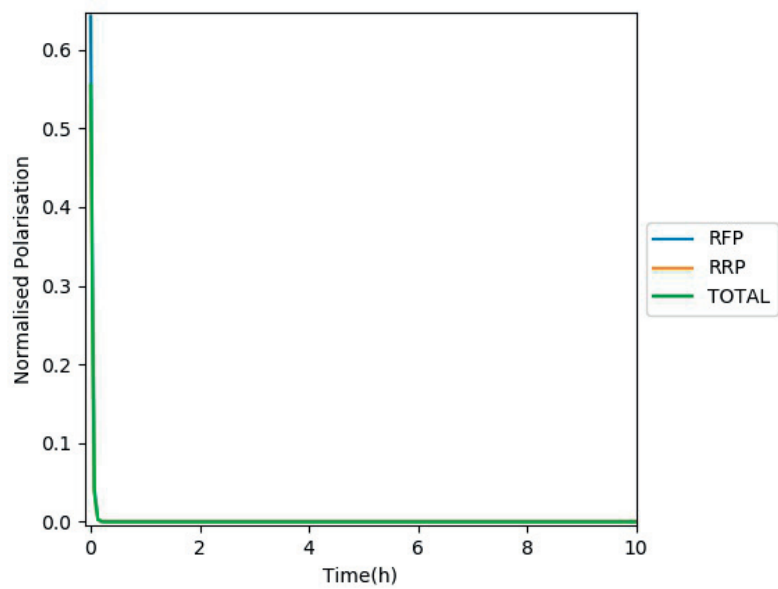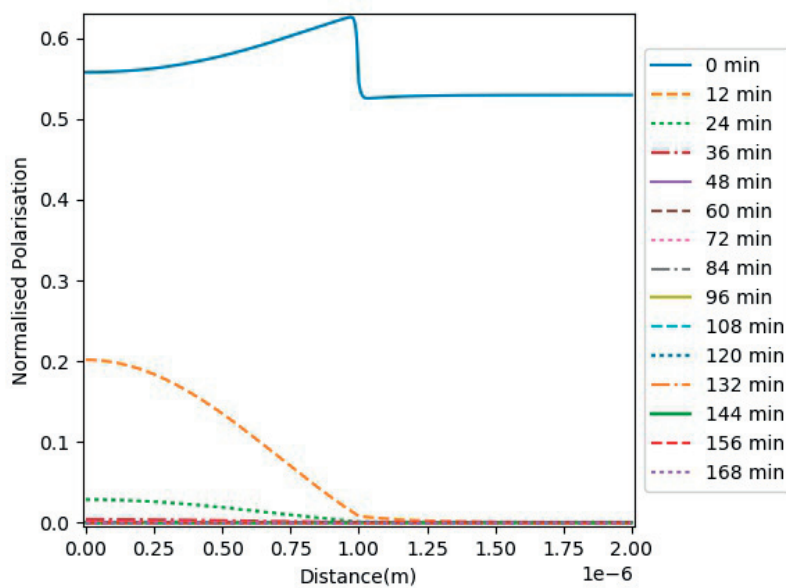
(b) Relaxation of the proton polarisation.

(c) Spatial distribution of proton hyperpolarisation during relaxation.
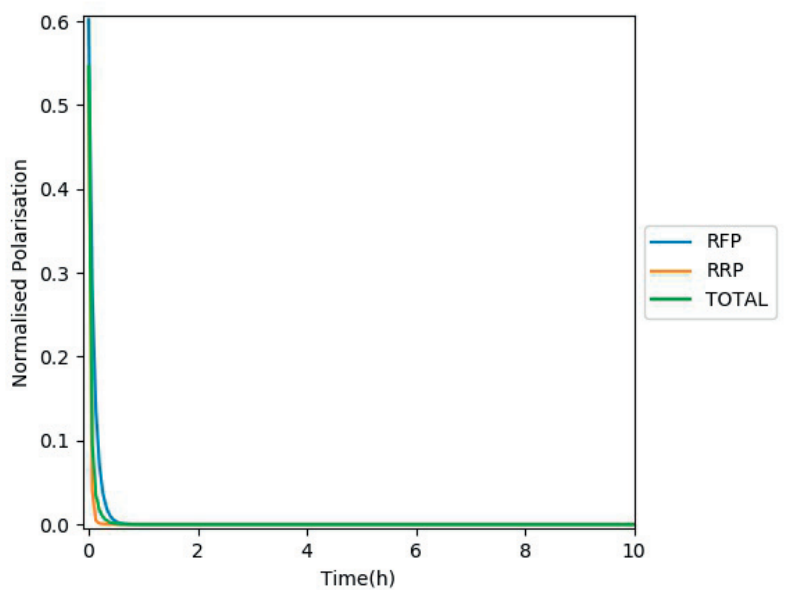
(d) Relaxation of the proton polarisation.

(e) Spatial distribution of proton hyperpolarisation during relaxation.
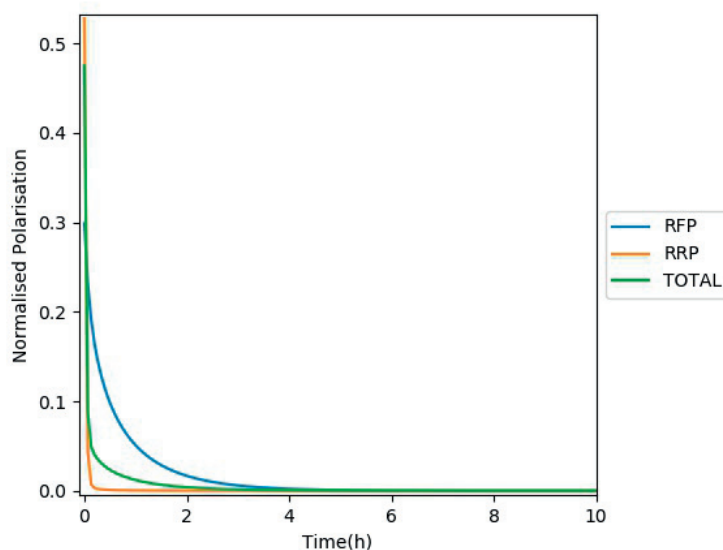
(f) Relaxation of the proton polarisation.

Figure 2.14 – Simulated time-dependent relaxation of the proton hyperpolarisation during the diffusion relayed DNP. The RFP is an equivalent spin glass of sodium pyruvate, where the proton spin density is 33 mol·L^{-1}. The RRP is a spin glass of natural abundance at 110 mol·L^{-1}. In figure (a) and (b), the effective Wigner–Seitz radius is 0.2 μm for the RFP and the effective thickness of the RP layer is 1 μm. In figure (c) and (d), the effective Wigner–Seitz radius is 2 μm for the RFP and the effective thickness of the RP layer is 1 μm. In figure (e) and (f) he effective Wigner–Seitz radius is 5 μm for the RFP and the effective thickness of the RP layer is 1 μm.

(a) Spatial distribution of carbon-13 hyperpolarisation during relaxation.
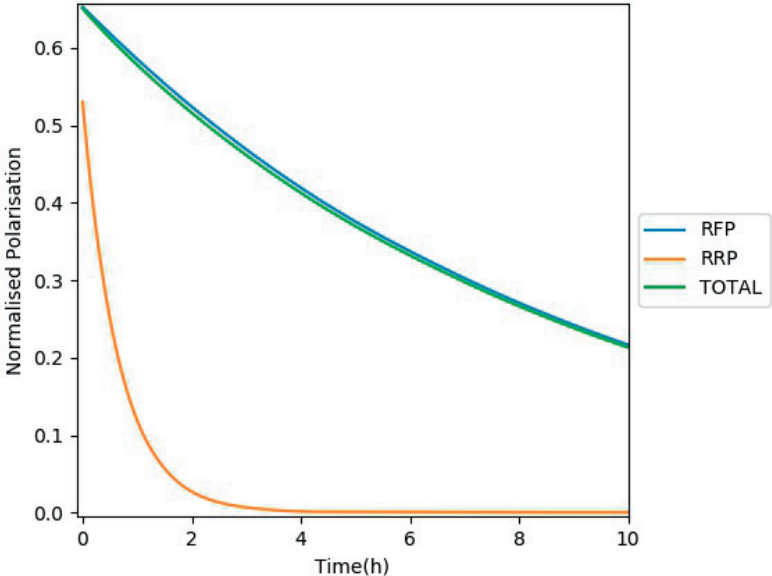
(b) Relaxation of the carbon-13 polarisation.
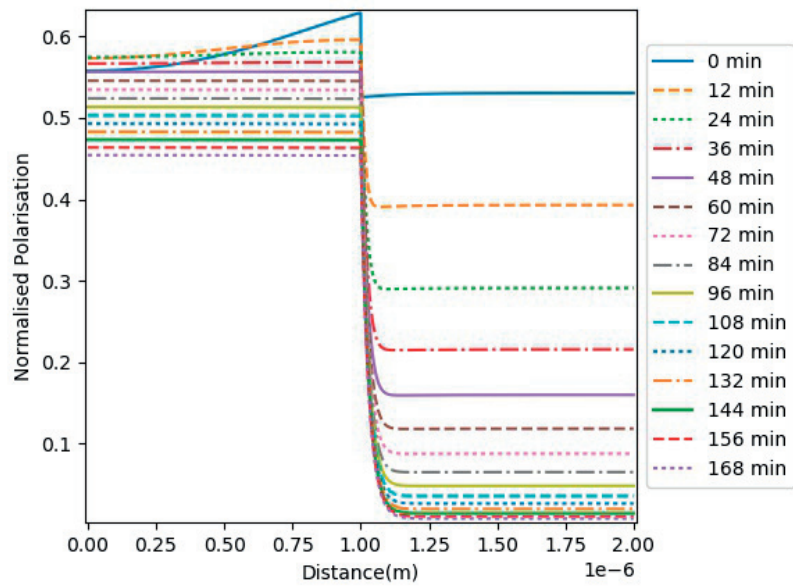
(c) Spatial distribution of carbon-13 hyperpolarisation during relaxation.

(d) Relaxation of the carbon-13 polarisation.

(e) Spatial distribution of carbon-13 hyperpolarisation during relaxation.

(f) Relaxation of the carbon-13 polarisation.

Figure 2.15 – Simulated time-dependent relaxation of the carbon-13 hyperpolarisation during the diffusion relayed DNP. The RFP is an equivalent spin glass of sodium pyruvate, where the proton spin density is $11\ mol \cdot L^{-1}$. The RRP is a spin glass of natural abundance at $0.69\ mol \cdot L^{-1}$. In figure (a) and (b), the effective Wigner–Seitz radius is $0.2\ \mu m$ for the RFP and the effective thickness of the RP layer is $1\ \mu m$. In figure (c) and (d), the effective Wigner–Seitz radius is $2\ \mu m$ for the RFP and the effective thickness of the RP layer is $1\ \mu m$. In figure (e) and (f) he effective Wigner–Seitz radius is $5\ \mu m$ for the RFP and the effective thickness of the RP layer is $1\ \mu m$.

3 Microwave-Gated Dynamic Nuclear Polarisation

The success of a d-DNP experiments depend on the achievement of hyperpolarisation at low temperatures. Initially , the low-γ nuclei are polarised by direct thermal contact between ^{13}C spin reservoir and the electronic spin reservoir.

Recently, Jannin *et al.* reported a success in coupling the DNP with CP. With this CP-DNP approach, we can first polarise the protons in the system directly, and then equalise the spin temperatures of the proton and carbon-13 reservoirs in the system.

Based on this CP-DNP scheme, Bornet *et al.* [92] further proposed a modified scheme for CP-DNP, in view of optimising CP. The key of this new method is to place a gating gap in the microwave irradiation before launching the CP spin-locking sequence. Such gating gaps allow the electronic spins to relax from their partially saturated state to their thermal equilibrium, where they are almost 100% polarised. A high electronic polarisation prior to the CP contact leads to a reduced paramagnetic nuclear relaxation, and thus to extended nuclear longitudinal relaxation times in the rotating frame for both protons and carbons. Therefore the efficiency of the CP-DNP build-up can be improved.

In this chapter, we shall apply the same principles of simulation that we used in chapter 2 in the context of microwave-gated DNP in homogeneous spin glasses.

3.1 Simulations of the Microwave-Gated DNP

3.1.1 Paramagnetic relaxation under DNP conditions

At low temperature and high field, the nuclear spin N at a distance r from electron spin $E = 1/2$ relaxes at the rate constant as a function of time, which could be obtained from the Solomon-Bloembergen equations[93, 94]:

$$R_{1,\rho}(t) = \frac{1}{T_{1,\rho}(t)} \tag{3.1}$$

$$= \frac{C}{r^6} \cdot \frac{\tau_c \cdot \left[1 - P_e^{Eq} \cdot P_e(t)\right]}{1 + \omega_n^2 \cdot \tau_c^2 \cdot \left[1 - P_e^{Eq} \cdot P_e(t)\right]^2} \tag{3.2}$$

where $P_e(t)$ is the electron spin polarisation at time t, P_e^{Eq} is electron spin polarisation in thermal equilibrium, τ_c is the correlation time the fluctuating electron dipolar field at the site of the nuclear spin, and C is a constant.

Now we consider two times, t_{eq} and t, where the system is at thermal equilibrium at t_{eq}, namely $P_e(t_{eq}) = P_e^{Eq}$, while at time t the system is partially saturated by continuous microwave irradiation. We define the ξ as the ratio between $R_{1,\rho}(t)$ and $R_{1,\rho}(t_{eq})$:

$$\xi = \frac{R_{1,\rho}(t)}{R_{1,\rho}(t_{eq})} = \frac{T_{1,\rho}(t_{eq})}{T_{1,\rho}(t)}$$

$$= \frac{\left[1 - P_e^{Eq} \cdot P_e(t)\right]}{\left\{1 + \omega_n^2 \cdot \tau_c^2 \cdot \left[1 - P_e^{Eq} \cdot P_e(t)\right]^2\right\}} \cdot \left\{1 + \omega_n^2 \cdot \tau_c^2 \cdot \left[1 - P_e^{Eq} \cdot P_e(t_{eq})\right]^2\right\}\left[1 - P_e^{Eq} \cdot P_e(t_{eq})\right] \tag{3.3}$$

$$= \frac{\left[1 - P_e^{Eq} \cdot P_e(t)\right] \cdot \left\{1 + \omega_n^2 \cdot \tau_c^2 \cdot \left[1 - P_e^{Eq} \cdot P_e(t_{eq})\right]^2\right\}}{\left\{1 + \omega_n^2 \cdot \tau_c^2 \cdot \left[1 - P_e^{Eq} \cdot P_e(t)\right]^2\right\} \cdot \left[1 - P_e^{Eq} \cdot P_e(t_{eq})\right]} \tag{3.4}$$

At 1.2 K and 6.7 T, we have the typical values as $P_e^{Eq} = 0.996$ and $\omega_H = 1.79 \cdot 10^9$ rad·s^{-1} $\omega_C = 4.56 \cdot 10^8$ rad·s^{-1}, so that we can plot the ratio between ξ_H and ξ_C as functions of both $P_e(t)$ and τ_c:

As illustrated in fig. 3.1, under the condition that the correlation time of the fluctuating electron dipolar field at the site of the nuclear spin be on the sub-nanosecond scale, the contribution of paramagnetic relaxation in the total rate of nuclear relaxation in rotating frame would be amplified when the microwave irradiation is constantly applied during the spin-locking process. When the nuclear spins are correlated with a motion, whose time-scale is on the order of $10^{-8}s$, the technique of microwave gating would not be very efficient. On the other hand, if the system were mainly subject to slow motions that have characteristic times beyond $10^{-8}s$, we could even reduce the loss of paramagnetic relaxation by saturating ESR absorptions.
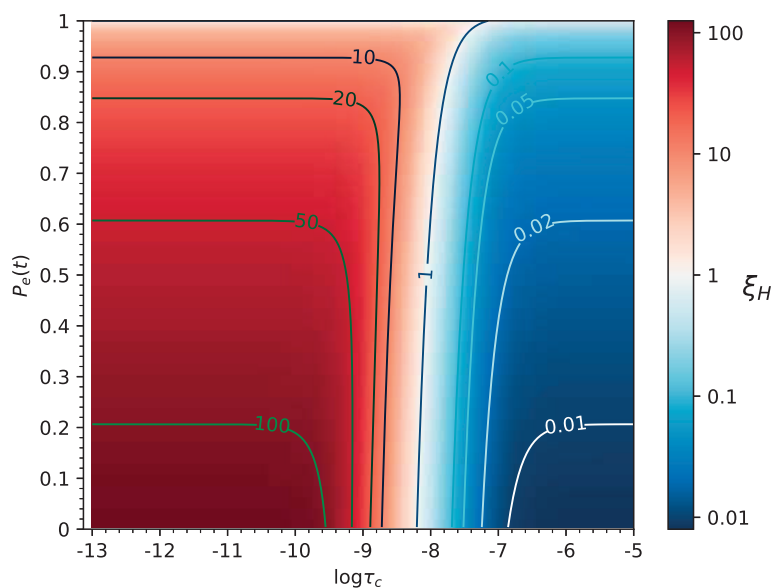
(g) ξ_H as a function of $P_e(t)$ and $\log \tau_c$ at 1.2 K, 6.7 T.
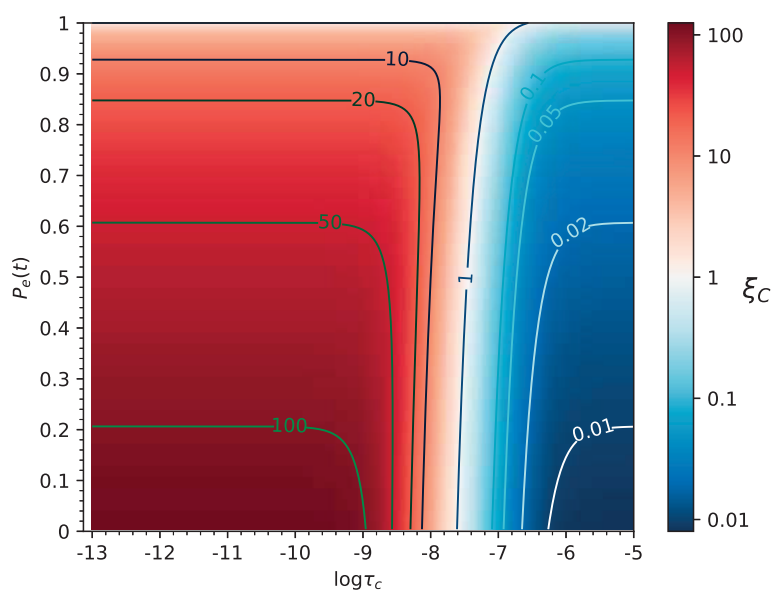
(h) ξ_C as a function of $P_e(t)$ and $\log \tau_c$ at 1.2 K, 6.7 T .

Figure 3.0 – The simulation of the ξ_H and ξ_C as a function of $P_e(t)$ and $\log \tau_c$ at 1.2 K, 6.7 T. In the red region, the paramagnetic relaxation is stronger when the electron spins are partially saturated, while in the blue region, the paramagnetic relaxation is stronger at thermal equilibrium.

3.1.2   Mathematical formulation of the build-up process

The dynamics of direct diffusion-relayed DNP

Since we are treating the samples with only one phase, the complexity of the problem reduces drastically from a second-order parabolic partiall differential equaiton (PDE) into an first-order ordinary differential equation (ODE) of time.

The governing equation then writes:

$$\begin{cases} \boldsymbol{d_a} \circ \frac{\partial}{\partial t} \boldsymbol{P}(t) = \boldsymbol{Q}(t) \\ \boldsymbol{d_a} = \boldsymbol{C_p} \circ \boldsymbol{c} \end{cases} \tag{3.5a}$$

$$\boldsymbol{P}(t = 0) = 0 \tag{3.5b}$$

For the diffusion-assisted DNP blocks that follows a CP block, the initial value should be the result of CP block.

The dynamics under CP

We use the same methodology to describe the dynamics within the CP blocks as in eq. (2.17) and in eq. (2.18). Details can be found in section 2.3.2.

3.1.3   Choice of parameters for simulations

For the simulation of CP profiles in this section, we limit ourselves to the experimental data reported in the original paper by A. Bornet [92]:

Sample composition

We only consider one DNP sample in this chapter: a frozen solution of 3 mol·L^{-1} [$1-^{13}C$]acetate in H_2O:D_2O:glycerol-d_8 ($v:v:v = 1:4:5$) doped with 40 mmol·L^{-1} TEMPOL at 1.2 K and 6.7 T.

Spin density

The protonspin density of proton in the mixed solvent of H_2O, D_2O, and glycerol-d_8 is approximately 11.1 mol·L^{-1}. We consider the total spin density of the frozen solution to be 20 mol·L^{-1}. A similar calculation can also be applied to assess the spin density of carbon-13 in the mixed solvent at natural abundance, which gives 0.225 mol·L^{-1}. We thus have 3.225 mol·L^{-1} as the total spin density of carbon in the frozen glassy solution, from the solvent and the carbon-enriched solute together.

Build-up time

The time constants of the build-up process are determined by a mono-exponential fit of the experimental data. The actual value used in simulations was set to be 150 s for protons and 6000 s for carbon-13.

Longitudinal Relaxation Time in the Rotating Frame (R)

Let us assume that these two factors share the same value during CP contact for a qualitative overview.

In the second step, we try to fit the experimental data. Because once the spin temperature of two nuclear spin reservoirs equalises, the relaxation in the rotating frame is dominated by the faster one of the two. In the cases where we apply continuous microwave irradiation, the $T_{1,\rho}^H$ is measured to be 10 ms while $T_{1,\rho}^C$ equals 7.4 ms from the fitting of experimental data. In the microwave-gated case, both time constants are assumed to be 100 ms.

Maximum Polarisation

The maximum polarisation can be fitted to experimental build-up curves. In the sample of 3 mol·L^{-1} [1 $-^{13}C$]acetate in H_2O:D_2O:glycerol-d_8 ($v:v:v = 1:4:5$) doped with 40 mmol·L^{-1} TEMPOL., we have a proton polarisation of 70%. According to the theory of thermal mixing, at the steady state of the DNP process, all species of nuclear spins arrive at a common spin temperature, so we can determine the carbon-13 polarisation to be 0.21%.

Average Dipolar Coupling

The average dipolar coupling is used to describe the rate of transfer of nuclear magnetic energy between distinct nuclear spin reservoirs during the process of cross polarisation. This parameter here is fitted to the experimental data of the dynamics of CP contact: as presented in the supporting information of Bornet's paper[92], $b_{H-C} = 1000/2.68 = 373$ Hz.

3.2 Numerical result of simulation

The first simulations that we present show the efficiency of CP for different values of $T_{1\rho}$. As shown in fig. 3.1, when the $T_{1,\rho}$ is short, the fast relaxation imposes a strong penalty on the build-up of carbon-13 polarisation during the thermal contact of CP. As a compromise, we will have to choose short spin-lock duration for each CP block.

On the contrary, under conditions of microwave gating, we can benefit from a much longer CP-contact time, in view of more efficient thermal mixing between the reservoirs of protons and of carbon-13.

The fig. 3.1 demonstrates how the $T_{1,\rho}$ influences the evolution of polarisation in the manifolds of different nuclear spins during the first CP block.

With a similar method, we can then describe the evolution of the polarisation during all the CP blocks within a multiple-CP-DNP sequence (See fig. 3.3). As the initial condition changes with the accumulation of carbon polarisation in previous CP blocks, the optimal duration of spin lock is reduced accordingly, until a dynamic equilibrium between the replenishment of the proton polarisation and the relaxation of carbon-13 polarisation finally occurs.

Basing on the optimal condition obtained from fig. 3.3, we can perform simulations in view of optimized build-up profiles of CP-DNP processes.

3.3   Discussion

Combining the correlations shown in fig. 3.1 and in fig. 3.1, we might conclude that, in order to benefit from a long and efficient CP blocks, the best timing for launching the spin-lock would be after the complete relaxation of the electronic spins, long after cutting off the microwaves. Admittedly, when the microwave irradiation is turned off, nuclear spins start to relax to their thermal equilibriums as well. This factor is, however, less significant. This is because, compared to the nuclear relaxation, the time-scale for the electronic spins to relax to their thermal equilibrium is negligible.
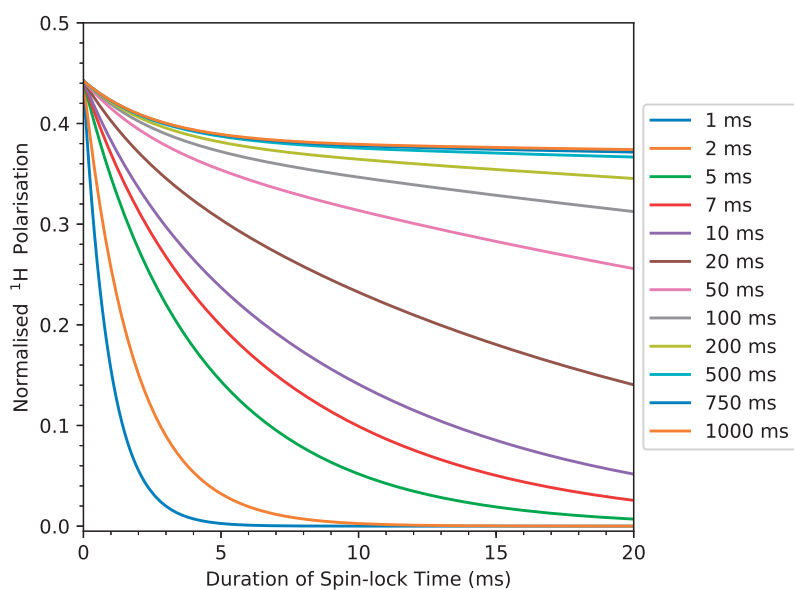
(a) The simulated polarisation of protons as a function of the CP contact time for different $T_{1,\rho}$.
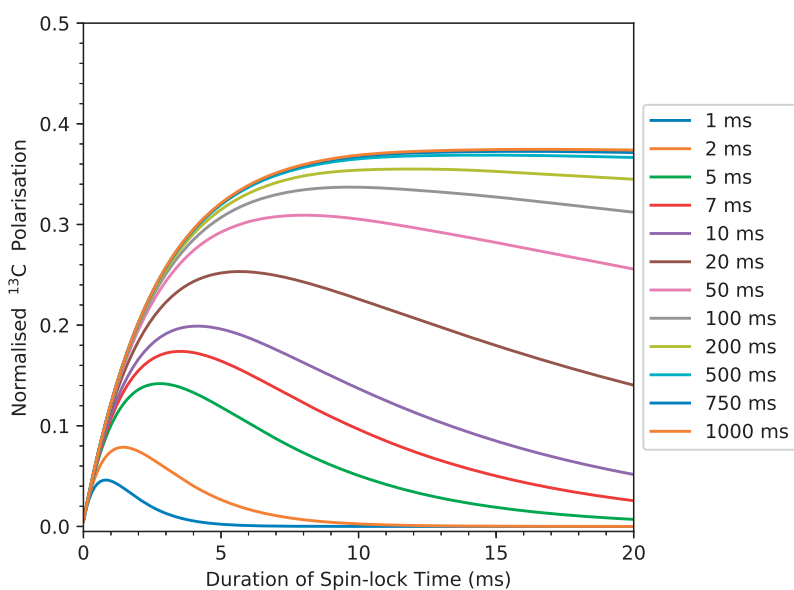
(b) The simulated polarisation of carbon-13 as a function of the CP contact time for different $T_{1,\rho}$.

Figure 3.1 – The simulated nuclear polarisation as a function of spin-lock time for different $T_{1,\rho}$. In both simulated subfigures, the $T_{1,\rho}^H$ is set to be equal to $T_{1,\rho}^C$. Detailed parameters of these simulations can be found in table A.3.
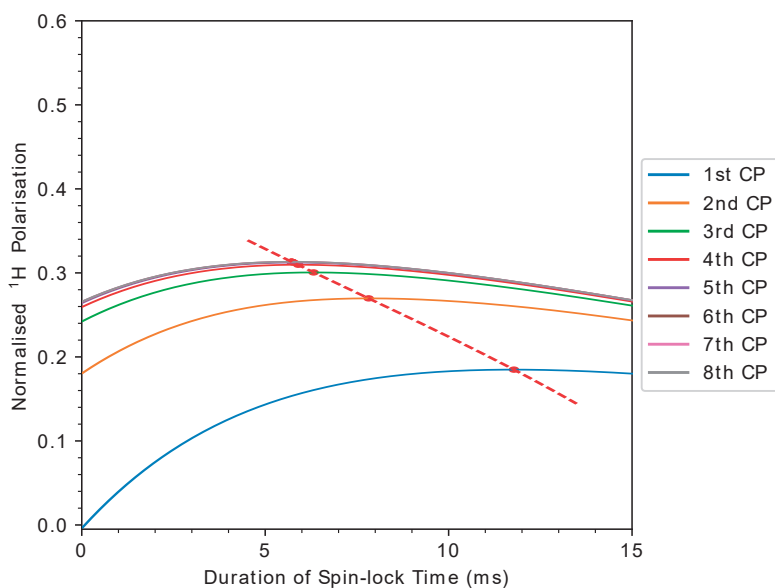
(a) The evolution of ^{13}C polarisation during CP blocks in a CP-DNP sequence without microwave-gating.
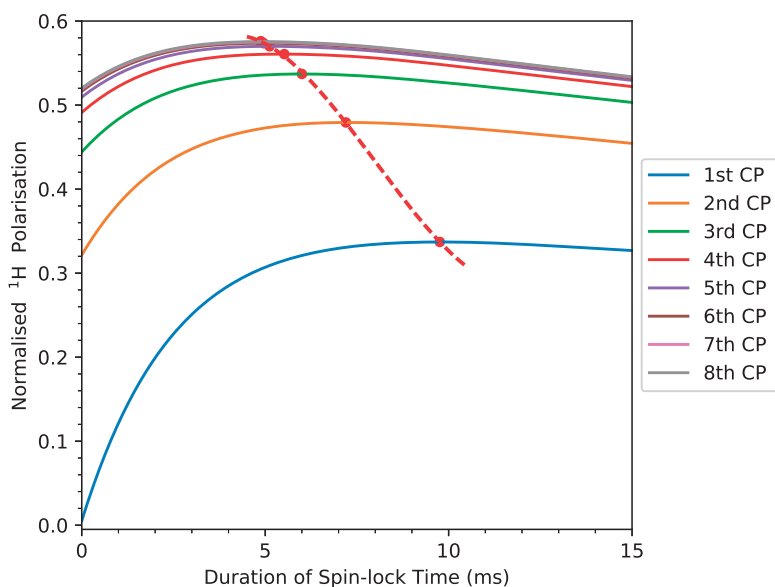
(b) The evolution of ^{13}C polarisation during CP blocks in a CP-DNP sequence with microwave-gating.

Figure 3.2 – The simulated evolution of ^{13}C polarisation during consecutive CP blocks in a CP-DNP sequence. Red dashed lines link the maxima of ^{13}C polarisation that we can obtain in each CP block. Detailed parameters of simulation can be found in table A.3.
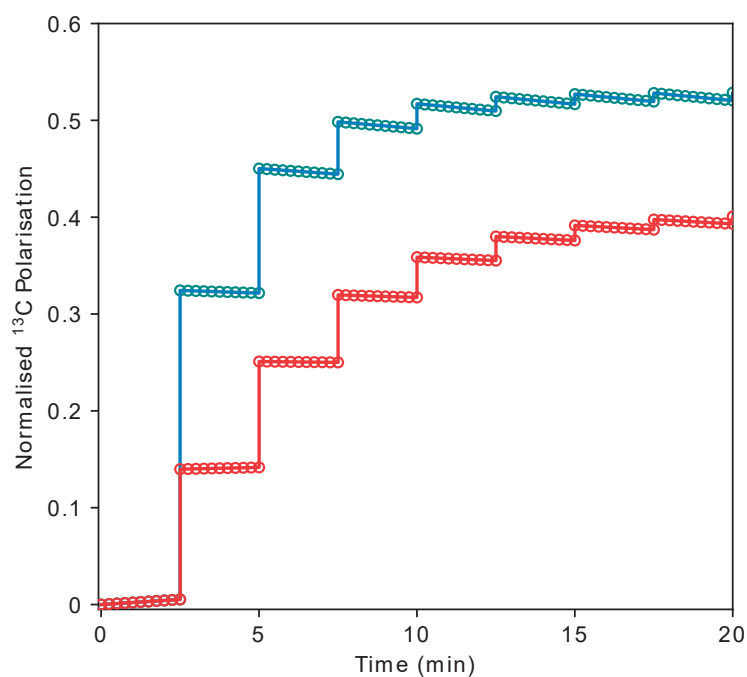
Figure 3.3 – The simulated build-up curves of carbon-13 polarisation during multiple CP-DNP in a frozen solution of 3 mol·L^{-1} [1 −^{13}C]acetate in H_2O:D_2O:glycerol-d_8 (v : v : v = 1 : 4 : 5) doped with 40 mmol·L^{-1} TEMPOL at 1.2 K and 6.7 T. The red curve is under the condition of continuous microwave irradiation, and the blue curve is under the condition of microwave gating. Detailed parameters of simulation can be found in table A.3.

4 Remote DNP with Impregnated Microcrystals

In this chapter, we shall present an illustrative example where we successfully illustrated the principle of transportable hyperpolarisation. With the help of a small electromagnetic solenoid to overcome the local dipolar field inside the sample, we can move the hyperpolarised crystals of $[U-^{13}C,^{15}N]$-labelled amino-acids out of the polariser. As long as the crystals are stored in a moderate field (*ca.* 1 T) in a liquid helium bath, their ^{13}C magnetisation can be observed after a dissolution experiment following a 16-hour-long storage.

4.1 Sample Preparation

Following the principle of biphasic sample formulation described in chapter 2, we divide our sample preparation step into two main steps:

- Preparing a micro-particulate radical-free phase (RFP)

- Formulating glassy radical-rich phase (RRP)

4.1.1 Preparing micro-particulate radical-free phase (RFP)

Our attempts thus start with grinding by hand [95] *. fig. 4.1a shows a picture of ground sodium pyruvate from scanning electron microscopy (SEM). From the statistics illustrated in fig. 4.1b, most of the particles have a surface-equivalent diameter around 1 μm, and the overall distribution of particle number manifest a long-tail pattern. It is worthy to note, however, that the distribution of particle volumes can be very different from the direct counting of particle numbers. As the volume of particle is proportional to the cube of diameter of the particles, and although the percentage of large crystallites is not significant after grinding, most of the molecules are nevertheless

---

*Detailed protocols can be found in the appendix

contained in a few large grains. The mean value of the distribution of the particle volume of sodium pyruvate powder after hand grinding is around 7 μm.
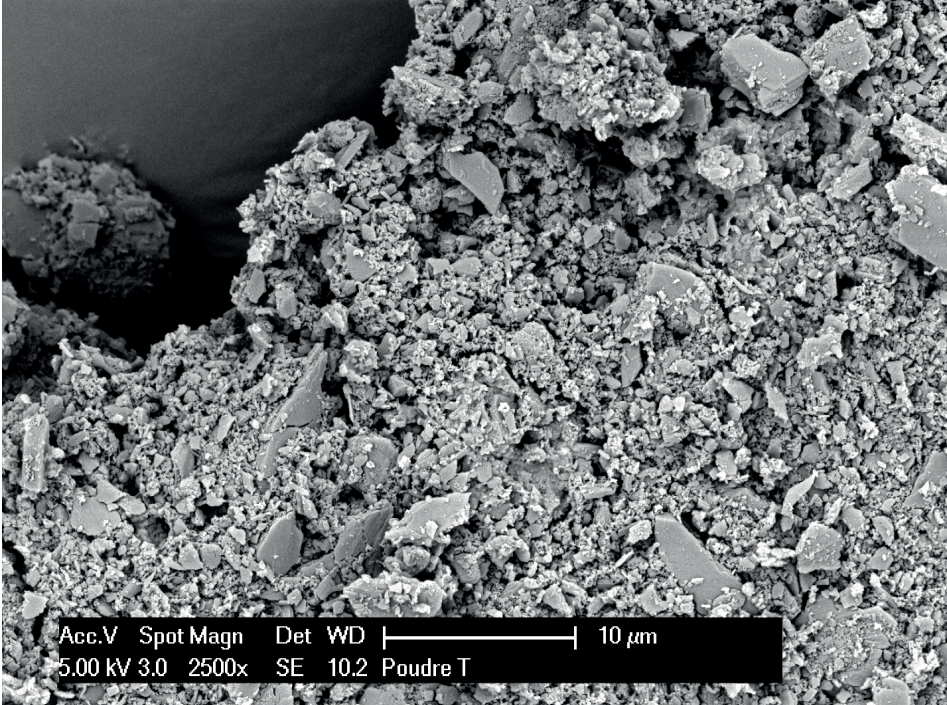
(a) SEM picture of sodium pyruvate after grinding.
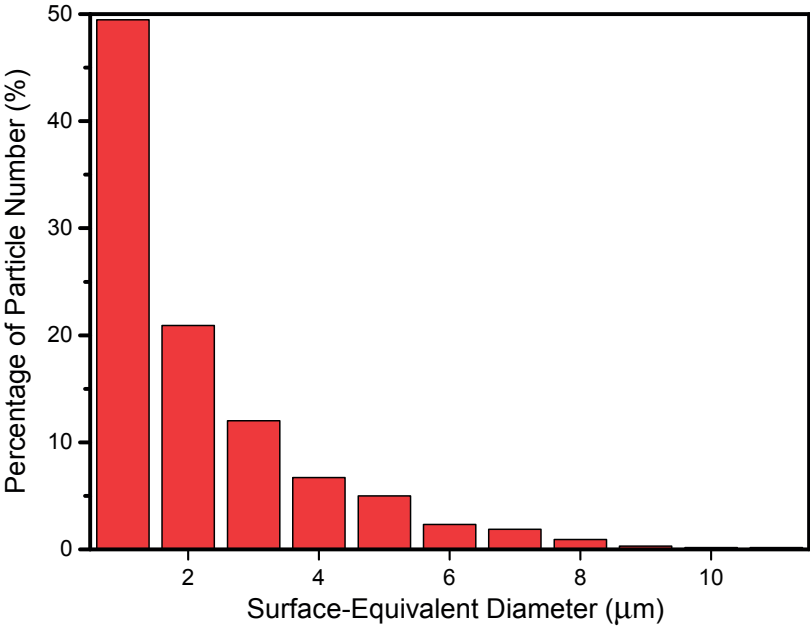
(b) Histogrtam of the distribution of the particle numbers in (a).
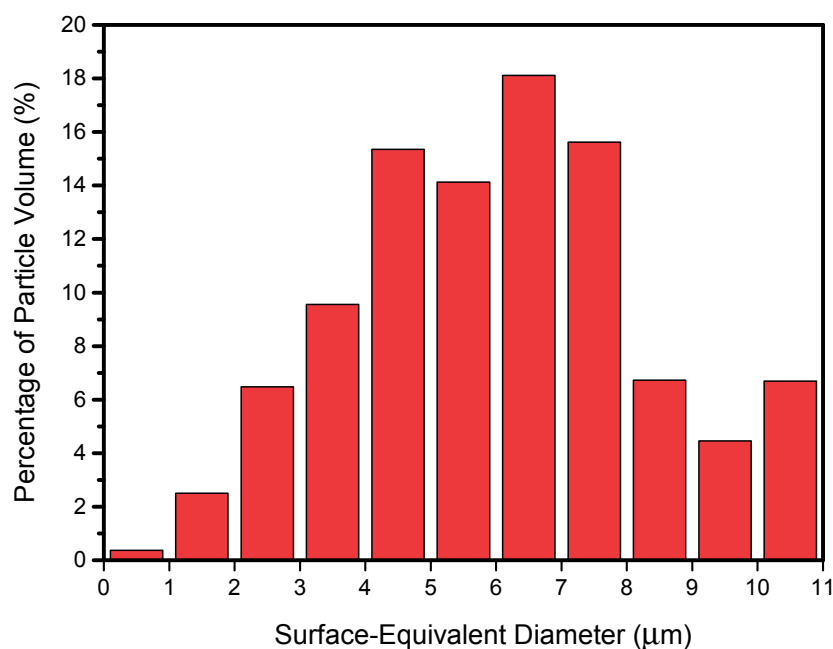
(c) Histogrtam of the distribution of the particle volume in (a).

Figure 4.1 – The profile of granularity of a sodium [1 −^{13}C]pyruvate sample after grinding. Figure (a) SEM picture of sodium [1 −^{13}C]pyruvate sample after grinding. Figure (b) Distribution of the surface-equivalent diameters of particles of sodium [1 −^{13}C]pyruvate in terms of the percentage of total particle numbers. Figure (c) shows the distribution of the volume-equivalent diameters of particles of sodium [1 −^{13}C]pyruvate in terms of the percentage of particle volume.

4.1.2   Formulating glassy radical-rich phase (RRP)

In contrast to conventional hydrophilic glassy RRPs, we are obliged to use solvents that have solubilities that are orthogonal with respect to biological metabolites to prepare biphasic samples.

Based on the solubility of TEMPO-benzoate, a hydrophobic derivative of TEMPO radical, we first chose a mixture of toluene and THF as the solvent. The role of THF (20% v/v) is to ensure the proper vitrification of the mixture, because THF is not glass-forming on its own and the glassy state of pure toluene is not stable compared with its crystalline form.

As studied in a previous chapter[†], we limit our scope here to the purely protonated spin glasses. In agreement with the results of numerical simulations, high proton concentrations favour proton spin diffusion[‡]. It would then facilitate the flow of

---

[†]see section 2.5.1

[‡]See fig. 2.9

magnetic energy towards the interface between RRP and RFP.

The choice of the level of doping with polarising agents is more complicated. In view of a satisfactory DNP performance, we require that the concentration of radicals to be in the optimal region. When the PA is too diluted, the protons are not sufficiently coupled to the electronic spins. We cannot achieve an efficient transfer of polarisation from radicals to nuclei. On the other hand, if we dope too high a concentration of radicals in the RRP, the dipolar couplings between electronic spins becomes too strong, so that they compete with the hyperfine couplings that polarises protons. We would also suffer from an enhanced paramagnetic nuclear relaxation in the RRP as the content of paramagnetic species in mixture increases. In the lack of convincing theoretical models, our intuition was confirmed on a trial-and-error basis. Basing on our previous experience with water-glycerol-based mixtures[96], our experimental attempts started from 50 mmol·L^{-1}, and the final radical concentration we adopted is 80 mmol·L^{-1}.

For similar reasons, since both organic solvents have a high affinity to oxygen, our previous experiences leads us to recommend the use of fully degassed solvents. Pre-degassing of the solvents can significantly reduce the content of paramagnetic oxygen in the RRP.

4.2 Sample Polarisation

4.2.1 Direct DNP and diffusion-assisted DNP

In fig. 4.2a we illustrate the build-up of the polarisation in the proton reservoir as a function of time. We can see that the final polarisation approaches 70% and that the build-up process is complete within minutes. When compared with the mono-exponential fit of experimental data, we can observe a slight deviation, which might be explained by the spatial inhomogeneity of the distributions of the radicals.

A typical build-up curve is presented here in fig. 4.2b. The pronounced pattern of stretched exponential curve suggests that the build-up of the proton polarisation in the RRP is accompanied by the diffusion of polarisation to micro-crystallites of the RFP. Such stretched exponential (or multi-exponential) patterns correspond well to the stretched exponential patterns of the particles, whose spherical-equivalent diameter is 5-10μm[§]. This matches the statistics from the SEM images.

4.2.2 Diffusion-assisted CP-DNP

The DNP enhanced proton polarisation can then be transferred to the carbon-13 spins in the RFP by CP at low temperatures. Although our micro-particulate DNP

[§]See fig. 2.7a
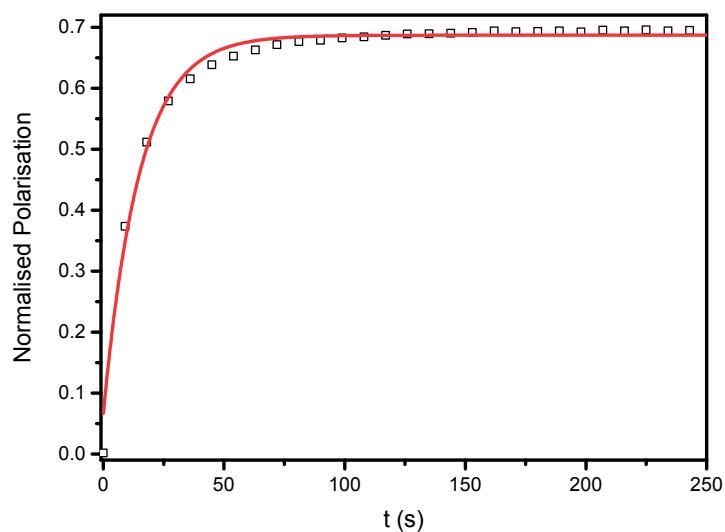
(a) The DNP build-up curve of proton in pure RRP sample.
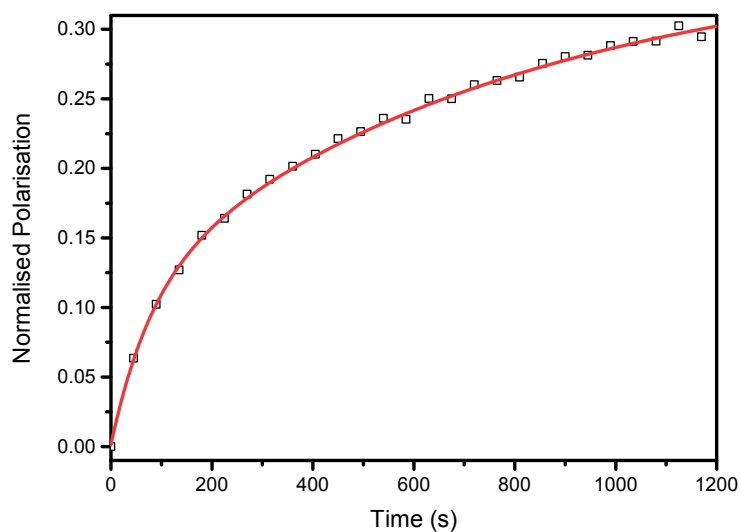
(b) The DNP build-up curve of proton in biphasic sample.

Figure 4.2 – The experimental result of proton build-up curve. Figure (a) shows the direct build-up curve of proton polarisation in pure RRP (black squares) and mono-exponential fit of experimental data (red line). The RRP is a organic solution of TEMPO-benzoate at the concentration of 80 mmol·L^{-1} in the mixture of h_8-toluene/h_8-toluene=8/2. Figure (b) shows the diffusion assisted build-up curve of average proton polarisation in a biphasic sample (black squares) and bi-exponential fit of experimental data (red line). The biphasic sample consists of 10 mg of sodium $[1-^{13}C]$ pyruvate (ground by hand) and 30 µL of organic solution of TEMPO-Benzoate at the concentration of 80 mmol·L^{-1} in the mixture of H_8-toluene/H_8-toluene=8/2.

sample formulation is drastically different from the usual glassy solutions, CP-DNP was performed in essentially the same manner. fig. 4.3b shows the stepwise build-up of the ^{13}C polarisation of sodium $[1-^{13}C]$pyruvate obtained by multiple-contact CP at 1.2 K. This may be compared with fig. 4.3a, a similar CP build-up measured for the same amount of sodium $[1-^{13}C]$pyruvate, but dissolved in a conventional glassy matrix H2O:D2O:glycerol-d8(2:3:5) doped with 40 m mol·L^{-1} TEMPOL.

Although these two CP build-up curves look similar, it is worth highlighting two major differences. First, the time between two consecutive CP contacts needs to be extended in biphasic samples to allow proton–proton spin diffusion to carry the polarisation into the RFP particles between CP steps (20 min in the biphasic sample, instead of 5 min in the conventional glassy matrix). Secondly, the carbon-13 relaxation between CP contacts, which usually limits the build-up of the carbon-13 polarisation, is essentially absent in the micro-particulate RFPs because of the absence of any thermal contact with the PAs. These two new features imply that, albeit the carbom-13 polarisation is slower to build-up, it can in principle achieve the same polarisation levels as the protons.

4.2.3   Extended lifetime of hyperpolarisation

The carbon-13 spins of metabolites dissolved in homogeneous glassy solutions are in contact through electron–nuclear dipolar interactions with the PAs that act as paramagnetic relaxation centres. In a biphasic formulation, on the other hand, the carbon-13 spins of the RFP are isolated from the PAs by the phase separation. As most of the molecules of interest (MOIs) reside in the core of the micro-crystallites, the distance between MOIs and PAs are generally on the order of micrometres, where the electron–nuclear dipolar interactions can be neglected. In fig. 4.4, we see how the spin-lattice relaxation time $T_1(^{13}C)$ of sodium $[1-^{13}C]$pyruvate can be significantly extended at 4.2 K and 6.7 T by switching from a glassy frozen solution, where $T_1(^{13}C)$ is 20 min, to a micro-particulate sample, where $T_1(^{13}C)$ is extended to 37 h. We measured relaxation times exceeding 20 h in[1-13C]glucose, and 5 h in $[U-^{13}C,^{15}N]$alanine and $[U-^{13}C_2,^{15}N]$glycine.

4.3   Remote Dissolution

Because of the radical-free nature of RFPs, the longitudinal relaxation times of carbon-13 spins can benefit from a remarkable extension. Hirsch *et al.* [97, 98] have reported that by using a cryogenic Dewar coupled with a weak static magnetic field, one can transport the $[1-^{13}C]$pyruvic acid that has been hyperpolarised by the brute force method. In their paper, they have pointed out the importance of preventing relaxation rate during the transfer, where the $T_1(^{13}C)$ can be drastically shorter than the value at 4 K and 6.7 T. There are two reasons: first, the sample is heated to higher temperatures,
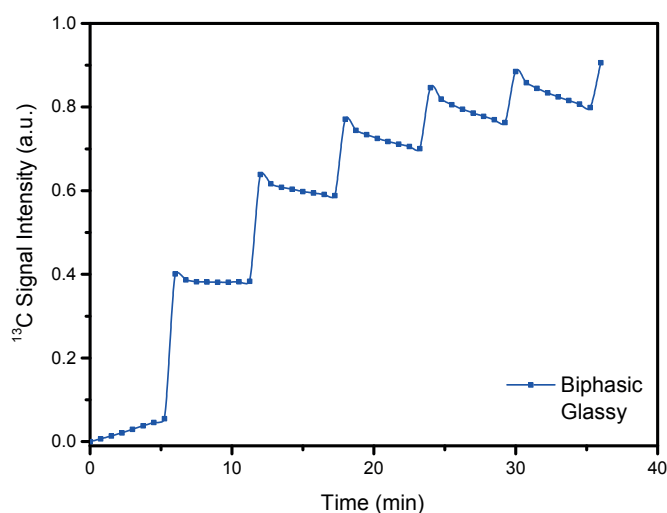
(a) The CP-DNP build-up curve of homogeneous glassy sample.
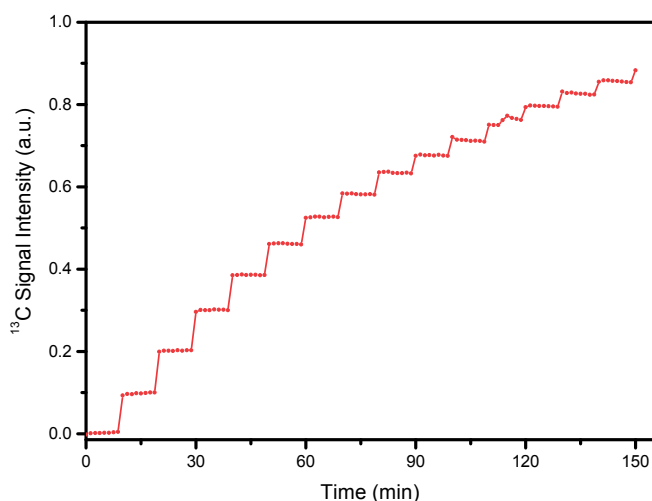
(b) The diffusion assisted CP-DNP build-up curve of biphasic sample.

Figure 4.3 – The experimental result of carbon CP build-up curve. Figure (a) shows the CP build-up curve of carbon polarisation in a homogeneous sample with CP interval of 300 s. The homogeneous sample is the frozen solution of sodium $[1-^{13}C]$ pyruvate (concentration at 3 mol·L^{-1}) in d_8-glycerol/D_2O/H_2O=5/3/2. TEMPOL serves as PA in the homogeneous polarising glass. The doping rate is 40 m mol·L−1. Figure (b) shows the diffusion assisted CP build-up curve of carbon polarisation in a biphasic sample with CP interval of 600 s. The biphasic sample consists of 20 mg of sodium $[1-^{13}C]$ pyruvate (ground by hand) and 60 μL of organic solution of TEMPO-Benzoate at the concentration of 40 mmol·L^{-1} in the mixture of d_8-toluene/d_8-THF/h_8-THF=8/2. We can not directly compare the two scales on y-axis.
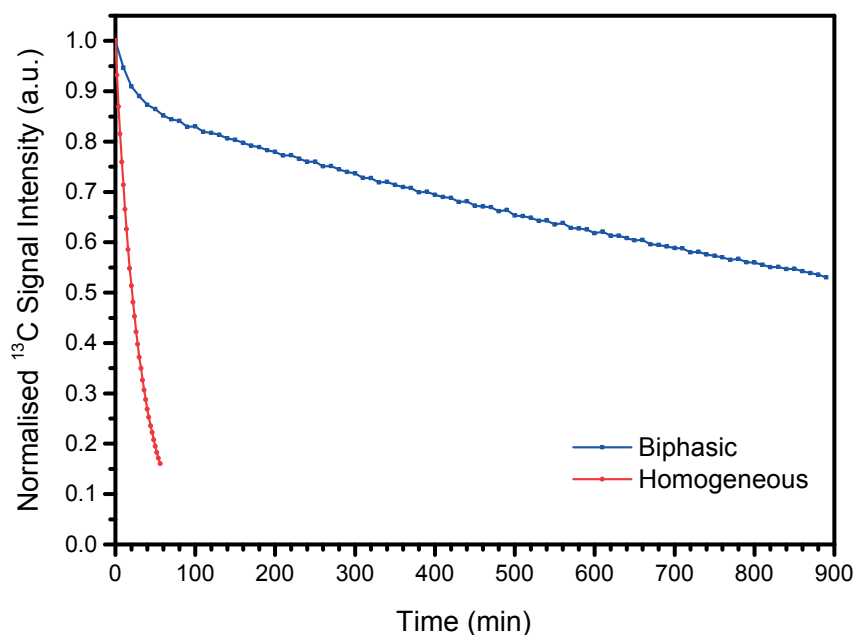
Figure 4.4 – The experimental result of carbon relaxation curve. The red line shows the re-laxation curve of carbon polarisation in a homogeneous sample. The homogeneous sam-ple is the frozen solution of sodium $[1-^{13}C]$pyruvate (concentration at 3 mol·L^{-1}) in d_8-glycerol/D_2O/H_2O=5/3/2. TEMPOL serves as PA in the homogeneous polarising glass. The do-ping rate is 40 m mol·L−1. The blue line shows the relaxation curve of carbon polarisation in a biphasic sample. The biphasic sample consists of 20 mg of sodium $[1-^{13}C]$ pyruvate (ground by hand) and 60 µL of organic solution of TEMPO-Benzoate at the concentration of 40 mmol·L^{-1} in the mixture of d_8-toluene/d_8-THF/h_8-THF=8/2. Both figures are normalised with respect to the initial signal intensity, respectively.

where more relaxation pathways occur by thermal interactions; second, during the transfer the sample is moved out of the high magnetic field, where low-field nuclear thermal mixing [34, 99, 100] can play a role as an extra source of relaxation for carbon-13 spins, as recently reported by Peat *et al.* [101].

4.3.1 Auxiliary magnets

In order to prevent low-field nuclear thermal mixing during the storage in low fields, We have designed a Halbach magnet that provides a constant magnetic field of 1.0 Tesla in the liquid helium cryogenic Dewar for transport.

For the same purpose, we have equipped the transfer stick with an auxiliary sole-noidal coil. The magnetic field produced by this coil is designed to be around 50 mT. The intensity of magnetic field matches the experimental result of Peat *et al.*. The coil was made with 100 turns per cm. A circuit current of 4 A was turned on in the coil

(a)

1.0 T Halbach
magnet
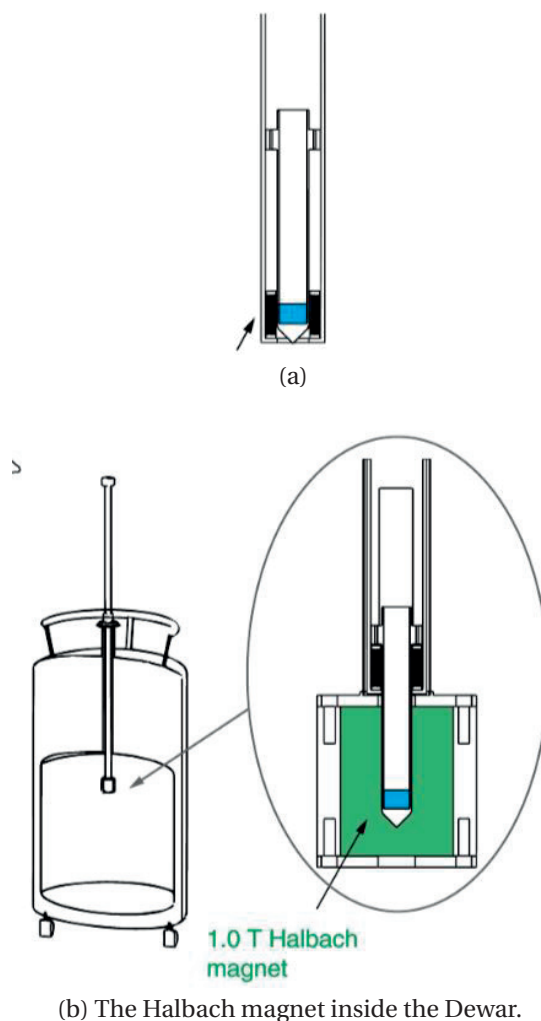
(b) The Halbach magnet inside the Dewar.

Figure 4.5 – The design of magnetic devices for the transport of hyperpoliarsied sample. Figure (a) shows the positioning of auxiliary solenoidal circuit inside the sample stick. This auxiliary solenoidal circuit generates a magnetic field of ca. 500 Gauss. Figure (b) shows the design of the Halbach magnet, which provides constant magnetic field during the storage.

before moving the sample out of polariser, and turned off after the sample was placed in the Halbach magnet inside the liquid helium Dewar of transportation.

4.3.2   Dissolution in the liquid helium cryogenic Dewar

The method used for dissolution in a liquid helium cryogenic Dewar is in principle the same as for the dissolution from in a polariser [102]:

5 mL of superheated D_2O at 420 K at a pressure of 1 MPa was injected onto the biphasic mixture inside the helium Dewar. After 700 ms of dissolution, the liquid in the sample holder was pushed through a polytetrafluoroethylene (Teflon) tube

through a 0.9 T magnetic tunnel to a home-made injector in a 11.7 T magnet. This transfer was achieved by using a flow of helium gas at 0.6 MPa for 4.5 s. Afterwards, the solution was injected into a 5 mm sample tube in 2 s. The whole process, including dissolution, transfer, and injection, requires *ca.* 7 s.

The carbon-13 spectra of the hyperpolarised metabolites in fig. 4.6 were obtained by looping a series of 5 deg pulses with subsequent signal acquisition at the intervals of 2 seconds.
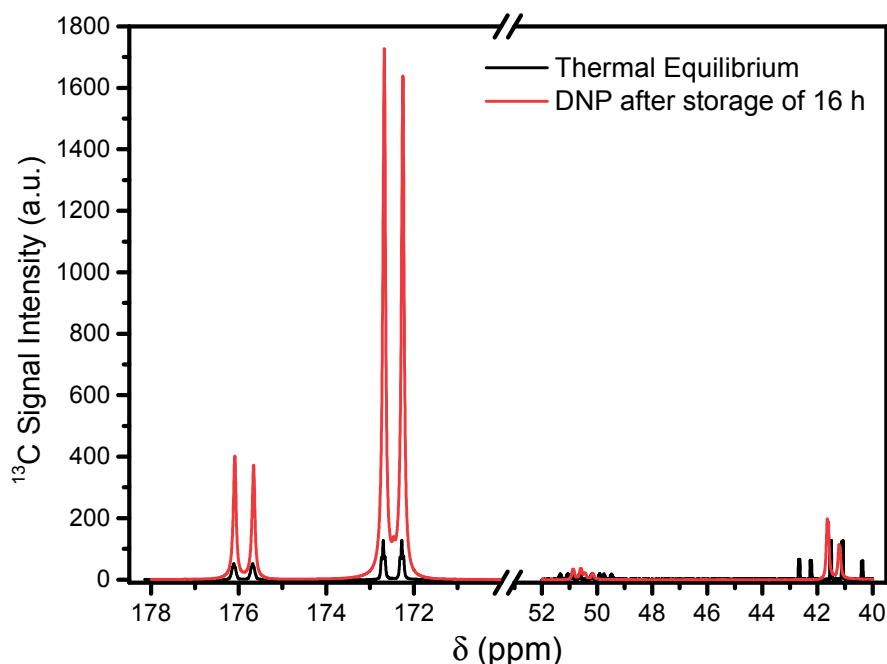
Figure 4.6 – The spectra of the mixture of 5.5 mg of $[U-^{13}C,^{15}N]$alanine and 9 mg of $[U-^{13}C_2,^{15}N]$glycine after remote dissolution in 11.7 T magnet. These amino-acids were first polarised at 1.2 K, 6.7 T with the impregnation of the solution of TEMPOL-benzoate (80 m mol·L^{-1}) in mixed solvent h_8-toluene/h_8-toluene=8/2. Then the hyperpolarised biphasic mixture is transferred into the updated Dewar for 16-hour-long storage at 4.2K, 1.0T. The dissolution performed inside the Dewar with overheated water, and the solution is pushed into the magnet through magnetic tunnel. The red line indicates the first ^{13}C spectrum recorded after injection with a 5°pulse. The black line shows the ^{13}C spectrum of thermal equilibrium signal of the same solution after complete relaxation of hyperpolarisation. The spectrum of thermal equilibrium was obtained with 16 times of 90°pulse at the recycle delay of 300 s.

4.4 Discussion

The experiment of remote dissolution was successful. Meanwhile, there is still plenty of scope for improvement.

The first issue is the distribution of particle sizes in the RFP. From the results of numerical simulations in chapter 2, we have acquired some empirical guidelines for the hyperpolarisation of heterogeneous samples by spin diffusion. In an optimised sample aiming at satisfactory overall direct proton polarisation from diffusion-relayed DNP, the average value of distribution of particle volumes in RFP should not exceed 2 μm, and the maximum spherical equivalent diameter of particles should not exceed 5 μm. If the distribution of the particle size does not change, we can also expect a nice carbon-13 polarisation with diffusion-relayed CP-DNP. Admittedly, we have not yet found a proper way of hand-grinding that permits us to obtain a narrow distribution of the volumes of crystallites on a sub-micrometric scale. Within commercial and economical limits for bench-top apparatus in a laboratory, a possible solutions could be the coupling the hand-grinding and sieve separation. In industrialised applications, zircon ball-milling coupled with sieve-levelling could be a good example of a top-down approach. Precipitation after immature nucleation would be an example of the bottom-up method.

Secondly, a complete study of low field relaxometry could contribute a great deal to the understanding of the hyperpolarisation, especially for sodium $[1-^{13}C]$pyruvate.

Last but not least, as both toluene and THF are hazardous for animals and human alike, great improvements can be envisaged from the use of bio-compatible solvents in the chemical formulation of RRPs.

5 Concept of Porous Polymeric Matrix for DNP

In the previous chapter, we have presented an attempt of remote DNP: Fine powder of MOI is impregnated in a glassy solution of PA. The (sub-)micrometric powder can then be hyperpolarised by spin-diffusion assisted DNP. Moreover, the lifetime of this hyperpolarisation is extended due to the segregation of paramagnetic centres. This methodology, in principle, can be adopted in the application of all crystalline solids.

Naturally, a following question came into our vision: What if the MOIs that we are using is a liquid at room temperature? We can no longer reduce the size of sample by mechanical operations. One answer to the question above is to use the liquid-liquid biphasic formulation, which bases upon the formation of emulsion between two immiscible liquids, say, water and heptane, water and xylene, or water and ethyl-acetate. Nevertheless, such formulation faces inevitably fundamental objection.

Because of the high energy of interface between two immiscible phases, the emulsions are thermodynamically unstable. Without adding any stabiliser, an established sample may well collapse from its emulsified state to two distinct phases within minutes or even seconds. Therefore, by convention, in the formulation of kinetically stable emulsion, the addition of surfactant is often of vital importance.

Though the incorporation of surfactants in the mixture can significantly enhance the kinetic stability of emulsions, we added the complexity of problematic by entering the reign of triphasic composition. First, the amphiphilic detergents forms micelles in the new triphasic system. As the micelles migrates freely between phases, they may extract radicals and redistribute them in the whole sample, which eradicates the separation between RRP and RFP. Second, once introduced in the system, the surfactant is immune to common physical separations, such as, filtration. They easily follow the flow of MOI and eventually arrives at the apparatus of detection, which complicates the final spectra. In case we are to study the dynamics of proteins, the surfactants would then act with macromolecules and cause undesirable side-effects.

Inspired by the micro-structure of the method of impregnation, where the MOI / RFP is solid and immobile while the solution of PA / RRP is liquid and mobile, we came up with a new scheme of phase separation: the fluid MOI be the RFP and a solid solution of PA serves as the porous matrix that holds the volume of liquid and acts as the source of hyperpolarisation during DNP experiments.

Similar ideas have already been proposed, of which the most famous is the HYPSO[103]. The main difference between HYPSO and the up-mentioned radical-doped porous matrix lies in the distribution of PA: In HYPSO silicate, PA are directly introduced on the surfaces of pores inside the silicate. This spatial alignment is not able to prevent the direct contact between paramagnetic centre and MOI / RFP. In the design of radical-doped porous matrix, we aim at immersing the radical inside the wall of matrix. Also, by surface decoration we kill the residual of radical on the surface. Therefore, the separation of RFP and RRP could be established. Besides, as suggested by the name <monolithic>, this design stands as a entire piece rather than fine powder, which further allows subtractive manufacturing for various shapes.

The Polymerised High Internal Phase Emulsion (poly-HIPE) was adopted as the main method for the preparation of RRP. Emulsions are heterogeneous mixtures consisting of two phases: the continuous external phase, and the internal phase dispersed inside the continuous phase. In the High Internal Phase Emulsions (HIPE), the volumetric percentage of discrete phase can reach up to 90%. The solidification of external phase and consequent removal of discrete phase, allows our obtaining a porous solid bulk, with merely 10-30% volume occupied by solid phase. The radicals are then incorporated inside the solid phase, being attached to the polymer through chemical bonds. The pores of the obtained material can be then fill with MOIs allowing to perform DNP experiments.

5.1 Synthesis and characteristication of radical-doped porous matrix

5.1.1 Synthesis and modification of polymeric matrix

The radical-doped porous bulk was prepared by free radical polymerisation (FRP) in HIPE. The protocol used was adapted after a previous described procedure [104]. In the literature, Sevsek *et al.* stopped at the step of polymeric bulk. We modified the composition and it is detailed in appendix A.3. The chemical composition, the porosity, and the concentration of doped radical of porous monolithic polarising matrices that are discussed in this chapter can be found in table A.5

The route of synthesis consists of two major steps: the polymerisation of monolithic block and are illustrated in fig. 5.1, fig. 5.2.

styrene (1)

1-(chloromethyl)-4-vinylbenzene (2)

Hydrophobic Monomers

+

sodium 4-vinylbenzenesulfinate (4)

Hydrophilic Monomer

Divinyl benzene (3)

Cross-Linking Agent

SPAN 80 (5)

Surfactants

1) KPS
H_2O, 24 h

2) Di-t-Bu-peroxide
C_6H_5-CH_3, 24 h

Polymeric precursor

Figure 5.1 – The schema of the multi-component heterogeneous polymerisation of polymeric precursor for PM-01 in the original route of synthesis of the radical-doped porous monolithic matrix.

Polymeric precursor

+ Radical

THF
r.t.
dark

Radical-doped Polymer

Radical = - H₂C-HN
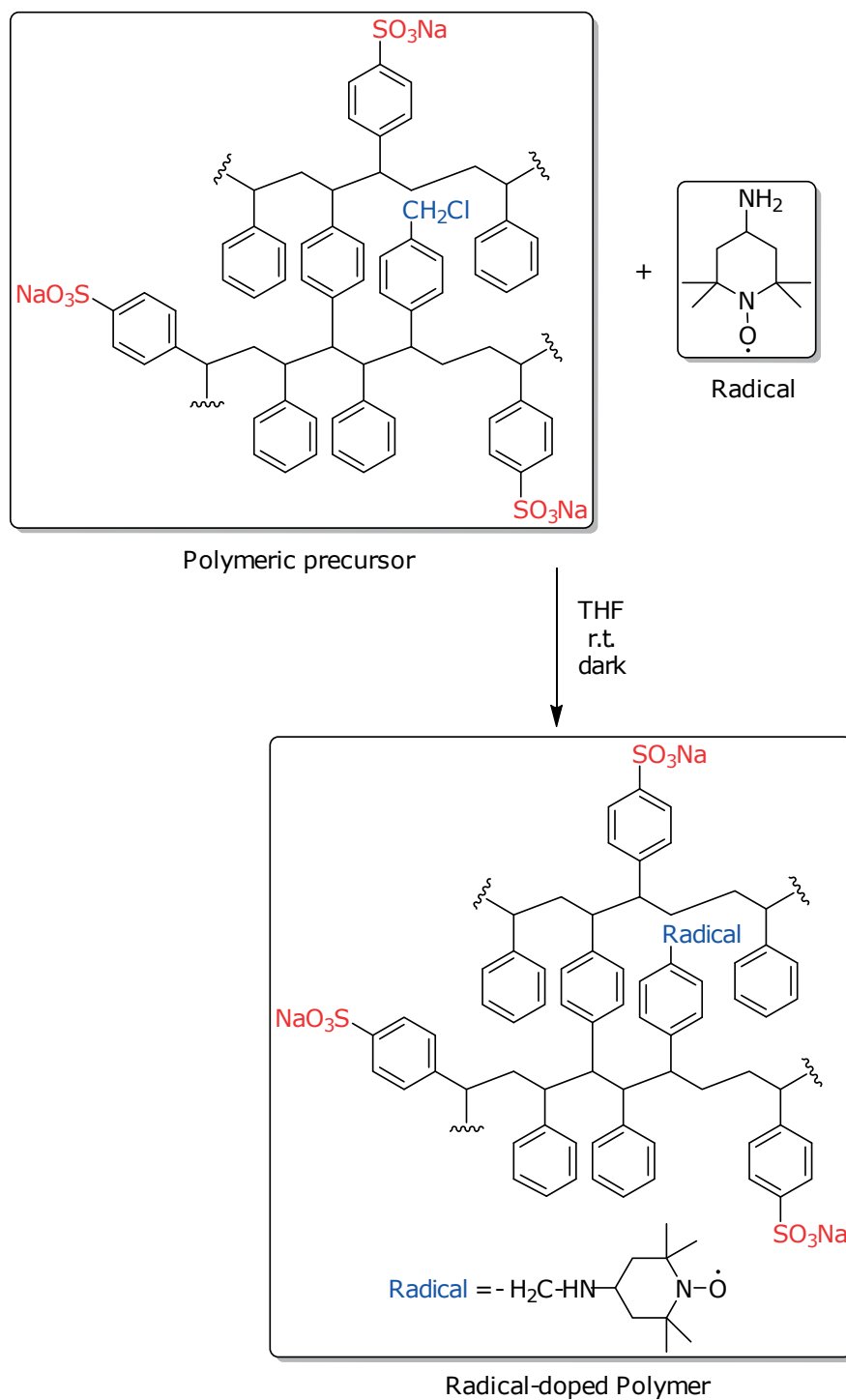
Figure 5.2 – The schema of the reaction of incorporating radical inside the polymeric precursor for PM-01 through chemical bond.

styrene (1)

1-(chloromethyl)-4-vinylbenzene (2)

ethylhexylacrylate (6)

Hydrophobic Monomers

sodium 4-vinylbenzenesulfinate (4)

Hydrophilic Monomer

Divinyl benzene (3)

Cross-Linking Agent

SPAN 80 (5)

Surfactants

1) KPS
H_2O, 24 h

2) Di-t-Bu-peroxide
C_6H_5-CH_3, 24 h

Polymeric precursor

Figure 5.3 – The schema of the multi-component heterogeneous polymerisation of polymeric precursor for PM-02 and PM-03 in the modified route of synthesis of the radical-doped porous monolithic matrix.
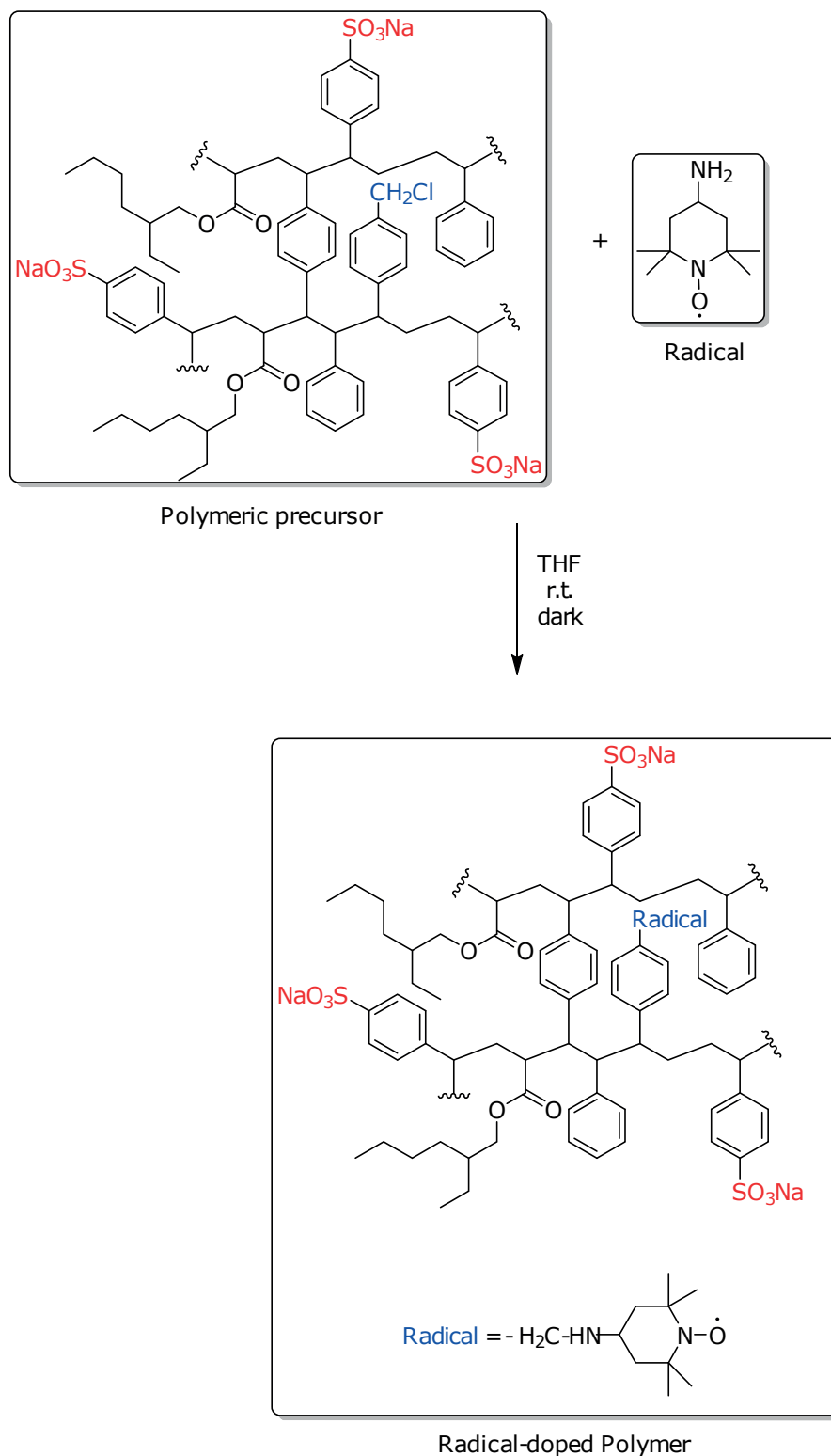
Figure 5.4 – The schema of the reaction of incorporating radical inside the modified polymeric precursor for PM-02 and PM-03 through chemical bond.

We started from a minor modification of literature (see [104] and appendix A.3), where only styrene (Sty) and divinylbenzene (DVB) are employed as the monomer for hydrophobic skeleton of the polymeric monolith PM-01. The role of 4-Vinylbenzyl chloride / 1-(chloromethyl)-4-vinylbenzene (VBC) as the oily monomers is to provide position of chemical anchoring for radicals in latter stage. The usage of sorbitan monooleate (Span 80) and sodium 4-vinylbenzenesulfinate (NaVBS) has two aspects: firstly, it serves as a surfactant that provides mechanical support of HIPE; secondly, after polymerisation, the NaVBS and the unsaturated molecules in SPAN 80 stays at the surface of polymeric matrix, which reduces the surface tension of hydrophobic backbone, and thus enhances the infiltration effect of the whole bulk. At the first stage, we expected the porosity of matrix is about 80%, so the ratio between aqueous phase and organic phase was set to be 1/4.
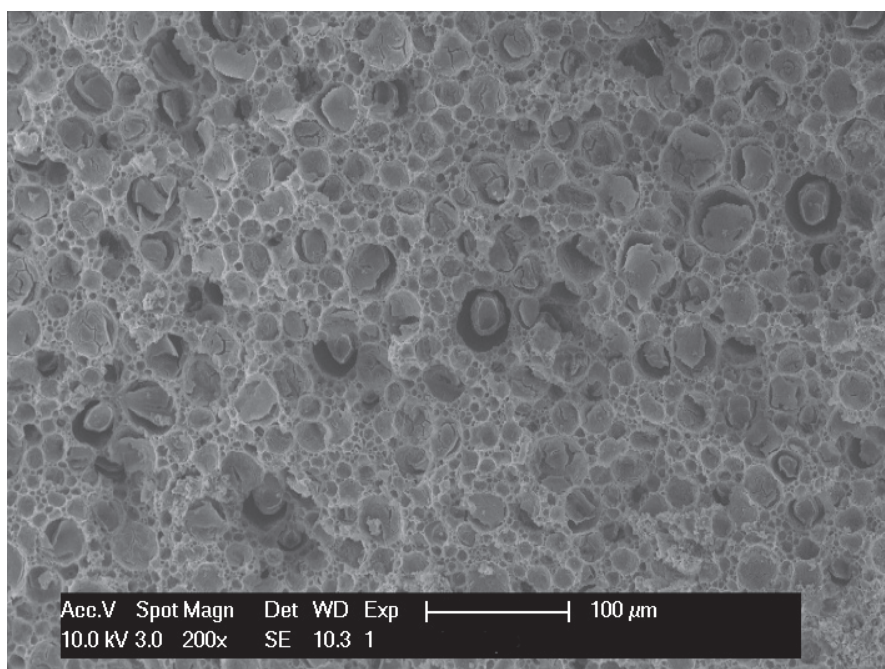
Figure 5.5 – The SEM picture of porous monolithic matrix PM-01.

After the preliminary tests, we found that the structure and the mechanical properties of such monolithic matrix still needs improvement. fig. 5.5 shows the microscopic appearance of the porous monolithic matrix from original route of synthesis. The average size of hole inside the matrix is on the order of 20-30 μm, which might be too big for DNP applications. In addition, the rigidity of this material is too high, and its toughness and ductility are both insufficient. The monolith breaks into small pieces with merely slight bending or torsion, which blocks the transferring tube during dissolution as a result of high pushing pressure in the pipeline. Modified route of synthesis then arose as the remedy of these problems.

The first modification intends to reduce the rigidity of polymer as the compromise for better toughness against external force. We then replace the Sty by 2-

ethylhexylacrylate (EHA), because the segments made of EHA units in a polymeric chain often has a much lower temperature of glassy transition with respect to pure polystyrene bulk and thus higher chain mobility. We also reduced the molar percentage of DVB in the organic phase from 90% to 30%, so as to decrease the crosslinking rate of polymer, in view of an extended ductility. fig. 5.6 demonstrates the SEM picture of porous matrix PM-02 after the first modification. The average size of pores reduces and the network of polymeric chain becomes denser.
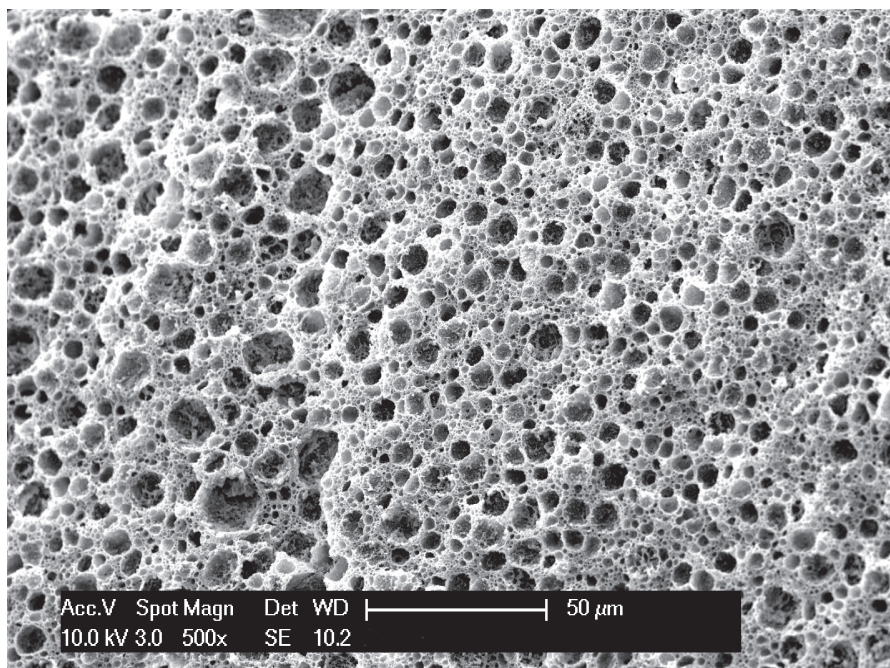
Figure 5.6 – The SEM picture of porous monolithic matrix PM-02 after the first modification of route of synthesis. The designed porosity equals 80%.

In view of better profile of the distribution of pore size inside the monolith, we conducted a second modification that reduces the overall porosity from 80% to 66%, which correspond to the ratio between aqueous phase and organic phase as 1/2.

We can see the microscopic structure of porous matrix PM03 after the second modification of chemical formulation in fig. 5.7. Though we can always observe the existence of large pores in fig. 5.7a, the average size of pore drops to the region of 1-10 μm. The inter-connectivity among neighbouring pores remains, as shown in fig. 5.7b.

5.2   DNP performance of radical-doped porous matrix

5.2.1   Relaxation of porous monolithic polarising matrix

The direct proton DNP build-up curve of PM-01 without MOI loading arrives 30% in both positive and negative mode at 1.2 K, 6.7 T. On the other hand, at around 4
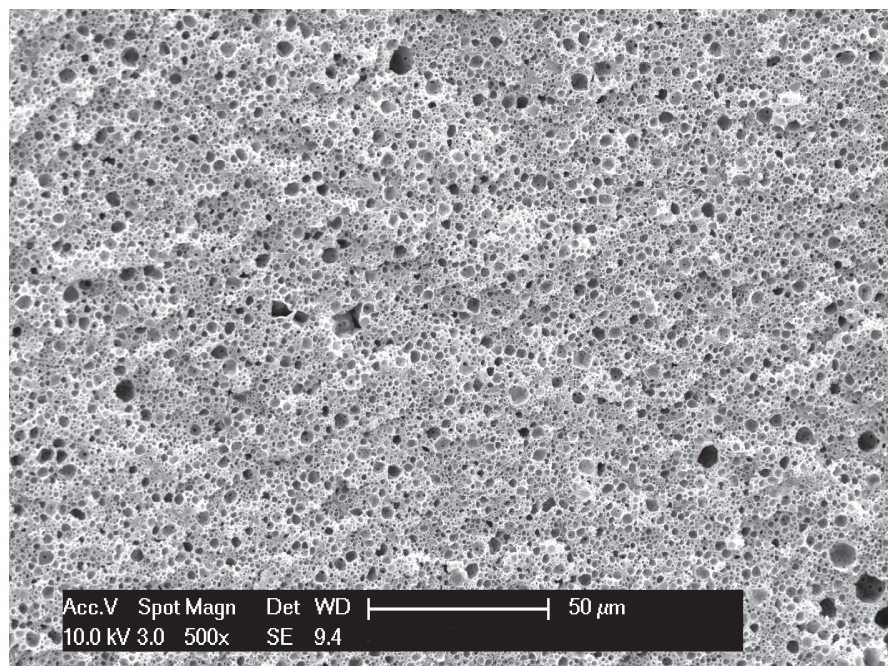
(a) SEM image of PM-03 with 500x magnificaiton.
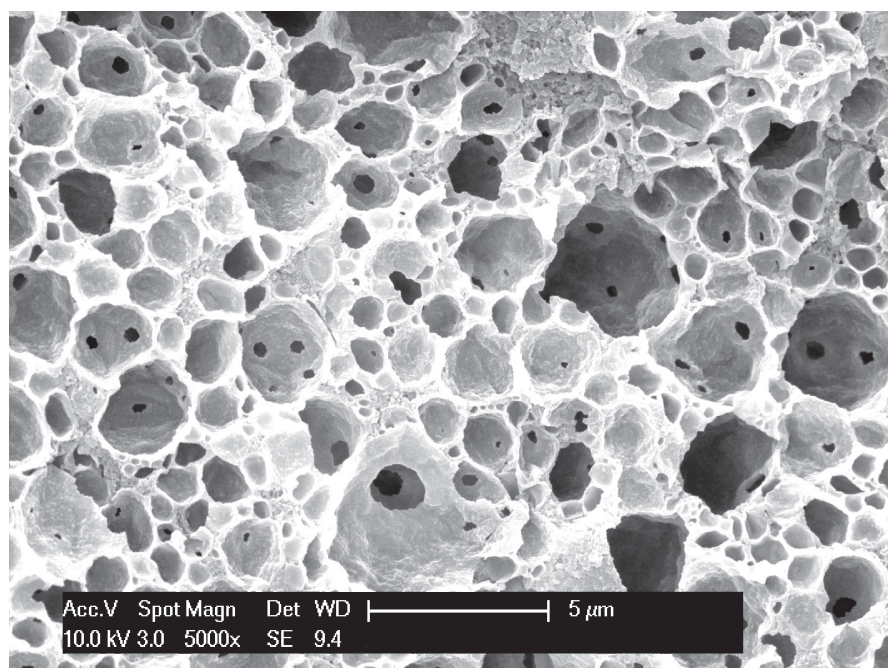
(b) SEM image of PM-03 with 5000x magnificaiton.

Figure 5.7 – The SEM picture of porous monolithic matrix of PM-03 after the second modification of route of synthesis. The designed porosity equals 66%.

K, 6.7 T the same sample can only be polarised to 2-3%. We then followed up with a brief study in the relaxometry of PM-01, and we compared the result with standard polystyrene reference for size-exclusion chromatography (Std PS ,as a compact bulk,
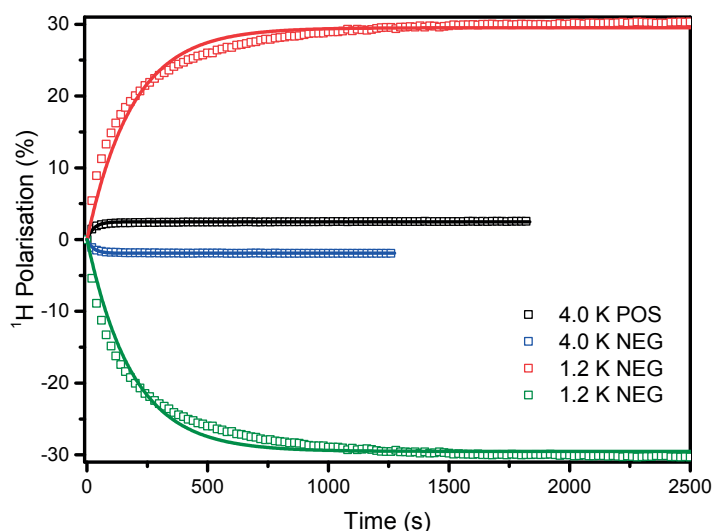
Figure 5.8 – The proton buld-up curve of the polarising matrix PM-01 without liquid loading.

$\overline{w_n} = 2 \cdot 10^5 Da$).

Table 5.1 – The parameters of bi-exponential fitting from saturation recovery experiment of PM-01 and standard polystyrene reference under different pre-treatments.

sample	condition	A^{fast}	t_1^{fast}	A^{slow}	t_1^{slow}
		(-)	(s)	(-)	(s)
PM-01	4.0K, No Degasing	0.60	6.74	0.40	39.9
PM-01	4.0K, Degasing	0.43	14.66	0.56	81.8
PM-01	1.2K, No Degasing	0.41	83.4	0.59	351
PM-01	1.2K, Degasing	0.48	361	0.52	1580
Std PS	4.0K, No Degasing	1.00	25.3	-	-

$$\text{Norm. Intensity}(t) = 1 - A_1^{fast} \cdot \exp(-\frac{t}{t_1^{fast}}) - A^{slow} \cdot \exp(-\frac{t}{t_1^{slow}})$$

$$A_1^{fast} + A^{slow} = 1$$

The relaxation profile of PM-01 (see fig. 5.9 and table 5.1) suggests first a pronounced multi-exponential pattern, which indicates two distinct relaxation mechanisms in the backbone of porous polarising matrix. The contrast of proton T_1 before and after sample degassing is ca. 2 times at 4.0 K and ca. 4 times at 1.2 K, which further manifests that of the oxygen biradical is heavily involved in the relaxation. According to Sevsek *et al.*, the specific surface area in this type of poly-HIPE-based porous material could be up to 300 $m^2 \cdot g^{-1}$, which permits a thorough adsorption of oxygen throughout the monolith. This explanation also supports the bi-exponential fit of experimental
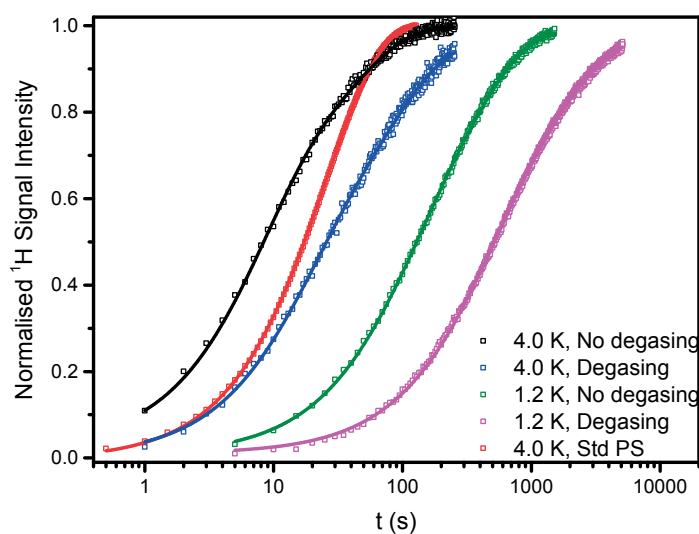
Figure 5.9 – The saturation recovery curve of PM-01 and standard polystyrene reference under different pre-treatments. The squares and line in black shows the experimental data and bi-exponential fit of PM-01 at 4.0 K, 6.7 T without pre-degasing. The squares and line in blue shows the experimental data and bi-exponential fit of PM-01 at 4.0 K, 6.7 T with pre-degasing. The squares and line in green shows the experimental data and bi-exponential fit of PM-01 at 1.2 K, 6.7 T without pre-degasing. The squares and line in magenta shows the experimental data and bi-exponential fit of PM-01 at 1.2 K, 6.7 T with pre-degasing. The squares and line in red shows the experimental data and bi-exponential fit of standard polystyrene reference for size-exclusion chromatography (as a compact bulk, $\overline{w_n} = 2 \cdot 10^5 Da$) at 4.0 K, 6.7 T without pre-degasing.

data. The adsorbed molecular oxygen acts as paramagnetic centres on the surface of polarising matrix, which yields the fast component of bi-exponential pattern. The core part of the polymeric backbone, which is less affected by oxygen biradical, contributes to the slower component of bi-exponential curve. It is worthy to note that, though the standard polystyrene sample is in a compact form, its $T_1(^1H)$ is also less than 30 s at 4.0 K, 6.7 T. The reason should be attributed as the nature of material.

5.2.2 Spin-diffusion assisted DNP of porous monolith with liquid-loading

From previous knowledge, we see that, in order to obtain precise experimental information from porous monolithic materials, we can not place enough attention on removing oxygen from the sample. Therefore, before the DNP study on pure PM-03 matrix, we chose to fill in the empty volume with d_4-MeOD after degassing, so as to avoid the contamination of oxygen. In fig. 5.10a we illustrate the proton build-up curve of PM-03 sample with d_4-MeOD under microwave irradiation of 187.75 GHz for positive hyperpolarisation. The final polarisation of this polarising matrix arrived at

ca. 12%.

The spin-diffusion assisted DNP was also conducted with pure water as liquid MOI. fig. 5.11b presents a distinct multi-exponential pattern, which suggest the hyperpolarisation created in polarising matrix crosses the interface between polymeric RRP and glass and flows into the RFP solid water inside the pores.

After polarising the RFP for 4 hours, we lifted twice the sample completely out of the polariser to verify if the hyperpolarisation of water in RFP could survive this transport (see fig. 5.11a). After the first lifting, both the signal intensity and line-shape of biphasic sample went through a thorough change. Around 63 % percent of initial polarisation lost during the first lift, while only ca. 10% loss was introduced by the second lift with respect to the signal after the first lift. This difference in the signal loss implies the different relaxation pathway in the biphasic sample, which in turn validates that the incorporated radical is not in direct contact with RFP.

Then we conducted a dissolution to extract the polarised water from inside the matrix. Similar to the experiment described in chapter 4, 5 mL of superheated D_2O at 420 K under the pressure of 1 MPa was injected onto the biphasic mixture inside the helium Dewar. After 0.5 s of dissolution, all the liquid in the sample holder were pushed through a polytetrafluoroethylene tube under the protection of a 0.9 T magnetic tunnel to a home-made injector in a 7.05 T magnet. This transfer was achieved by using a flow of helium gas at 0.6 MPa for 3.5 s. Afterwards, the solution was injected into a 5 mm sample tube in 2 s. The whole process, including dissolution, transfer, and injection, covers ca. 6 s. We have obtained a maximal proton polarisation of 2.1% after dissolution. The longitudinal relaxation time of hyperpolarised water is 20.8 s at room temperature, which suggests that no paramagnetic species travelled along with water during the transfer. We have conducted several times the dissolution, both with and without filtrating the polarising matrix. The decay rate of hyperpolarisation does not vary, which confirms a satisfactory confinement of PA inside the wall of polarising matrix.

5.3   Discussion

It is an intriguing phenomenon to us that the degassing process significantly improves the proton polarisation in the polarising matrix without liquid-loading. A possible hypothesis lies in the combination of the huge surface-volume of the porous monolith and the high inherent affinity to oxygen of the polymer. If we do not perform degassing to the porous sample, air, or more specifically, the molecules of oxygen shall adsorb on the surface of polymer. At low temperature, the two free electrons in the anti-bond orbital of oxygen molecule couples strongly with the PAs doped in the polarising matrix, which competes with the hyperfine coupling, and thus dampers the DNP performance. After degassing, the interference of oxygen in the DNP process

is eliminated. The final proton polarisation is therefore optimised.

The low polarisation of water after dissolution might be due to the insufficient polarisation in the biphasic sample of waterand monolith. The long trend of stretched exponential in fig. 5.10b indicates a very inhomogeneous distribution pore size with a mean value larger than 5 μm. We will continue optimising the composition and porosity of the polymeric matrix.

Also, we envisage a series of porous material with different radical doping rate, in view of obtaining the best compromise between cooling power of magnetic energy and the paramagnetic relaxation in RRP. Higher polarisation could also be obtained from better efficiency of de-oxygenation during DNP process.
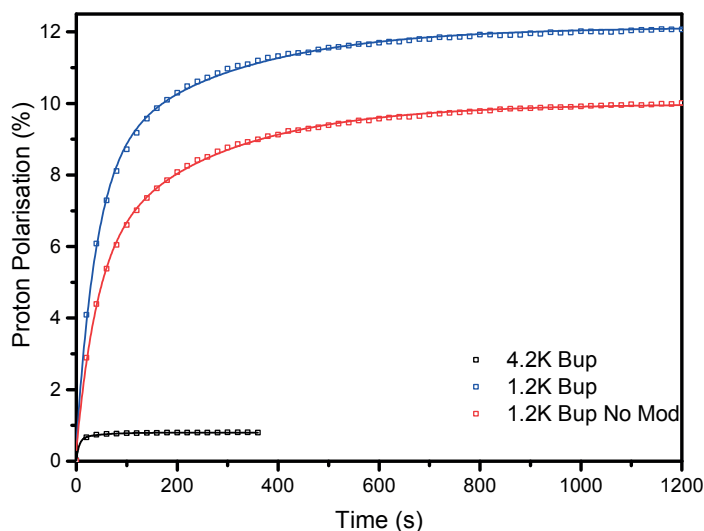
(a) Proton build-up curve of the polarising matrix PM-03 fully soaked with d_4-MeOD.
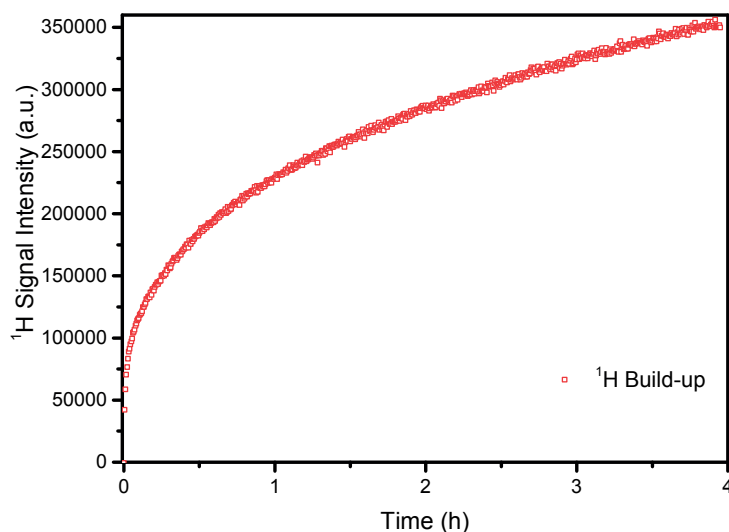
(b) Proton build-up curve of the polarising matrix PM-03 fully soaked with H_2O.

Figure 5.10 – Proton build-up curve of the polarising matrix PM-03 soaked with different loading liquid. The DNP experiment was performed with microwave irradiation at 187.7 GHz for positive DNP effect. Figure (a) shows the build-up profile of pure backbone of polarising matrix, in which the volume of pores are filled with d_3-MeOD. The black line shows the build-up curve at 4.2 K with modulation of microwave frequency at 50 kHz. The red line shows the build curve at 1.2 K without modulation of microwave frequency. The blue line shows the build-up curve at 1.2 K with microwave frequency at 50 kHz. Figure (b) shows the the build-up profile of pure backbone of polarising matrix, in which the volume of pores are filled with H_2O. The data was recorded with modulation of microwave frequency at 50 kHz.
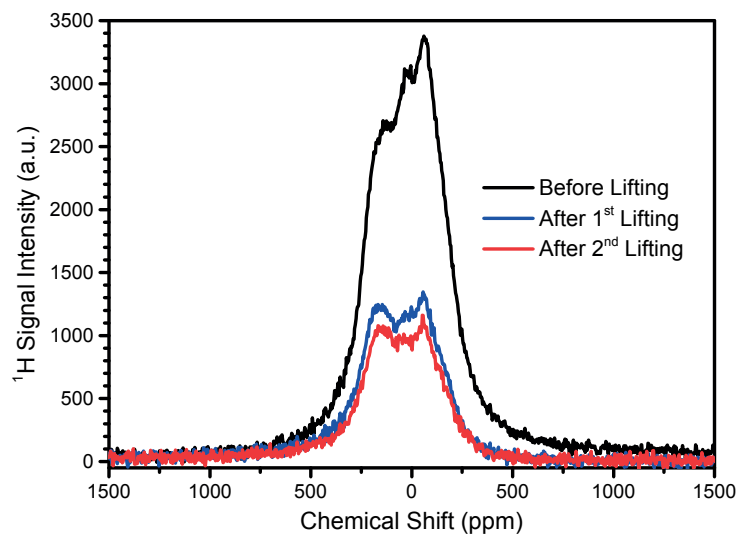
(a) Proton spectra of polarising matrix PM-03 fully soaked with H_2O before and after lifting experiment.
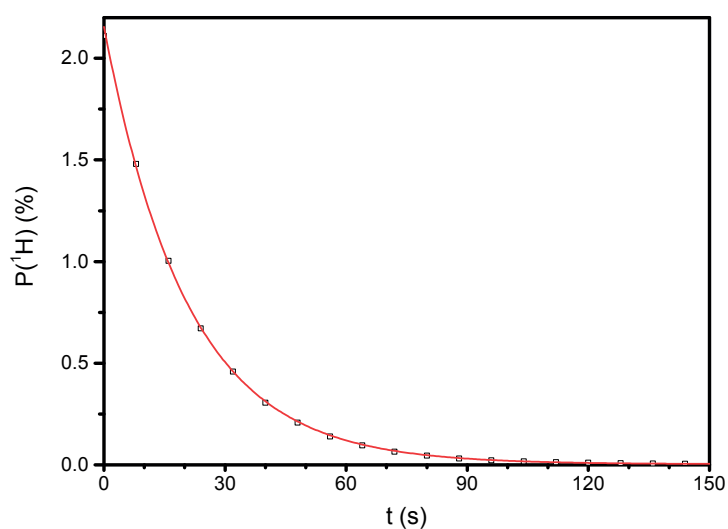
(b) Proton relaxation curve of hyperpolarised H_2O after dissolution.

Figure 5.11 – Figure (a) shows the proton spectra of water soaked porous monolith before and after lifting completely out of the polariser. Black line indicates the spectrum before lifting. Blue line indicates the spectrum after the first lifting. Red line indicates the spectrum after the second lifting. Figure (b) shows the exponential decay of hyperpolarisation of water after the dissolution of water in the pores of polarising matrix. The complete curve of relaxation was measured with 2 °pulses at the interval of 2 s.

6 Conclusions

In this thesis, an extensive numerical treatment has been described of the time-dependent evolution of nuclear magnetic energy in the biphasic samples for dissolution dynamic nuclear polarisation (d-DNP) containing spins such as ^1H and ^{13}C. Under conditions where the high temperature approximation is no longer valid, we propose to use the absolute spin polarisation as new measure of the system and study the accumulation of nuclear magnetic energy during direct DNP build-up, the transfer of polarisation through cross-polarisation (CP), and the relaxation of the nuclear magnetisation before dissolution. From the results of simulations, we have found a series of characteristic values of the system that allow one to improve performance of diffusion-relayed DNP, as described in chapter 2:

In view of achieving the best possible performance of direct DNP, the size of particulate radical-free phases (RFPs) containing the molecules of interest (MOIs) should be below 5 microns, and the equivalent thickness of the layers of the radical-rich phase (RRP) around the particles containing the MOIs should be on the order of 1 micron. This shows that the volumetric ratios between the two phases are interdependent. Also, the calculations suggest that the fully protonated RRP facilitate the fast spin diffusion in biphasic systems throughout the diffusion-assisted DNP process.

Concerning the transfer of magnetic energy between proton and carbon-13 reservoirs during the CP-DNP build-up, the optimal duration of the CP contact time and the duration of the interval between CP contacts in multiple CP series are complex functions that depend on the sample. Though still fairly primitive, our simulations have demonstrated their potential in predicting the time-dependent evolution of the spatial distribution of polarisation throughout the biphasic samples. By iterative applications of this numerical scheme, we can then optimise the experimental set-up to obtain the best compromise between overall experimental time and the final level of the nuclear polarisation.

From the simulated relaxation profiles, we can see that the hyperpolarisation of

low-γ nuclei in selectively enriched biphasic samples may survive for hours and even days in the RFP, regardless of the presence of polarising agents (PAs) in the RRP of the biphasic samples, so that the lifetime of nuclear magnetisation is greatly extended compared to conventional glassy samples routinely used in d-DNP experiments. Our simulations verify the principle of the extension of longitudinal relaxation times of hyperpolarised samples as well as the resulting possibility of remote transportation of hyperpolarised material of biological and medical interest.

In chapter 3, we investigated the efficiency of CP at low temperatures as a function of electron polarisation, focusing on the relationship between partial saturation of the electron spins and the time constant of nuclear longitudinal relaxation in the rotating frame. Using a similar numerical treatment as in chapter 2, we obtained a practical method for estimating the experimental parameters of the build-up of CP-DNP in a homogeneous glassy sample. Based on these calculations, we further analysed a microwave-gated scheme that largely increases the final carbon polarisation at steady state to 70-90%, and reduces the time requirements and total duration of CP-DNP experiments.

To validate our practical approach and verify the hypothesis that hyperpolarisation can be preserved and made transportable, we proposed two orthogonal methodologies for preparing biphasic d-DNP samples. The first one relies on the impregnation of particulate MOI crystals in spin glasses doped with PAs. Using this approach, we have obtained an extended lifetime of ^{13}C hyperpolarisation in fully labelled amino acids, which is demonstrated by its survival overnight in a Dewar of liquid helium at 4.2 K in a static magnetic field of 1.0 T generated by a Halbach magnet. The next stage of this project would focus on the coupling technique between transportable hyperpolarised MOI with remote detecting methods, for example, *in-vivo*, and even preclinical, MRI.

Another approach focuses on polarising frozen liquids of MOI using a radical-doped porous polymeric matrix. Once filled the pores are filled with liquid MOIs, the sample can reach 30%. We can then obtain a radical-free solution of MOI with a proton polarisation up to around 2% from dissolution.

A Appendix

A.1 Supplimentrary information of numerical simulation

A.1.1 The numerical values of parameters used in simulation

In this section, we summarise all the numerical parameters that we used in the simulation of DNP profiles in biphasic sample as well as in the microwave-gated experiments.

Table A.1 – *Physical properties used in the numerical simulation of direct diffusion-relayed DNP*

	Parameter	Symbol	Unit	RRP 10%^1H	RRP 20%^1H	RRP 50%^1H	RRP 80%^1H	RRP 100%^1H	RFP Pyruvate	RFP Glycine
	Molar energy capacity	$C_p^{\,H}$	J·mol⁻¹				$5.69 \cdot 10^{-2}$			
	Spin density	c^H	mol·m⁻³	$1.1 \cdot 10^4$	$2.2 \cdot 10^4$	$5.5 \cdot 10^4$	$8.8 \cdot 10^4$	$1.1 \cdot 10^5$	$3.3 \cdot 10^4$	$1.07 \cdot 10^5$
	Damping actor	$d_a^{\,H}$	J·m⁻³	$6.26 \cdot 10^2$	$1.25 \cdot 10^3$	$3.13 \cdot 10^3$	$5.01 \cdot 10^3$	$6.26 \cdot 10^3$	$1.88 \cdot 10^3$	$6.09 \cdot 10^3$
^1H	Spin diffusivity	D^H	m²·s⁻¹	$2.0 \cdot 10^{-15}$	$2.5 \cdot 10^{-15}$	$3.3 \cdot 10^{-15}$	$3.9 \cdot 10^{-15}$	$4.2 \cdot 10^{-15}$	$2.8 \cdot 10^{-15}$	$4.2 \cdot 10^{-15}$
	Spin conductivity	κ^H	W·m⁻¹	$1.2 \cdot 10^{-12}$	$3.1 \cdot 10^{-12}$	$1.0 \cdot 10^{-11}$	$2.0 \cdot 10^{-11}$	$2.6 \cdot 10^{-11}$	$5.3 \cdot 10^{-12}$	$2.5 \cdot 10^{-11}$
	Build-up Time	$t_{Bup}^{\,H}$	s	65.4	65.4	65.4	65.4	65.4	-	-
	Relaxation Time (L)	$T_1^{\,H}$	s	100	100	100	100	100	6000	6000
	Max Polarisation	$P_\infty^{\,H}$	-	0.684	0.684	0.684	0.684	0.684	-	-
	Heat Source	$q_{Bup}^{\,H}$	J·m⁻³·s⁻¹	9.57	19.12	47.87	76.63	95.75	-	-
		$q_{Relax}^{\,H}$	J·m⁻³·s⁻¹	6.26	12.5	31.3	50.1	62.6	0.31	1.02
		$Q_{const}^{\,H}$	J·m⁻³·s⁻¹	4.28	8.55	21.41	34.27	42.82	-	-
	Molar energy capacity	$C_p^{\,C}$	J·mol⁻¹				$1.43 \cdot 10^{-2}$			
	Spin density	c^C	mol·m⁻³	$6.9 \cdot 10^2$	$6.9 \cdot 10^2$	$6.9 \cdot 10^2$	$6.9 \cdot 10^2$	$6.9 \cdot 10^2$	$1.1 \cdot 10^4$	$4.28 \cdot 10^4$
	Damping actor	$d_a^{\,C}$	J·m⁻³	9.87	9.87	9.87	9.87	9.87	157	612
^{13}C	Spin diffusivity	D^C	m²·s⁻¹	$3.3 \cdot 10^{-18}$	$3.3 \cdot 10^{-18}$	$3.3 \cdot 10^{-18}$	$3.3 \cdot 10^{-18}$	$3.3 \cdot 10^{-18}$	$1.4 \cdot 10^{-17}$	$8.3 \cdot 10^{-17}$
	Spin conductivity	κ^C	W·m⁻¹	$3.3 \cdot 10^{-18}$	$3.3 \cdot 10^{-18}$	$3.3 \cdot 10^{-18}$	$3.3 \cdot 10^{-18}$	$3.3 \cdot 10^{-18}$	$2.1 \cdot 10^{-15}$	$5.1 \cdot 10^{-14}$
	Build-up Time	$t_{Bup}^{\,C}$	s	1800	1800	1800	1800	1800	-	-
	Relaxation Time (L)	$T_1^{\,C}$	s	2400	2400	2400	2400	2400	36000	36000
	Max Polarisation	$P_\infty^{\,C}$	-	0.207	0.207	0.207	0.207	0.207	-	-
	Heat Source	$q_{Bup}^{\,C}$	J·m⁻³·s⁻¹	$5.5 \cdot 10^{-3}$	$5.5 \cdot 10^{-3}$	$5.5 \cdot 10^{-3}$	$5.5 \cdot 10^{-3}$	$5.5 \cdot 10^{-3}$	$4.4 \cdot 10^{-3}$	$1.7 \cdot 10^{-2}$
		$q_{Relax}^{\,C}$	J·m⁻³·s⁻¹	$4.1 \cdot 10^{-3}$	$4.1 \cdot 10^{-3}$	$4.1 \cdot 10^{-3}$	$4.1 \cdot 10^{-3}$	$4.1 \cdot 10^{-3}$	$4.4 \cdot 10^{-3}$	$1.7 \cdot 10^{-2}$
		$Q_{const}^{\,C}$	J·m⁻³·s⁻¹	$1.1 \cdot 10^{-3}$	$1.1 \cdot 10^{-3}$	$1.1 \cdot 10^{-3}$	$1.1 \cdot 10^{-3}$	$1.1 \cdot 10^{-3}$	-	-

Table A.2 – Physical properties used in the numerical simulation of diffusion-relayed CP-DNP

	Parameter	Symbol	Unit	RRP					RFP	
				$10\%\,^1H$	$20\%\,^1H$	$50\%\,^1H$	$80\%\,^1H$	$100\%\,^1H$	Pyruvate	Glycine
^1H	Spin density	c^H	mol·m^{-3}	$1.1\cdot10^4$	$2.2\cdot10^4$	$5.5\cdot10^4$	$8.8\cdot10^4$	$1.1\cdot10^5$	$3.3\cdot10^4$	$1.07\cdot10^5$
	Relaxation Time (R)	$T_{1\rho}^H$	ms	10	10	10	10	10	200	200
^{13}C	Spin density	c^C	mol·m^{-3}	$6.9\cdot10^2$	$6.9\cdot10^2$	$6.9\cdot10^2$	$6.9\cdot10^2$	$6.9\cdot10^2$	$1.1\cdot10^4$	$4.28\cdot10^4$
	Relaxation Time (R)	$T_{1\rho}^H$	ms	10	10	10	10	10	200	200
	Average Dipolar Coupling	b_{H-C}	Hz	12000	12000	12000	12000	12000	1500	5500

Table A.3 – Physical properties used in the numerical simulation of microwave-gated CP

Parameter		Symbol	Unit	RRP Sodium $[1-^{13}C]$Acetate
Concentration		c^H	mol·m^{-3}	$3\cdot10^3$
^1H Spin density		c^H	mol·m^{-3}	$2.0\cdot10^4$
Build-up Time		$t_{Bup}^{\,H}$	s	150
Relaxation Time (R)	w/ MW	$T_{1\rho}^{H}$	ms	10
	w/o MW			100
Max Polarisation		$P_\infty^{\,H}$	-	0.7
^{13}C Spin density		c^C	mol·m^{-3}	$3.225\cdot10^3$
Build-up Time		$t_{Bup}^{\,H}$	s	6000
Relaxation Time (R)	w/ MW	$T_{1\rho}^{H}$	ms	7.4
	w/o MW			100
Max Polarisation		$P_\infty^{\,H}$	-	0.21
Average Dipolar Coupling		b_{H-C}	Hz	373

A.1.2   The script of numerical model for simulation

In this section, we attach all the initial codes of numerical simulation that are used in the coupled runtime environment of COMSOL Multiphysics®with LiveLink^TM for MATLAB®.

Run-time Sequence: Main

```
1     %
2     % CoeffPDE1D_1H-13C_20160525.m
3     %
4
5     % Model last updateed on June 15 2016, 18:16 by Xiao JI.
6     %
7
8     numofCP = 1;
9     seqBlockNum = numofBlocks(numofCP);
10    global blocSeqParam
11    blocSeqParam = seqGen(seqBlockNum);
12    iterStrFunc
13
14
15    PhysChemParams
16
17    import com.comsol.model.*
18    import com.comsol.model.util.*
19
20    model = ModelUtil.create('Model');
21    model.modelPath('C:\COMSOL\M');
22    model.modelNode.create('comp1');
23
24    ParamsSpec
25
26    model.geom.create('geom1', 1);
27    model.geom('geom1').create('i1', 'Interval');
28    model.geom('geom1').feature('i1').set('p2', 'r_core');
29    model.geom('geom1').create('i2', 'Interval');
30    model.geom('geom1').feature('i2').set('p1', 'r_core');
31    model.geom('geom1').feature('i2').set('p2', 'r_core+r_shell');
32    model.geom('geom1').run('fin');
33
34    model.mesh.create('mesh1', 'geom1');
35    model.mesh('mesh1').automatic(false);
36    model.mesh('mesh1').feature('size').set('table', 'semi');
37    model.mesh('mesh1').feature('size').set('hauto', '1');
38    model.mesh('mesh1').feature('edg1').create('dis1', 'Distribution');
39    model.mesh('mesh1').feature('edg1').create('dis2', 'Distribution');
40    model.mesh('mesh1').feature('edg1').feature('dis1').selection.set([1]);
41    model.mesh('mesh1').feature('edg1').feature('dis2').selection.set([2]);
42    model.mesh('mesh1').feature('edg1').feature('dis1').set('numelem', 'r');
43    model.mesh('mesh1').feature('edg1').feature('dis1').set('type', 'predefined');
44    model.mesh('mesh1').feature('edg1').feature('dis1').set('elemratio', '8');
45    model.mesh('mesh1').feature('edg1').feature('dis1').set('reverse', 'on');
46    model.mesh('mesh1').feature('edg1').feature('dis1').set('method', 'geometric');
47    model.mesh('mesh1').feature('edg1').feature('dis1').set('elemcount','r_core/2e-9');
48    model.mesh('mesh1').feature('edg1').feature('dis2').set('type', 'predefined');
49    model.mesh('mesh1').feature('edg1').feature('dis2').set('elemratio', '15');
50    model.mesh('mesh1').feature('edg1').feature('dis2').set('method', 'geometric');
51    model.mesh('mesh1').feature('edg1').feature('dis2').set('elemcount','r_shell/1e-9');
52    model.mesh('mesh1').run;
53
54    for i = 1:seqBlockNum
55        if i == 1
56            % First block needs specification of evolution in 2 reservoirs
57            model.physics.create(ci(i), 'CoefficientFormPDE', 'geom1',  {'u1H' 'u13C'});
58            model.physics(ci(i)).prop('Units').set('SourceTermQuantity', 'powerdensity');
59            model.physics(ci(i)).prop('Units').set('DependentVariableQuantity', 'temperature
                  ');
60        else
```

Appendix A. Appendix

```
61          % Following blocks follow the specification of the 1st
62          model.physics.create(ci(i), 'CoefficientFormPDE', 'geom1', strcat('u', num2str(i)
                ));
63          model.physics(ci(i)).prop('Units').set('SourceTermQuantity', 'powerdensity');
64          model.physics(ci(i)).prop('Units').set('DependentVariableQuantity', 'temperature
                ');
65          model.physics(ci(i)).field('dimensionless').field('u');
66      end
67  end
68
69  for i = 1:seqBlockNum
70      if i < seqBlockNum
71          if i == 1
72              % First block of BUP Cond. with initial condtion P|_{t=0} \equiv 0
73              model.physics(ci(i)).feature('init1').set('u1H', 'Pini1H_1');
74              model.physics(ci(i)).feature('init1').set('u13C', 'Pini13C_1');
75              model.physics(ci(i)).feature.duplicate('init2', 'init1');
76              model.physics(ci(i)).feature('init2').selection.set([2]);
77              model.physics(ci(i)).feature('init2').set('u1H', 'Pini1H_2');
78              model.physics(ci(i)).feature('init2').set('u13C', 'Pini13C_2');
79
80              model.physics(ci(i)).feature('cfeq1').setIndex('c', 'kappa1H_1', 0);
81              model.physics(ci(i)).feature('cfeq1').setIndex('c', 'kappa13C_1', 3);
82              model.physics(ci(i)).feature('cfeq1').setIndex('a', 'qsAntiBup1H_1', 0);
83              model.physics(ci(i)).feature('cfeq1').setIndex('a', 'qsAntiBup13C_1', 3);
84              model.physics(ci(i)).feature('cfeq1').setIndex('f', 'Qbup1H_1', 0);
85              model.physics(ci(i)).feature('cfeq1').setIndex('f', 'Qbup13C_1', 1);
86              model.physics(ci(i)).feature('cfeq1').setIndex('da', 'NuEnergy1H_1', 0);
87              model.physics(ci(i)).feature('cfeq1').setIndex('da', 'NuEnergy13C_1', 3);
88              model.physics(ci(i)).feature('cfeq1').setIndex('be', '-2*kappa1H_1/x', 0);
89              model.physics(ci(i)).feature('cfeq1').setIndex('be', '-2*kappa13C_1/x', 3);
90
91              model.physics(ci(i)).feature.duplicate('cfeq2', 'cfeq1');
92              model.physics(ci(i)).feature('cfeq2').selection.set([2]);
93              model.physics(ci(i)).feature('cfeq2').setIndex('c', 'kappa1H_2', 0);
94              model.physics(ci(i)).feature('cfeq2').setIndex('c', 'kappa13C_2', 3);
95              model.physics(ci(i)).feature('cfeq2').setIndex('a', 'qsAntiBup1H_2', 0);
96              model.physics(ci(i)).feature('cfeq2').setIndex('a', 'qsAntiBup13C_2', 3);
97              model.physics(ci(i)).feature('cfeq2').setIndex('f', 'Qbup1H_2', 0);
98              model.physics(ci(i)).feature('cfeq2').setIndex('f', 'Qbup13C_2', 1);
99              model.physics(ci(i)).feature('cfeq2').setIndex('da', 'NuEnergy1H_2', 0);
100             model.physics(ci(i)).feature('cfeq2').setIndex('da', 'NuEnergy13C_2', 3);
101             model.physics(ci(i)).feature('cfeq2').setIndex('be', '-2*kappa1H_2/x', 0);
102             model.physics(ci(i)).feature('cfeq2').setIndex('be', '-2*kappa13C_2/x', 3);
103
104         elseif mod(i, 2) == 1 & i<seqBlockNum & i>1
105             % Odd block of Bup Cond. inside the sequence
106             model.physics(ci(i)).feature('cfeq1').setIndex('c', 'kappa1H_1', 0);
107             model.physics(ci(i)).feature('cfeq1').setIndex('c', 'kappa13C_1', 3);
108             model.physics(ci(i)).feature('cfeq1').setIndex('a', 'qsAntiBup1H_1', 0);
109             model.physics(ci(i)).feature('cfeq1').setIndex('a', 'qsAntiBup13C_1', 3);
110             model.physics(ci(i)).feature('cfeq1').setIndex('f', 'Qbup1H_1', 0);
111             model.physics(ci(i)).feature('cfeq1').setIndex('f', 'Qbup13C_1', 1);
112             model.physics(ci(i)).feature('cfeq1').setIndex('da', 'NuEnergy1H_1', 0);
113             model.physics(ci(i)).feature('cfeq1').setIndex('da', 'NuEnergy13C_1', 3);
114             model.physics(ci(i)).feature('cfeq1').setIndex('be', '-2*kappa1H_1/x', 0);
115             model.physics(ci(i)).feature('cfeq1').setIndex('be', '-2*kappa13C_1/x', 3);
116
117             model.physics(ci(i)).feature.duplicate('cfeq2', 'cfeq1');
118             model.physics(ci(i)).feature('cfeq2').selection.set([2]);
119             model.physics(ci(i)).feature('cfeq2').setIndex('c', 'kappa1H_2', 0);
120             model.physics(ci(i)).feature('cfeq2').setIndex('c', 'kappa13C_2', 3);
121             model.physics(ci(i)).feature('cfeq2').setIndex('a', 'qsAntiBup1H_2', 0);
122             model.physics(ci(i)).feature('cfeq2').setIndex('a', 'qsAntiBup13C_2', 3);
123             model.physics(ci(i)).feature('cfeq2').setIndex('f', 'Qbup1H_2', 0);
124             model.physics(ci(i)).feature('cfeq2').setIndex('f', 'Qbup13C_2', 1);
125             model.physics(ci(i)).feature('cfeq2').setIndex('da', 'NuEnergy1H_2', 0);
126             model.physics(ci(i)).feature('cfeq2').setIndex('da', 'NuEnergy13C_2', 3);
127             model.physics(ci(i)).feature('cfeq2').setIndex('be', '-2*kappa1H_2/x', 0);
128             model.physics(ci(i)).feature('cfeq2').setIndex('be', '-2*kappa13C_2/x', 3);
129
```

108

```
130             elseif mod(i, 2) == 0
131                 % Even blocks of CP inside the sequences
132
133         model.physics(ci(i)).feature('cfeq1').setIndex('c', '0', 0);
134         model.physics(ci(i)).feature('cfeq1').setIndex('c', '0', 3);
135
136         model.physics(ci(i)).feature('cfeq1').setIndex('f', '0', 0);
137         model.physics(ci(i)).feature('cfeq1').setIndex('f', '0', 1);
138
139         model.physics(ci(i)).feature('cfeq1').setIndex('a', '+bHC_1*c13C_1/(c1H_1+c13
                C_1)+1/T1rho_1H_1', 0);
140         model.physics(ci(i)).feature('cfeq1').setIndex('a', '-bHC_1*c1H_1/(c1H_1+c13C
                _1)', 1);
141         model.physics(ci(i)).feature('cfeq1').setIndex('a', '-bHC_1*c13C_1/(c1H_1+c13
                C_1)', 2);
142         model.physics(ci(i)).feature('cfeq1').setIndex('a', '+bHC_1*c1H_1/(c1H_1+c13C
                _1)+1/T1rho_13C_1', 3);
143
144
145         model.physics(ci(i)).feature.duplicate('cfeq2', 'cfeq1');
146         model.physics(ci(i)).feature('cfeq2').selection.set([2]);
147         model.physics(ci(i)).feature('cfeq2').setIndex('a', 'bHC_2*c13C_2/(c1H_2+c13C
                _2)+1/T1rho_2H_1', 0);
148         model.physics(ci(i)).feature('cfeq2').setIndex('a', 'bHC_2*c13C_2/(c1H_2+c13C
                _2)+1/T1rho_1H_2', 0);
149         model.physics(ci(i)).feature('cfeq2').setIndex('a', '-bHC_2*c13C_2/(c1H_2+c13
                C_2)', 2);
150         model.physics(ci(i)).feature('cfeq2').setIndex('a', '-bHC_2*c1H_2/(c1H_2+c13C
                _2)', 1);
151         model.physics(ci(i)).feature('cfeq2').setIndex('a', '+bHC_2*c1H_2/(c1H_2+c13C
                _2)+1/T1rho_13C_2', 3);
152
153
154         else
155             % Last block of Relax
156
157         model.physics(ci(i)).feature('cfeq1').setIndex('c', 'kappa1H_1', 0);
158         model.physics(ci(i)).feature('cfeq1').setIndex('c', 'kappa13C_1', 3);
159         model.physics(ci(i)).feature('cfeq1').setIndex('a', 'qsRelax1H_1', 0);
160         model.physics(ci(i)).feature('cfeq1').setIndex('a', 'qsRelax13C_1', 3);
161         model.physics(ci(i)).feature('cfeq1').setIndex('f', 'Qzero1H_1', 0);
162         model.physics(ci(i)).feature('cfeq1').setIndex('f', 'Qzero13C_1', 1);
163         model.physics(ci(i)).feature('cfeq1').setIndex('da', 'NuEnergy1H_1', 0);
164         model.physics(ci(i)).feature('cfeq1').setIndex('da', 'NuEnergy13C_1', 3);
165
166         model.physics(ci(i)).feature.duplicate('cfeq2', 'cfeq1');
167         model.physics(ci(i)).feature('cfeq2').selection.set([2]);
168         model.physics(ci(i)).feature('cfeq2').setIndex('c', 'kappa1H_2', 0);
169         model.physics(ci(i)).feature('cfeq2').setIndex('c', 'kappa13C_2', 3);
170         model.physics(ci(i)).feature('cfeq2').setIndex('a', 'qsRelax1H_2', 0);
171         model.physics(ci(i)).feature('cfeq2').setIndex('a', 'qsRelax13C_2', 3);
172         model.physics(ci(i)).feature('cfeq2').setIndex('f', 'Qzero1H_2', 0);
173         model.physics(ci(i)).feature('cfeq2').setIndex('f', 'Qzero13C_2', 1);
174         model.physics(ci(i)).feature('cfeq2').setIndex('da', 'NuEnergy1H_2', 0);
175         model.physics(ci(i)).feature('cfeq2').setIndex('da', 'NuEnergy13C_2', 3);
176
177         end
178     else
179         model.physics(ci(i)).feature('cfeq1').setIndex('c', 'kappa1H_1', 0);
180         model.physics(ci(i)).feature('cfeq1').setIndex('c', 'kappa13C_1', 3);
181         model.physics(ci(i)).feature('cfeq1').setIndex('a', 'qsRelax1H_1', 0);
182         model.physics(ci(i)).feature('cfeq1').setIndex('a', 'qsRelax13C_1', 3);
183         model.physics(ci(i)).feature('cfeq1').setIndex('f', 'Qzero1H_1', 0);
184         model.physics(ci(i)).feature('cfeq1').setIndex('f', 'Qzero13C_1', 1);
185         model.physics(ci(i)).feature('cfeq1').setIndex('da', 'NuEnergy1H_1', 0);
186         model.physics(ci(i)).feature('cfeq1').setIndex('da', 'NuEnergy13C_1', 3);
187         model.physics(ci(i)).feature('cfeq1').setIndex('be', '-2*kappa1H_1/x', 0);
188         model.physics(ci(i)).feature('cfeq1').setIndex('be', '-2*kappa13C_1/x', 3);
189
190         model.physics(ci(i)).feature.duplicate('cfeq2', 'cfeq1');
191         model.physics(ci(i)).feature('cfeq2').selection.set([2]);
```

```
192
193          model.physics(ci(i)).feature('cfeq2').setIndex('c', 'kappa1H_2', 0);
194          model.physics(ci(i)).feature('cfeq2').setIndex('c', 'kappa13C_2', 3);
195          model.physics(ci(i)).feature('cfeq2').setIndex('a', 'qsRelax1H_2', 0);
196          model.physics(ci(i)).feature('cfeq2').setIndex('a', 'qsRelax13C_2', 3);
197          model.physics(ci(i)).feature('cfeq2').setIndex('f', 'Qzero1H_2', 0);
198          model.physics(ci(i)).feature('cfeq2').setIndex('f', 'Qzero13C_2', 1);
199          model.physics(ci(i)).feature('cfeq2').setIndex('da', 'NuEnergy1H_2', 0);
200          model.physics(ci(i)).feature('cfeq2').setIndex('da', 'NuEnergy13C_2', 3);
201          model.physics(ci(i)).feature('cfeq2').setIndex('be', '-2*kappa1H_2/x', 0);
202          model.physics(ci(i)).feature('cfeq2').setIndex('be', '-2*kappa13C_2/x', 3);
203      end
204  end
205
206
207
208  for i = 1:seqBlockNum
209      model.study.create(stdi(i));
210      model.study(stdi(i)).create('time', 'Transient');
211
212      for j = 1:seqBlockNum
213          cj = @(t)ci(t);
214          if j == i
215              model.study(stdi(i)).feature('time').activate(cj(j), true);
216          else
217              model.study(stdi(i)).feature('time').activate(cj(j), false);
218          end
219      end
220
221      model.sol.create(soli(i));
222      model.sol(soli(i)).study(stdi(i));
223
224      rangei= strcat('range(0,', num2str(blocSeqParam(i,1)),',',num2str(blocSeqParam(i,2))
          ,')');
225
226      if i == 1
227          model.study(stdi(i)).feature('time').set('notlistsolnum', 1);
228          model.study(stdi(i)).feature('time').set('notsolnum', '1');
229          model.study(stdi(i)).feature('time').set('listsolnum', 1);
230          model.study(stdi(i)).feature('time').set('solnum', '1');
231          model.study(stdi(i)).feature('time').set('tlist', rangei);
232          model.study(stdi(i)).feature('time').set('rtolactive', 'on');
233          model.study(stdi(i)).feature('time').set('rtol', '1e-6');
234
235      else
236          model.study(stdi(i)).feature('time').set('useinitsol', 'on');
237          model.study(stdi(i)).feature('time').set('initmethod', 'sol');
238          model.study(stdi(i)).feature('time').set('initstudy', stdi(i-1));
239          model.study(stdi(i)).feature('time').set('solnum', 'last');
240          model.study(stdi(i)).feature('time').set('usesol', 'on');
241          model.study(stdi(i)).feature('time').set('notsolmethod', 'sol');
242          model.study(stdi(i)).feature('time').set('notstudy', stdi(i-1));
243          model.study(stdi(i)).feature('time').set('notsolnum', 'last');
244          model.study(stdi(i)).feature('time').set('notlistsolnum', 1);
245          model.study(stdi(i)).feature('time').set('notsolnum', 'last');
246          model.study(stdi(i)).feature('time').set('listsolnum', 1);
247          model.study(stdi(i)).feature('time').set('solnum', 'last');
248          model.study(stdi(i)).feature('time').set('tlist', rangei);
249          model.study(stdi(i)).feature('time').set('rtolactive', 'on');
250          model.study(stdi(i)).feature('time').set('rtol', '1e-6');
251
252      end
253
254      model.sol(soli(i)).create('st1', 'StudyStep');
255      model.sol(soli(i)).feature('st1').set('study', stdi(i));
256      model.sol(soli(i)).feature('st1').set('studystep', 'time');
257      model.sol(soli(i)).create('v1', 'Variables');
258      model.sol(soli(i)).feature('v1').set('control', 'time');
259      model.sol(soli(i)).create('t1', 'Time');
260      model.sol(soli(i)).feature('t1').set('plot', 'off');
261      model.sol(soli(i)).feature('t1').set('plotgroup', 'Default');
```

110

```
262      model.sol(soli(i)).feature('t1').set('plotfreq', 'tout');
263      model.sol(soli(i)).feature('t1').set('probesel', 'all');
264      model.sol(soli(i)).feature('t1').set('probes', {});
265      model.sol(soli(i)).feature('t1').set('probefreq', 'tsteps');
266      model.sol(soli(i)).feature('t1').set('control', 'time');
267      model.sol(soli(i)).feature('t1').create('fc1', 'FullyCoupled');
268      model.sol(soli(i)).feature('t1').feature('fc1').set('linsolver', 'dDef');
269      model.sol(soli(i)).feature('t1').feature.remove('fcDef');
270      model.sol(soli(i)).attach(stdi(i));
271
272  end
273
274  for i = 1:seqBlockNum
275      model.sol(soli(i)).runAll;
276  end
277
278  for i = 1:seqBlockNum
279      model.result.create(pgi(i), 1);
280      model.result(pgi(i)).set('data', dseti(i));
281      model.result(pgi(i)).setIndex('looplevelinput', 'manualindices', 0);
282      model.result(pgi(i)).setIndex('looplevelindices', slidei(i), 0);
283      model.result(pgi(i)).create('lngr1', 'LineGraph');
284      model.result(pgi(i)).feature('lngr1').set('xdata', 'expr');
285      model.result(pgi(i)).feature('lngr1').set('xdataexpr', 'x');
286      model.result(pgi(i)).feature('lngr1').selection.all;
287      model.result(pgi(i)).feature('lngr1').set('expr', 'u1H');
288      model.result(pgi(i)).feature('lngr1').set('linecolor', 'blue');
289      model.result(pgi(i)).feature('lngr1').set('linestyle', 'cycle');
290      model.result(pgi(i)).feature.duplicate('lngr2', 'lngr1');
291      model.result(pgi(i)).feature('lngr2').set('expr', 'u13C');
292      model.result(pgi(i)).feature('lngr2').set('linestyle', 'cycle');
293      model.result(pgi(i)).feature('lngr2').set('linecolor', 'red');
294      model.result(pgi(i)).set('title', 'P1H (Blue) and P13C (Red)');
295      model.result(pgi(i)).set('xlabelactive', 'on');
296      model.result(pgi(i)).set('xlabel', 'Distance from Core (m)');
297      model.result(pgi(i)).set('ylabelactive', 'on');
298      model.result(pgi(i)).set('ylabel', 'Polarisation (%)');
299      model.result(pgi(i)).feature('lngr1').set('legend', 'on');
300      model.result(pgi(i)).feature('lngr1').set('legendmethod', 'manual');
301      model.result(pgi(i)).feature('lngr1').setIndex('legends', 'P1H, 0 s', 0);
302      model.result(pgi(i)).feature('lngr2').set('legend', 'on');
303      model.result(pgi(i)).feature('lngr2').set('legendmethod', 'manual');
304      model.result(pgi(i)).feature('lngr2').setIndex('legends', 'P13C, 0 s', 0);
305      model.result(pgi(i)).set('legendpos', 'upperleft');
306      model.result(pgi(i)).run;
307
308      figure;
309      mphplot(model,pgi(i),'rangenum',1)
310  end
311
312      exportFileDirectory = " C:\COMSOL\Output data\20170103\Raw Data\ ";
313      exportProtonFileName = ['1H-Bup-', num2str(core.radius), 'm-', num2str(core.proton.
          concentration),'M-',num2str(shell.thickness), 'm-', num2str(shell.proton.
          concentration),'M-deltaTime-150s-20170103.txt'];
314      model.result.export.create(plot1Hi(i), pgi(i), 'lngr1', 'Plot');
315      model.result.export(plot1Hi(i)).set('header', 'off');
316      model.result.export(plot1Hi(i)).set('sort', 'on');
317      model.result.export(plot1Hi(i)).set('filename', [exportFileDirectory, exportFileName
          ]);
318      model.result.export(plot1Hi(i)).run;
319      model.result.export.create(plot13Ci(i), pgi(i), 'lngr2', 'Plot');
320      model.result.export(plot13Ci(i)).set('header', 'off');
321  return
```

Run-time Sequence: PhysChemParams

```
1  % param.reference material for proton reservoir is polystyrene_ Data source: param.ref
    _[1]
2
3  param.ref_proton_concentration = 81.0*1000;%(mol)
```

Appendix A. Appendix

```
4   param.ref_proton_diffusivity = 0.38e-15;%(m^2/s)
5   param.ref_proton_energyCapacity = 5.69e-2;%(J*mol^-1)
6
7
8   % param.reference material for carbon reservoir is adamantane_ Data source: param.ref_[2]
9
10  % Admittedly, the value of 13C diffusivity in Na-Pyruvate and in Na-Acetate crystals
11  % could be calculated from the 13C spectrum and the XRD data with the method indicated in
        param.ref_[2].
12
13  param.ref_carbon_concentration = 0.872*1000;%(mol*m^-3)
14  param.ref_carbon_diffusivity = 4.617e-19;%(m^2/s)
15  param.ref_carbon_energyCapacity = 1.43e-2;%(J*mol^-1)
16
17  % param.reference average 1H-13C dipolar coupling constant is estimated from 1H-13C
        distance in XRD structure_
18  % Numerical value with better precision could be obtained from 1H-13C MAS DD Recoupling
        Experiment.
19
20  param.core_heteroDipolar = 2000;%(Hz)
21  param.shell_heteroDipolar = 9000;%(Hz)
22
23  % The scaling rule (power 1/3) comes from the ABRAGAM book for the homonuclear network of
        abundant spins. param.ref_[2]
24
25  param.core_proton_concentration = 80.0*1000;%(mol*m^-3)
26  param.core_proton_diffusivity = param.ref_proton_diffusivity * (param.core_proton_
        concentration / param.ref_proton_concentration)^(1/3);%(m^2/s)
27  param.core_proton_conductivity = param.core_proton_concentration * param.core_proton_
        diffusivity * param.ref_proton_energyCapacity;%(J*m^-1*s^-1)
28  param.core_proton_initialPolarisation = 0.0;%(1)
29  param.core_proton_bupPolarisation = 0.0;%(1) No bup exists in this phase
30  param.core_proton_eqPolarisation = 0.0;%(1)
31  param.core_proton_energyDensity = param.core_proton_concentration * param.ref_proton_
        energyCapacity;%(J*m^-3)
32  param.core_proton_Tbup = 0;%(s) No bup exists in this phase
33  param.core_proton_T1 = 6000.0;%(s)
34  param.core_proton_T1rho = 200e-3;%(s)
35  param.core_proton_bupSource = 0;%(J*m^-3*s^-1) No bup exists in this phase
36  param.core_proton_zeroSource = 0 ;%(J*m^-3*s^-1) No positive constant source during the
        storage of hyperpolarised sample
37  param.core_proton_relaxingLeak = param.core_proton_energyDensity / param.core_proton_T1;%
        (J*m^-3*s^-1)
38  param.core_proton_antiBupLeak = param.core_proton_relaxingLeak ;%(J*m^-3*s^-1) No bup
        exists in this phase
39
40  param.shell_proton_concentration = 80.0*1000;%(mol*m^-3)
41  param.shell_proton_diffusivity = param.ref_proton_diffusivity * (param.shell_proton_
        concentration / param.ref_proton_concentration)^(1/3);%(m^2/s)
42  param.shell_proton_conductivity = param.shell_proton_concentration * param.shell_proton_
        diffusivity * param.ref_proton_energyCapacity;%(J*m^-1*s^-1)
43  param.shell_proton_initialPolarisation = 0.0;%(1)
44  param.shell_proton_bupPolarisation = 0.6835;%(1)
45  param.shell_proton_eqPolarisation = 0.0;%(1)
46  param.shell_proton_energyDensity = param.shell_proton_concentration * param.ref_proton_
        energyCapacity;%(J*m^-3)
47  param.shell_proton_Tbup = 65.38;%(s)
48  param.shell_proton_T1 = 90;%(s)
49  param.shell_proton_T1rho = 10.0e-3;%(s)
50  param.shell_proton_bupSource = param.shell_proton_bupPolarisation * param.shell_proton_
        energyDensity / param.shell_proton_Tbup;%(J*m^-3*s^-1)
51  param.shell_proton_antiBupLeak = param.shell_proton_energyDensity / param.shell_proton_
        Tbup;%(J*m^-3*s^-1)
52  param.shell_proton_zeroSource = 0 ;%(J*m^-3*s^-1) No positive constant source during the
        storage of hyperpolarised sample
53  param.shell_proton_relaxingLeak = param.shell_proton_energyDensity / param.shell_proton_T
        1;%(J*m^-3*s^-1)
54
55  % The scaling rule (power 4/3) comes from the GOLDMAN paper for the proton-driven
        diffusion of inabundant spins. param.ref_[3]
56  param.core_carbon_concentration = 42.8*1000;%(mol*m^-3)
```

```
57  param.core_carbon_diffusivity = param.ref_carbon_diffusivity * (param.core_carbon_
       concentration / param.ref_carbon_concentration)^(4/3);%(m^2/s)
58  param.core_carbon_conductivity = param.core_carbon_concentration * param.core_carbon_
       diffusivity * param.ref_carbon_energyCapacity;%(J*m^-1*s^-1)
59  param.core_carbon_initialPolarisation = 0.0;%(1)
60  param.core_carbon_bupPolarisation = 0.0;%(1) No bup exists in this phase
61  param.core_carbon_eqPolarisation = 0.0;%(1)
62  param.core_carbon_energyDensity = param.core_carbon_concentration * param.ref_carbon_
       energyCapacity;%(J*m^-3)
63  param.core_carbon_T1 = 10*3600.0;%(s)
64  param.core_carbon_Tbup = 0;%(1) No bup exists in this phase
65  param.core_carbon_T1rho = 200e-3;%(s)
66  param.core_carbon_bupSource = 0;%(J*m^-3*s^-1) No bup exists in this phase
67  param.core_carbon_zeroSource = 0 ;%(J*m^-3*s^-1) No positive constant source during the
       storage of hyperpolarised sample
68  param.core_carbon_relaxingLeak = param.core_carbon_energyDensity / param.core_carbon_T1;%
       (J*m^-3*s^-1)
69  param.core_carbon_antiBupLeak = param.core_carbon_relaxingLeak;%(J*m^-3*s^-1) No bup
       exists in this phase
70  param.shell_carbon_concentration = 0.69*1000;%(mol*m^-3)
71  param.shell_carbon_diffusivity = param.ref_carbon_diffusivity * (param.shell_carbon_
       concentration / param.ref_carbon_concentration)^(4/3);%(m^2/s)
72  param.shell_carbon_conductivity = param.shell_carbon_concentration * param.shell_carbon_
       diffusivity * param.ref_carbon_energyCapacity;%(J*m^-1*s^-1)
73  param.shell_carbon_initialPolarisation = 0.0;%(1)
74  param.shell_carbon_bupPolarisation = 0.207;%(1)
75  param.shell_carbon_eqPolarisation = 0.0;%(1)
76  param.shell_carbon_energyDensity = param.shell_carbon_concentration * param.ref_carbon_
       energyCapacity;%(J*m^-3)
77  param.shell_carbon_Tbup = 1800.0;%(s)
78  param.shell_carbon_T1 = 2400.0;%(s)
79  param.shell_carbon_T1rho = 10.0e-3;%(s)
80  param.shell_carbon_bupSource = param.shell_carbon_bupPolarisation * param.shell_carbon_
       energyDensity / param.shell_carbon_Tbup;%(J*m^-3*s^-1)
81  param.shell_carbon_zeroSource = 0 ;%(J*m^-3*s^-1) No positive constant source during the
       storage of hyperpolarised sample
82  param.shell_carbon_antiBupLeak = param.shell_carbon_energyDensity / param.shell_carbon_
       Tbup;%(J*m^-3*s^-1)
83  param.shell_carbon_relaxingLeak = param.shell_carbon_energyDensity / param.shell_carbon_T
       1;%(J*m^-3*s^-1)
84
85  param.core_radius = 5e-6;%(m)
86  param.shell_thickness = 5e-6;%(m)
87
88  param.time_bup_duration = 600;%(s)
89  param.time_bup_pts = 600;
90  param.time_bup_interval = param.time_bup_duration / param.time_bup_pts;
91  param.time_CP_duration = 2e-3;%(s)
92  param.time_CP_pts = 100;
93  param.time_CP_interval  = param.time_CP_duration / param.time_CP_pts;
94  param.time_relax_duration = 3600*20;%(s)
95  param.time_relax_pts = 300;
96  param.time_relax_interval = param.time_relax_duration / param.time_relax_pts ;
```

Run-time Sequence: ParamSpec

```
1   model.param.set('Cp1H', num2str(param.ref_proton_energyCapacity), '');
2   model.param.set('c1HPS', num2str(param.ref_proton_concentration), '');
3   model.param.set('D1HPS', num2str(param.ref_proton_diffusivity), '');
4   model.param.set('c1H_1', num2str(param.core_proton_concentration), '');
5   model.param.set('D1H_1', num2str(param.core_proton_diffusivity), '');
6   model.param.set('kappa1H_1', num2str(param.core_proton_conductivity), '');
7   model.param.set('c1H_2', num2str(param.shell_proton_concentration), '');
8   model.param.set('D1H_2', num2str(param.shell_proton_diffusivity), '');
9   model.param.set('kappa1H_2', num2str(param.shell_proton_conductivity), '');
10  model.param.set('Pini1H_1', num2str(param.core_proton_initialPolarisation), '');
11  model.param.set('Pini1H_2', num2str(param.shell_proton_initialPolarisation), '');
12  model.param.set('NuEnergy1H_1', num2str(param.core_proton_energyDensity), '');
13  model.param.set('NuEnergy1H_2', num2str(param.shell_proton_energyDensity), '');
14  model.param.set('Tbup_1H_1', num2str(param.core_proton_Tbup), '');
```

Appendix A. Appendix

```
15  model.param.set('Tbup_1H_2', num2str(param.shell_proton_Tbup), '');
16  model.param.set('T1_1H_1', num2str(param.core_proton_T1), '');
17  model.param.set('T1_1H_2', num2str(param.shell_proton_T1), '');
18  model.param.set('Pbup1H_1', num2str(param.core_proton_bupPolarisation) ,'');
19  model.param.set('Pbup1H_2', num2str(param.shell_proton_bupPolarisation) ,'');
20  model.param.set('Qbup1H_1', num2str(param.core_proton_bupSource) ,'');
21  model.param.set('Qbup1H_2', num2str(param.shell_proton_bupSource) ,'');
22  model.param.set('Qzero1H_1', num2str(param.core_proton_zeroSource) ,'');
23  model.param.set('Qzero1H_2', num2str(param.shell_proton_zeroSource) ,'');
24  model.param.set('qsAntiBup1H_1', num2str(param.core_proton_antiBupLeak) ,'');
25  model.param.set('qsAntiBup1H_2', num2str(param.shell_proton_antiBupLeak) ,'');
26  model.param.set('qsRelax1H_1', num2str(param.core_proton_relaxingLeak) ,'');
27  model.param.set('qsRelax1H_2', num2str(param.shell_proton_relaxingLeak) ,'');
28  model.param.set('T1rho_1H_1', num2str(param.core_proton_T1rho), '');
29  model.param.set('T1rho_1H_2', num2str(param.shell_proton_T1rho), '');
30  model.param.set('Cp13C', num2str(param.ref_carbon_energyCapacity), '');
31  model.param.set('c13CAda', num2str(param.ref_carbon_concentration), '');
32  model.param.set('D13CAda', num2str(param.ref_carbon_diffusivity), '');
33  model.param.set('c13C_1', num2str(param.core_carbon_concentration), '');
34  model.param.set('D13C_1', num2str(param.core_carbon_diffusivity), '');
35  model.param.set('kappa13C_1', num2str(param.core_carbon_conductivity), '');
36  model.param.set('c13C_2', num2str(param.shell_carbon_concentration), '');
37  model.param.set('D13C_2', num2str(param.shell_carbon_diffusivity), '');
38  model.param.set('kappa13C_2', num2str(param.shell_carbon_conductivity), '');
39  model.param.set('Pini13C_1', num2str(param.core_carbon_initialPolarisation), '');
40  model.param.set('Pini13C_2', num2str(param.shell_carbon_initialPolarisation), '');
41  model.param.set('NuEnergy13C_1', num2str(param.core_carbon_energyDensity), '');
42  model.param.set('NuEnergy13C_2', num2str(param.shell_carbon_energyDensity), '');
43  model.param.set('T1_13C_1', num2str(param.core_carbon_T1), '');
44  model.param.set('T1_13C_2', num2str(param.shell_carbon_T1), '');
45  model.param.set('Pbup13C_1', num2str(param.core_carbon_bupPolarisation) ,'');
46  model.param.set('Pbup13C_2', num2str(param.shell_carbon_bupPolarisation) ,'');
47  model.param.set('Qbup13C_1', num2str(param.core_carbon_bupSource) ,'');
48  model.param.set('Qbup13C_2', num2str(param.shell_carbon_bupSource) ,'');
49  model.param.set('Qzero13C_1', num2str(param.core_carbon_zeroSource) ,'');
50  model.param.set('Qzero13C_2', num2str(param.shell_carbon_zeroSource) ,'');
51  model.param.set('qsAntiBup13C_1', num2str(param.core_carbon_antiBupLeak) ,'');
52  model.param.set('qsAntiBup13C_2', num2str(param.shell_carbon_antiBupLeak) ,'');
53  model.param.set('qsRelax13C_1', num2str(param.core_carbon_relaxingLeak) ,'');
54  model.param.set('qsRelax13C_2', num2str(param.shell_carbon_relaxingLeak) ,'');
55  model.param.set('T1rho_13C_1', num2str(param.core_carbon_T1rho), '');
56  model.param.set('T1rho_13C_2', num2str(param.shell_carbon_T1rho), '');
57  model.param.set('bHC_1', num2str(param.core_heteroDipolar ), '');
58  model.param.set('bHC_2', num2str(param.shell_heteroDipolar ), '');
59  model.param.set('r_core', num2str(param.core_radius), '');
60  model.param.set('r_shell', num2str(param.shell_thickness), '');
```

Function: str4IterGen

```
1  function y = str4IterGen(parStr, parNum)
2      % inline func to assign COMSOL_JAVA keywords
3      y = strcat(parStr, num2str(parNum));
4  end
```

Lambda Functions: iterStrFunc

```
1  stdi =    @(t)str4IterGen('std',t);
2  ci =   @(t)str4IterGen('c',t);
3  soli =   @(t)str4IterGen('sol',t);
4  pgi = @(t) str4IterGen('pg',t);
5  dseti = @(t) str4IterGen('dset',t);
6  tbli = @(t) str4IterGen('tbl', t);
7  plot1Hi = @(t) str4IterGen('plot1H-', t);
8  plot13Ci = @(t) str4IterGen('plot13C-', t);
```

Function: numofBlocks

114

```
1   function y = numofBlocks(x)
2       % Calculate the number of total blocks basing on the number of CP blocks
3       % ONLY take Integer as input
4       % When takeing -1 as param, means only one bup
5       % when takeing 0 as param, means one bup and one relaxation
6       % when takeing n as positive intergers, means n times bup-CP blocks
7
8       if x>0 & mod(x,1) == 0
9           y = 2*x+1;
10      elseif x == 0
11          y = 2;
12      elseif x == -1
13          y = 1;
14      else
15          error ('<numofCP> must be a positive integer or -1')
16          return
17      end
18  end
```

Function: seqGen

```
1   function seq = seqGen(x)
2       % Generate the array of information in time domain for the simulation.
3
4       param = evalin('base', 'param');
5       % get time params from the base workspace
6       if isempty(param)
7           error ('parameter must be a positive integer greater than 1')
8       else
9           if x < 1
10              error ('parameter must be a positive integer greater than 0')
11              return
12          elseif x == 1
13              seq = zeros(x, 2);
14              seq(1,2) = param.time_bup_duration;
15              seq(1,1) = param.time_bup_interval;
16
17          elseif x == 2
18              seq = zeros(x, 2);
19              seq(1,2) = param.time_bup_duration;
20              seq(1,1) = param.time_bup_interval;
21              seq(2,2) = param.time_relax_duration;
22              seq(2,1) = param.time_relax_interval;
23          else
24              seq = zeros(x, 2);
25
26              for i = 1 : x
27                  if mod(i, 2) == 1 & i < x
28                      seq(i,2) = param.time_bup_duration;
29                      seq(i,1) = param.time_bup_interval;
30                  elseif mod(i, 2) == 0
31                      seq(i,2) = param.time_CP_duration;
32                      seq(i,1) = param.time_CP_interval;
33                  else
34                      seq(i,2) = param.time_relax_duration;
35                      seq(i,1) = param.time_relax_interval;
36                  end
37              end
38          end
39      end
40  end
```

A.2 Supplementary information on the preparation of biphasic sample

A.2.1 Preparing micro-particulate RFP

A typical protocol of micro-particulate RFP follows here:

20 mg of sodium $[1-^{13}C]$ pyruvate is placed in an mortar made of agate. Before starting hand-grinding, 100 uL of toluene is introduced in the mortar in view of smoothing the friction for more homogenised distribution of particle size. Upon complete evaporation of solvent, another 100 uL of solvent is reintroduced. The occasional addition of milling liquid lasts along the whole process of 5-minute long hand-milling.

A.2.2 Manual counting for the distribution of particle size

The statistics of the distribution of particle number with respect to the surface-equivalent diameter of particles of hand-ground sodium $[1-^{13}C]$pyruvate is obtained from the software ImageJ.

Since the image is dense in overlapped particles, the whole process was conducted as a manual repetition of particle picking and pixel counting on the SEM image.

The distribution of particle size in terms of particle volume is calculated basing on the distribution of particle number .

A.3 Supplementary information on the synthesis of porous polarising matrix

A.3.1 Chemicals and Materials

Styrene (Sty, Sigma-Aldrich, Analytical Grade, 99%), divinylbenzene (DVB, Sigma-Aldrich, 80% DVB + 20% Ethylvinylbenzene(EVB)), 4-Vinylbenzyl chloride / 1-(chloromethyl)-4-vinylbenzene (VBC, Sigma-Aldrich, Mixture of 3- and 4-isomers, 97%), and 2-ethylhexylacrylate (EHA, Sigma-Aldrich, 98%) were purified by column of basic alumina (Al_2O_3, Sigma-Aldrich) to remove the inhibitors before synthesis. Potassium persulfate ($K_2S_2O_8$), calcium chloride hexahydrate ($CaCl_2 \cdot H_2O$), sorbitan monooleate (Span 80, Sigma-Aldrich), sodium 4-vinylbenzenesulfinate (NaVBS) and di-tert-butyl peroxide (DTBP, Sigma-Aldrich) were used as receved. Tetrahydrofurane (THF, Sigma-Aldrich) passed through the peroxide test (with potassium iodide / starch paper) and distilled upon usage. Toluene was also distilled upon usage.

The quantities of starting materials are listed in the following tables:

Table A.4 – Chemical composition of aqueous initiator solution

Chemical	m (g)	V (mL)	n (mmol)
$K_2S_2O_8$	0.11	-	0.407
$CaCl_2 \cdot H_2O$	1.78	-	8.13
H_2O	-	100	5556

Table A.5 – Characteristic parameters of monomers of polymers discussed in this chapter

	NaVBS (mol %)	Sty (mol %)	DVB+EVB (mol %)	VBC (mol %)	EHA (mol %)	Porosity (%)	Radical Concentration mmol·L^{-1}
PM-01	7.5	2.0	90	0.5	0	80	25
PM-02	7.5	0	30	0.6	61.9	80	25
PM-03	7.5	0	30	0.6	61.9	66	25

A.3.2 Protocol of a typical synthesis

1. All the ionic initiator (potassium persulfate), and the stabiliser (calcium, chloride) were solubilised in deionised degassed water so as to form the aqueous solution of initiator. Detailed composition see table A.4. Then dissolve the hydrophilic mono-mer(NaVBS) in this solution under protective atmosphere.

2. The surfactant and the hydrophobic monomers (Sty, DVB+EVB, VBC, and EHA) were placed in a reactor (10 mL capped glass vial equipped with a magnetic bar) and the mixture was stirred (300 rpm) for 10 min under protective atmosphere.

3. The aqueous solution (4 times the volume of the oil-phase) was then added drop-wise to the oil-phase under continuous stirring under atmosphere. The obtained emulsion was then sealed and further vigorously stirred for 60 min to yield a viscous uniform W/O HIPE.

4. The HIPE is then transferred into 6 mm diameter glass tubes (around 1 to 1.5 cm high column) which there capped and inserted in a preheated oil bath (60 °C) and further maintained for 24 h.

5. The resulting bulk polymer was then recovered and successively washed by solid/li-quid extraction in a Soxhlet apparatus with H_2O (150 mL, 24 h) and then with ethanol (150 mL, 24 h). The clean polymer monolith was then dried under high vacuum at room temperature for 72 h.

6. The purified polymer monolith was suspended in dry toluene (20 mL/g of polymer), then di-t-Bu-peroxide (130 μL/g of polymer) was added and the mixture was heated at reflux under N2 for 24 h (secondary polymerisation).

7. The isolated polymer was washed with THF (3 x 50 mL), then dried under high vacuum at room temperature for 72 h.

8. The polymer bulk yielded after the secondary polymerisation was then immersed in a solution of amino-TEMPO (10 eq. with respect to vinylbenzyl chloride) in THF (20 mL) and maintained for 1 week at room temperature in the dark. Then the polymer monolith is washed by fresh THF (3 x 50 mL), immersed in deionised water over night, and washed by solution of ascorbate (1 mol·L^{-1})* before drying under high vacuum at room temperature for 72 h.

A.3.3 Protocol of scanning electronic microscopy (SEM)

SEM was performed with a FEI XLF-30 SEM instrument at 10 kV accelerating voltage. An amount of 10 mg of finely ground RFP was placed on a film of conducting polymer attached to the sample holder. The sample was coated with 25nm gold to ensure surface conductivity.

---

*This step aimes at complete quenching of the residual of TEMPO on the surface of matrix. It is optional

Bibliography

[1] Albert W Overhauser. Polarization of nuclei in metals. *Physical Review*, 92(2):411, 1953.

[2] TR Carver and CP Slichter. Polarization of nuclear spins in metals. *Physical Review*, 92(1):212, 1953.

[3] Thomas R Carver and Charles P Slichter. Experimental verification of the overhauser nuclear polarization effect. *Physical Review*, 102(4):975, 1956.

[4] Albert W. Overhauser. Paramagnetic relaxation in metals. *Phys. Rev.*, 89:689–700, Feb 1953.

[5] Lino R. Becerra, Gary J. Gerfen, Richard J. Temkin, David J. Singel, and Robert G. Griffin. Dynamic nuclear polarization with a cyclotron resonance maser at 5 t. *Phys. Rev. Lett.*, 71:3561–3564, Nov 1993.

[6] Melanie Rosay, Ana-Carolina Zeri, Nathan S Astrof, Stanley J Opella, Judith Herzfeld, and Robert G Griffin. Sensitivity-enhanced NMR of biological solids: Dynamic nuclear polarization of y21m fd bacteriophage and purple membrane. *Journal of the American Chemical Society*, 123(5):1010–1011, 2001.

[7] Patrick CA van der Wel, Kan-Nian Hu, Józef Lewandowski, and Robert G Griffin. Dynamic nuclear polarization of amyloidogenic peptide nanocrystals: GNNQQNY, a core segment of the yeast prion protein sup35p. *Journal of the American Chemical Society*, 128(33):10840–10846, 2006.

[8] Melody L Mak-Jurkauskas, Vikram S Bajaj, Melissa K Hornstein, Marina Belenky, Robert G Griffin, and Judith Herzfeld. Energy transformations early in the bacteriorhodopsin photocycle revealed by DNP-enhanced solid-state nmr. *Proceedings of the National Academy of Sciences*, 105(3):883–888, 2008.

[9] Michael T Colvin, Robert Silvers, Qing Zhe Ni, Thach V Can, Ivan Sergeyev, Melanie Rosay, Kevin J Donovan, Brian Michael, Joseph Wall, Sara Linse, et al. Atomic resolution structure of monomorphic aβ42 amyloid fibrils. *Journal of the American Chemical Society*, 138(30):9663–9674, 2016.

[10] Anne Lesage, Moreno Lelli, David Gajan, Marc A Caporini, Veronika Vitzthum, Pascal Miéville, Johan Alauzun, Arthur Roussey, Chloé Thieuleux, Ahmad Mehdi, et al. Surface enhanced nmr spectroscopy by dynamic nuclear polarization. *Journal of the American Chemical Society*, 132(44):15459–15461, 2010.

Bibliography

[11] Moreno Lelli, David Gajan, Anne Lesage, Marc A Caporini, Veronika Vitzthum, Pascal Miéville, Florent Héroguel, Fernando Rascón, Arthur Roussey, Chloé Thieuleux, et al. Fast characterization of functionalized silica materials by silicon-29 surface-enhanced nmr spectroscopy using dynamic nuclear polarization. *Journal of the American Chemical Society*, 133(7):2104–2107, 2011.

[12] Aaron J Rossini, Alexandre Zagdoun, Moreno Lelli, David Gajan, Fernando Rascón, Melanie Rosay, Werner E Maas, Christophe Copéret, Anne Lesage, and Lyndon Emsley. One hundred fold overall sensitivity enhancements for silicon-29 nmr spectroscopy of surfaces by dynamic nuclear polarization with cpmg acquisition. *Chemical Science*, 3(1):108–115, 2012.

[13] Alexandre Zagdoun, Aaron J Rossini, David Gajan, Adrien Bourdolle, Olivier Ouari, Melanie Rosay, Werner E Maas, Paul Tordo, Moreno Lelli, Lyndon Emsley, et al. Non-aqueous solvents for dnp surface enhanced nmr spectroscopy. *Chemical Communications*, 48(5):654–656, 2012.

[14] Veronika Vitzthum, Pascal Miéville, Diego Carnevale, Marc A Caporini, David Gajan, Christophe Copéret, Moreno Lelli, Alexandre Zagdoun, Aaron J Rossini, Anne Lesage, et al. Dynamic nuclear polarization of quadrupolar nuclei using cross polarization from protons: surface-enhanced aluminium-27 nmr. *Chemical Communications*, 48(14):1988–1990, 2012.

[15] Aaron J Rossini, Alexandre Zagdoun, Moreno Lelli, Anne Lesage, Christophe Coperet, and Lyndon Emsley. Dynamic nuclear polarization surface enhanced nmr spectroscopy. *Accounts of chemical research*, 46(9):1942–1951, 2013.

[16] Patrick Wolf, Maxence Valla, Aaron J Rossini, Aleix Comas-Vives, Francisco Núñez-Zarur, Bernard Malaman, Anne Lesage, Lyndon Emsley, Christophe Copéret, and Ive Hermans. Nmr signatures of the active sites in sn-β zeolite. *Angewandte Chemie International Edition*, 53(38):10179–10183, 2014.

[17] Ta-Chung Ong, Wei-Chih Liao, Victor Mougel, David Gajan, Anne Lesage, Lyndon Emsley, and Christophe Copéret. Atomistic description of reaction intermediates for supported metathesis catalysts enabled by dnp sens. *Angewandte Chemie International Edition*, 55(15):4743–4747, 2016.

[18] Pierrick Berruyer, Moreno Lelli, Matthew P Conley, Daniel L Silverio, Cory M Widdifield, Georges Siddiqi, David Gajan, Anne Lesage, Christophe Copéret, and Lyndon Emsley. Three-dimensional structure determination of surface sites. *Journal of the American Chemical Society*, 2017.

[19] Frédéric Blanc, Luke Sperrin, David A Jefferson, Shane Pawsey, Melanie Rosay, and Clare P Grey. Dynamic nuclear polarization enhanced natural abundance 17o spectroscopy. *Journal of the American Chemical Society*, 135(8):2975–2978, 2013.

[20] Maxence Valla, Aaron J Rossini, Maxime Caillot, Céline Chizallet, Pascal Raybaud, Mathieu Digne, Alexandra Chaumonnot, Anne Lesage, Lyndon Emsley, Jeroen A Van Bokhoven, et al. Atomic description of the interface between silica and alumina in aluminosilicates through dynamic nuclear polarization surface-enhanced nmr spectroscopy and first-principles calculations. *Journal of the American Chemical Society*, 137(33):10710–10719, 2015.

[21] Laura Piveteau, Ta-Chung Ong, Aaron J Rossini, Lyndon Emsley, Christophe Coperet, and Maksym V Kovalenko. Structure of colloidal quantum dots from dynamic nuclear polarization surface enhanced nmr spectroscopy. *Journal of the American Chemical Society*, 137(43):13964–13971, 2015.

[22] Aaron J Rossini, Cory M Widdifield, Alexandre Zagdoun, Moreno Lelli, Martin Schwarzwälder, Christophe Coperet, Anne Lesage, and Lyndon Emsley. Dynamic nuclear polarization enhanced nmr spectroscopy for pharmaceutical formulations. *Journal of the American Chemical Society*, 136(6):2324–2334, 2014.

[23] Arthur C Pinon, Aaron J Rossini, Cory M Widdifield, David Gajan, and Lyndon Emsley. Polymorphs of theophylline characterized by dnp enhanced solid-state nmr. *Molecular pharmaceutics*, 12(11):4146–4153, 2015.

[24] Jan H Ardenkjær-Larsen, Björn Fridlund, Andreas Gram, Georg Hansson, Lennart Hansson, Mathilde H Lerche, Rolf Servin, Mikkel Thaning, and Klaes Golman. Increase in signal-to-noise ratio of> 10,000 times in liquid-state nmr. *Proceedings of the National Academy of Sciences*, 100(18):10158–10163, 2003.

[25] J Wolber, F Ellner, B Fridlund, A Gram, H Johannesson, G Hansson, LH Hansson, MH Lerche, Sven Månsson, R Servin, et al. Generating highly polarized nuclear spins in solution using dynamic nuclear polarization. *Nuclear Instruments and Methods in Physics Research Section A: Accelerators, Spectrometers, Detectors and Associated Equipment*, 526(1):173–181, 2004.

[26] Klaes Golman, Jan H Ardenkjær-Larsen, J Stefan Petersson, Sven Månsson, and Ib Leunbach. Molecular imaging with endogenous substances. *Proceedings of the National Academy of Sciences*, 100(18):10435–10439, 2003.

[27] Ferdia A Gallagher, Mikko I Kettunen, Sam E Day, De-En Hu, Jan Henrik Ardenkjær-Larsen, Pernille R Jensen, Magnus Karlsson, Klaes Golman, Mathilde H Lerche, Kevin M Brindle, et al. Magnetic resonance imaging of ph in vivo using hyperpolarized 13c-labelled bicarbonate. *Nature*, 453(7197):940–943, 2008.

[28] Lucio Frydman and Damir Blazina. Ultrafast two-dimensional nuclear magnetic resonance spectroscopy of hyperpolarized solutions. *Nature physics*, 3(6):415–419, 2007.

[29] Mathilde H Lerche, Sebastian Meier, Pernille R Jensen, Svein-Olaf Hustvedt, Magnus Karlsson, Jens Ø Duus, and Jan H Ardenkjær-Larsen. Quantitative dynamic nuclear polarization-nmr on blood plasma for assays of drug metabolism. *NMR in Biomedicine*, 24(1):96–103, 2011.

[30] Marina Carravetta, Ole G Johannessen, and Malcolm H Levitt. Beyond the t 1 limit: singlet nuclear spin states in low magnetic fields. *Physical review letters*, 92(15):153003, 2004.

[31] Pascal Miéville, Sami Jannin, Lothar Helm, and Geoffrey Bodenhausen. Nmr of insensitive nuclei enhanced by dynamic nuclear polarization. *Chimia-International Journal for Chemistry*, 65(4):260, 2011.

[32] Aaron J Rossini, Alexandre Zagdoun, Franziska Hegner, Martin Schwarzwalder, David Gajan, Christophe Copéret, Anne Lesage, and Lyndon Emsley. Dynamic nuclear polarization nmr spectroscopy of microcrystalline solids. *Journal of the American Chemical Society*, 134(40):16899–16908, 2012.

Bibliography

[33] Anatole Abragam. *The principles of nuclear magnetism.* Oxford university press, 1961.

[34] Maurice Goldman. *Spin temperature and nuclear magnetic resonance in solids.* Clarendon Press Oxford, 1970.

[35] Charles P Slichter. *Principles of magnetic resonance*, volume 1. Springer Science & Business Media, 1996.

[36] Malcolm H Levitt. *Spin dynamics: basics of nuclear magnetic resonance.* John Wiley & Sons, 2001.

[37] Melinda J Duer. *Solid state NMR spectroscopy: principles and applications.* John Wiley & Sons, 2008.

[38] James Keeler. *Understanding NMR spectroscopy.* John Wiley & Sons, 2011.

[39] HBG Casimir and FK Du Pré. Note on the thermodynamic interpretation of paramagnetic relaxation phenomena. *Physica*, 5(6):507–511, 1938.

[40] Alfred G. Redfield. Nuclear magnetic resonance saturation and rotary saturation in solids. *Phys. Rev.*, 98:1787–1809, Jun 1955.

[41] Ta-Chung Ong, Melody L Mak-Jurkauskas, Joseph J Walish, Vladimir K Michaelis, Björn Corzilius, Albert A Smith, Andrew M Clausen, Janet C Cheetham, Timothy M Swager, and Robert G Griffin. Solvent-free dynamic nuclear polarization of amorphous and crystalline ortho-terphenyl. *The Journal of Physical Chemistry B*, 117(10):3040–3046, 2013.

[42] Veronika Vitzthum, Françoise Borcard, Sami Jannin, Mylène Morin, Pascal Miéville, Marc A Caporini, Andrzej Sienkiewicz, Sandrine Gerber-Lemaire, and Geoffrey Bodenhausen. Fractional spin-labeling of polymers for enhancing nmr sensitivity by solvent-free dynamic nuclear polarization. *ChemPhysChem*, 12(16):2929–2932, 2011.

[43] Aany Sofia Lilly Thankamony, Olivier Lafon, Xingyu Lu, Fabien Aussenac, Melanie Rosay, Julien Trébosc, Hervé Vezin, and Jean-Paul Amoureux. Solvent-free high-field dynamic nuclear polarization of mesoporous silica functionalized with tempo. *Applied Magnetic Resonance*, 43(1-2):237–250, 2012.

[44] B Van den Brandt, EI Bunyatova, P Hautle, JA Konter, and S Mango. Dynamic nuclear polarization in thin polymer foils and tubes. *Nuclear Instruments and Methods in Physics Research Section A: Accelerators, Spectrometers, Detectors and Associated Equipment*, 356(1):36–38, 1995.

[45] Magnus Karlsson, Pernille R Jensen, Jens Ø Duus, Sebastian Meier, and Mathilde H Lerche. Development of dissolution dnp-mr substrates for metabolic research. *Applied Magnetic Resonance*, 43(1-2):223–236, 2012.

[46] D Hill and M Krumpolc. Dynamic polarization in some high-hydrogen glasses. Technical report, Argonne National Lab., IL (USA); Illinois Univ., Chicago (USA), 1982.

[47] EI Bunyatova. New investigations of organic compounds for targets with polarized hydrogen nuclei. *Nuclear Instruments and Methods in Physics Research Section A: Accelerators, Spectrometers, Detectors and Associated Equipment*, 356(1):29–33, 1995.

[48] E Elisei, M Filibian, P Carretta, S Colombo Serra, F Tedoldi, JF Willart, M Descamps, and A Cesàro. Dynamic nuclear polarization of a glassy matrix prepared by solid state mechanochemical amorphization of crystalline substances. *Chemical Communications*, 51(11):2080–2083, 2015.

[49] Klaes Golman, Mikkel Thaning, et al. Real-time metabolic imaging. *Proceedings of the National Academy of Sciences*, 103(30):11270–11275, 2006.

[50] Sven Macholl, Haukur Jóhannesson, and Jan Henrik Ardenkjaer-Larsen. Trityl biradicals and 13c dynamic nuclear polarization. *Physical Chemistry Chemical Physics*, 12(22):5804–5817, 2010.

[51] Sami Jannin, Aurélien Bornet, Sonia Colombo, and Geoffrey Bodenhausen. Low-temperature cross polarization in view of enhancing dissolution dynamic nuclear polarization in nmr. *Chemical Physics Letters*, 517(4):234–236, 2011.

[52] Aurélien Bornet, Roberto Melzi, Angel J Perez Linde, Patrick Hautle, Ben van den Brandt, Sami Jannin, and Geoffrey Bodenhausen. Boosting dissolution dynamic nuclear polarization by cross polarization. *The journal of physical chemistry letters*, 4(1):111–114, 2012.

[53] Sami Jannin, Aurélien Bornet, Roberto Melzi, and Geoffrey Bodenhausen. High field dynamic nuclear polarization at 6.7 t: Carbon-13 polarization above 70% within 20min. *Chemical Physics Letters*, 549:99–102, 2012.

[54] Aurélien Bornet, Roberto Melzi, Sami Jannin, and Geoffrey Bodenhausen. Cross polarization for dissolution dynamic nuclear polarization experiments at readily accessible temperatures 1.2< t< 4.2 k. *Applied Magnetic Resonance*, 43(1-2):107–117, 2012.

[55] Angel J Perez Linde, Aurélien Bornet, Jonas Milani, Basile Vuichoud, Roberto Melzi, Sami Jannin, and Geoffrey Bodenhausen. Cross polarization from 1 h to quadrupolar 6 li nuclei for dissolution dnp. *Physical Chemistry Chemical Physics*, 16(45):24813–24817, 2014.

[56] Basile Vuichoud, Jonas Milani, Aurélien Bornet, Roberto Melzi, Sami Jannin, and Geoffrey Bodenhausen. Hyperpolarization of deuterated metabolites via remote cross-polarization and dissolution dynamic nuclear polarization. *The Journal of Physical Chemistry B*, 118(5):1411–1415, 2014.

[57] Jonas Milani, Basile Vuichoud, Aurélien Bornet, Pascal Miéville, Roger Mottier, Sami Jannin, and Geoffrey Bodenhausen. A magnetic tunnel to shelter hyperpolarized fluids. *Review of Scientific Instruments*, 86(2):024101, 2015.

[58] Jean-Nicolas Dumez, Jonas Milani, Basile Vuichoud, Aurélien Bornet, Julie Lalande-Martin, Illa Tea, Maxime Yon, Mickaël Maucourt, Catherine Deborde, Annick Moing, et al. Hyperpolarized nmr of plant and cancer cell extracts at natural abundance. *Analyst*, 140(17):5860–5863, 2015.

[59] Aurélien Bornet, Mickaël Maucourt, Catherine Deborde, Daniel Jacob, Jonas Milani, Basile Vuichoud, Xiao Ji, Jean-Nicolas Dumez, Annick Moing, Geoffrey Bodenhausen, et al. Highly repeatable dissolution dynamic nuclear polarization for heteronuclear nmr metabolomics. *Analytical chemistry*, 2016.

Bibliography

[60] Aurélien Bornet, Xiao Ji, Daniele Mammoli, Basile Vuichoud, Jonas Milani, Geoffrey Bodenhausen, and Sami Jannin. Long-lived states of magnetically equivalent spins populated by dissolution-dnp and revealed by enzymatic reactions. *Chemistry–A European Journal*, 20(51):17113–17118, 2014.

[61] Emeric Miclet, Daniel Abergel, Aurélien Bornet, Jonas Milani, Sami Jannin, and Geoffrey Bodenhausen. Toward quantitative measurements of enzyme kinetics by dissolution dynamic nuclear polarization. *The journal of physical chemistry letters*, 5(19):3290–3295, 2014.

[62] Roberto Buratto, Aurélien Bornet, Jonas Milani, Daniele Mammoli, Basile Vuichoud, Nicola Salvi, Maninder Singh, Aurélien Laguerre, Solène Passemard, Sandrine Gerber-Lemaire, et al. Drug screening boosted by hyperpolarized long-lived states in nmr. *ChemMedChem*, 9(11):2509–2515, 2014.

[63] Quentin Chappuis, Jonas Milani, Basile Vuichoud, Aurélien Bornet, Alvar D Gossert, Geoffrey Bodenhausen, and Sami Jannin. Hyperpolarized water to study protein–ligand interactions. *The journal of physical chemistry letters*, 6(9):1674–1678, 2015.

[64] Ferdia A Gallagher, Mikko I Kettunen, De-En Hu, Pernille R Jensen, Magnus Karlsson, Anna Gisselsson, Sarah K Nelson, Timothy H Witney, Sarah E Bohndiek, Georg Hansson, et al. Production of hyperpolarized $[1, 4-^{13}c_2]$ malate from $[1, 4-^{13}c_2]$ fumarate is a marker of cell necrosis and treatment response in tumors. *Proceedings of the National Academy of Sciences*, 106(47):19801–19806, 2009.

[65] Magnus Karlsson, Pernille R Jensen, Anna Gisselsson, Georg Hansson, Jens Ø Duus, Sebastian Meier, Mathilde H Lerche, et al. Imaging of branched chain amino acid metabolism in tumors with hyperpolarized 13c ketoisocaproate. *International journal of cancer*, 127(3):729–736, 2010.

[66] Klaes Golman, Mathilde Lerche, Rikard Pehrson, Jan Henrik Ardenkjaer-Larsen, et al. Metabolic imaging by hyperpolarized 13c magnetic resonance imaging for in vivo tumor diagnosis. *Cancer research*, 66(22):10855–10860, 2006.

[67] Pernille R Jensen, Torben Peitersen, Magnus Karlsson, Anna Gisselsson, Georg Hansson, Sebastian Meier, Mathilde H Lerche, et al. Tissue-specific short chain fatty acid metabolism and slow metabolic recovery after ischemia from hyperpolarized nmr in vivo. *Journal of Biological Chemistry*, 284(52):36077–36082, 2009.

[68] AG Redfield. Spatial diffusion of spin energy. *Physical Review*, 116(2):315, 1959.

[69] Alfred G Redfield and WN Yu. Moment-method calculation of magnetization and interspin-energy diffusion. *Physical Review*, 169(2):443, 1968.

[70] IJ Lowe and S Gade. Density-matrix derivation of the spin-diffusion equation. *Physical Review*, 156(3):817, 1967.

[71] Jerome I Kaplan. Modified linear-response method for obtaining the spin-diffusion constant of a rigid dipole system. *Physical Review B*, 2(11):4578, 1970.

[72] Dieter Suter and RR Ernst. Spin diffusion in resolved solid-state nmr spectra. *Physical Review B*, 32(9):5608, 1985.

[73] Nicolaas Bloembergen. On the interaction of nuclear spins in a crystalline lattice. *Physica*, 15(3):386–426, 1949.

[74] IM Nolden and RJ Silbey. Simulation of spin diffusion in a disordered system. *Physical Review B*, 54(1):381, 1996.

[75] Yonatan Hovav, Akiva Feintuch, and Shimon Vega. Dynamic nuclear polarization assisted spin diffusion for the solid effect case. *The Journal of chemical physics*, 134(7):074509, 2011.

[76] Mark C Butler, Jean-Nicolas Dumez, and Lyndon Emsley. Dynamics of large nuclear-spin systems from low-order correlations in liouville space. *Chemical Physics Letters*, 477(4):377–381, 2009.

[77] Jean-Nicolas Dumez, Mark C Butler, Elodie Salager, Bénédicte Elena-Herrmann, and Lyndon Emsley. Ab initio simulation of proton spin diffusion. *Physical Chemistry Chemical Physics*, 12(32):9172–9175, 2010.

[78] Jean-Nicolas Dumez and Lyndon Emsley. A master-equation approach to the description of proton-driven spin diffusion from crystal geometry using simulated zero-quantum lineshapes. *Physical Chemistry Chemical Physics*, 13(16):7363–7370, 2011.

[79] Jean-Nicolas Dumez, Meghan E Halse, Mark C Butler, and Lyndon Emsley. A first-principles description of proton-driven spin diffusion. *Physical Chemistry Chemical Physics*, 14(1):86–89, 2012.

[80] Meghan E Halse, Alexandre Zagdoun, Jean-Nicolas Dumez, and Lyndon Emsley. Macroscopic nuclear spin diffusion constants of rotating polycrystalline solids from first-principles simulation. *Journal of Magnetic Resonance*, 254:48–55, 2015.

[81] Mikhail Veshtort and Robert G Griffin. Proton-driven spin diffusion in rotating solids via reversible and irreversible quantum dynamics. *The Journal of chemical physics*, 135(13):10B606, 2011.

[82] D Greenbaum, M Kindermann, C Ramanathan, and DG Cory. Hydrodynamic approach to coherent nuclear-spin transport. *Physical Review B*, 71(5):054403, 2005.

[83] Tom Wenckebach. *Essentials of Dynamic Nuclear Polarization*. Spindrift Publications, 2016.

[84] Henriette W Meyer, Horst Schneider, and Kay Saalwächter. Proton nmr spin-diffusion studies of ps-pb block copolymers at low field: two-vs three-phase model and recalibration of spin-diffusion coefficients. *Polymer journal*, 44(8):748–756, 2012.

[85] Shinji Ando, Robin K Harris, and Stefan A Reinsberg. Analysis of cross-polarization dynamics between two abundant nuclei, 19 f and 1 h, based on spin thermodynamics theory. *Journal of Magnetic Resonance*, 141(1):91–103, 1999.

[86] Wurong Zhang and DG Cory. First direct measurement of the spin diffusion rate in a homogenous solid. *Physical review letters*, 80(6):1324, 1998.

[87] GB Furman, SD Goren, AM Panich, AI Shames, and T Nakajima. Spin diffusion in multiple pulse spin-locking in solids containing paramagnetic impurities. *Solid state nuclear magnetic resonance*, 38(4):84–89, 2010.

Bibliography

[88] GR Khutsishvili. Spin diffusion. *Soviet Physics Uspekhi*, 8(5):743, 1966.

[89] Charles E Bronniman, Nikolaus M Szeverenyi, and Gary E Maciel. 13c spin diffusion of adamantane. *The Journal of chemical physics*, 79(8):3694–3700, 1983.

[90] Louis A Girifalco. *Statistical mechanics of solids*, volume 58. OUP USA, 2003.

[91] M Goldman and JF Jacquinot. Nuclear spin diffusion in a rare spin species. *Journal de Physique*, 43(7):1049–1058, 1982.

[92] Aurélien Bornet, Arthur Pinon, Aditya Jhajharia, Mathieu Baudin, Xiao Ji, Lyndon Emsley, Geoffrey Bodenhausen, Jan Henrik Ardenkjaer-Larsen, and Sami Jannin. Microwave-gated dynamic nuclear polarization. *Physical Chemistry Chemical Physics*, 18(44):30530–30535, 2016.

[93] N Bloembergen and LO Morgan. Proton relaxation times in paramagnetic solutions. effects of electron spin relaxation. *The Journal of Chemical Physics*, 34(3):842–850, 1961.

[94] I Solomon. Relaxation processes in a system of two spins. *Physical Review*, 99(2):559, 1955.

[95] Xiao Ji, Aurélien Bornet, Basile Vuichoud, Jonas Milani, David Gajan, Aaron J Rossini, Lyndon Emsley, Geoffrey Bodenhausen, and Sami Jannin. Transportable hyperpolarized metabolites. *Nature Communications*, 8:13975, 2017.

[96] Aurélien Bornet and Sami Jannin. Optimizing dissolution dynamic nuclear polarization. *Journal of Magnetic Resonance*, 264:13–21, 2016.

[97] Matthew L Hirsch, Neal Kalechofsky, Avrum Belzer, Melanie Rosay, and James G Kempf. Brute-force hyperpolarization for nmr and mri. *Journal of the American Chemical Society*, 137(26):8428–8434, 2015.

[98] Matthew L Hirsch, Bryce A Smith, Mark Mattingly, Artem G Goloshevsky, Melanie Rosay, and James G Kempf. Transport and imaging of brute-force 13 c hyperpolarization. *Journal of Magnetic Resonance*, 261:87–94, 2015.

[99] A Abragam and WG Proctor. Spin temperature. *Physical Review*, 109(5):1441, 1958.

[100] A Abragam and WG Proctor. Experiments on spin temperature. *Physical Review*, 106(1):160, 1957.

[101] David T Peat, Matthew L Hirsch, David G Gadian, Anthony J Horsewill, John R Owers-Bradley, and James G Kempf. Low-field thermal mixing in [1-13c] pyruvic acid for brute-force hyperpolarization. *Physical Chemistry Chemical Physics*, 18(28):19173–19182, 2016.

[102] A Comment, B vd van den Brandt, K Uffmann, F Kurdzesau, S Jannin, JA Konter, P Hautle, W Th Wenckebach, R Gruetter, and JJ Van Der Klink. Design and performance of a dnp prepolarizer coupled to a rodent mri scanner. *Concepts in Magnetic Resonance Part B: Magnetic Resonance Engineering*, 31(4):255–269, 2007.

[103] David Gajan, Aurélien Bornet, Basile Vuichoud, Jonas Milani, Roberto Melzi, Henri A Van Kalkeren, Laurent Veyre, Chloé Thieuleux, Matthew P Conley, Wolfram R Grüning, et al. Hybrid polarizing solids for pure hyperpolarized liquids through dissolution dynamic nuclear polarization. *Proceedings of the National Academy of Sciences*, 111(41):14693–14697, 2014.

[104] Urška Sevšek, Jiří Brus, Karel Jeřabek, and Peter Krajnc. Post polymerisation hyper-crosslinking of styrene/divinylbenzene poly (hipe) s: Creating micropores within macroporous polymer. *Polymer*, 55(1):410–415, 2014.

Acknowledgements

To begin with, I would like to address my full respect and gratitude for the members of my jury: Prof. Sami JANNIN, Prof. Mattias ERNST, Prof. Lothar HELM, and Prof. Sandrine GERBER. You are so special to this thesis that you, together with my advisors, might be the only people that would have gone through this thesis.

I am really grateful to Prof. Geoffrey BODENHAUSEN, my thesis director. I am deeply impressed by his expertise in NMR spectroscopy, his acute judgements in the field of magnetic resonance, and his refined taste in the English language as well as the French. Hardly can I be more grateful for the trust from him: he is always supportive for immature ideas and he always appreciates naive attempts.

I thank immensely my co-advisor Prof. Jean-Philippe ANSERMET. Without his sympathetic understanding, firm support and kind generosity, the evolution of this thesis would have been totally different.

I am much indebted to prof. Sami JANNIN. His perspicacity for the principles of basic physics, his acumen for the interpretation of experimental phenomena, and his mastery in constructing scientific instruments always inspire my admirations. Moreover, he led me to the world of dissolution DNP, guided me through the books and papers of magnetic resonance of the 1960s and 1970s, instructed me on how to struggle with finite elements and advised me thoroughly on the composition of this manuscript. I cannot express enough thankfulness for his farsighted comments, detailed corrections and constructive advices on this thesis.

To Dr. Pascal MIÉVILLE, I want to express much my obligations. I shall always remember the Christmas of 2014, which is the first time in my life that I was invited to spend the Christmas in a Western family. It was also the first time that I felt like at home in Europe.

In Lausanne, I spent most of my working time with the d-DNP team. It is very true that any progress in a complicated discipline like d-DNP depends heavily on team work. I feel thus that I have been very lucky to have the chance to work with them: Dr. Aurelien BORNET, the patient tank driver, who initiated my interests in the NMR pulse programming, and in the *Apricotine*. Dr. Jonas MILANI, the great organiser of St.

Acknowledgements

Martin, the princess of boutin jurassien and the adventurer of Great Siberia. Thank you for your *Damascene*! Dr. Basile Viochoud, the Zombie fighter in Wolfenstein. It is not easy to forget your jokes and your night driving after a fondue aux trois sifflé.

I would like to thank Dr. Roberto BURATTO for his organisation of Italaus and his help when I was changing my apartment in Lausanne, and Dr. Danielle MAMMOLI, my Italian teacher. Thank you for teaching me the Chinese philosophy in Italian style: *Dovremmo amare gli animali, per che sono deliziosi.* Also, many thanks to Dr. Angel-Joachim PEREZ-LINDE and to Dr. Srinivas CHITHALAPALLI for their good company.

I thank Dr. Zhaofu FEI, Dr. Emilia PAUNESCU, Dr. Wei ZHONG and Prof. Paul DYSON for their collaboration and their help. Without their extensive knowledge of organic synthesis, of bench work, and of radical-initiated reactions, the synthesis of porous polarising matrices would have been much more difficult.

I thank also the members at LRM ISIC: Albert HOFSTETTER, Arthur PINON, Baptiste BUSI, Brennan WALDER, Claudia AVALOS, Jasmine VIGER-GRAVEL, Jayasubba YARAVA, Jozef KUBICKI, Federico PARUZZO, Nadia GAULJAUX, and Prof. Lyndon EMSLEY, who all contributed to the nice atmosphere in our corridor.

I cannot forget Béatrice BLIESENER-TONG and Anne Lene ODEGAARD for their kind support in fighting the administration and bureaucracy. I do appreciate the efforts of Anto BARISIC in maintaining the spectrometers and solving hardware issues. I want to greet Annelise CARRUPT, Benjamin KRONENBERG, and Gladys PACHE for their Swiss efficiency in the chemical shop of the BCH. I thank the service of mass spectrometry, Dr. Laure MENIN, Daniel ORTIZ, and Francisco SEPULVEDA, for their help in the analyse after my chemical synthesis. Also my sincere thanks to Gregoire BAROZ for his assistance in electron microscopies.

I have shared my Lausanne period and the first part of my time in Paris working with Estel CANET, who impressed me with her firm determination. I thank her for telling me that there are many other possibilities in our lives apart from the professorships in the academic world.

Although Dr. Diego CARNEVALE and me first met in Lausanne, we did not really have a chance to work together until our relocation in Paris. He is a real expert in the solid-state NMR. Without the opportunity of working with him, the solid-state NMR would still be a region of total mystery in my brain. His considerate suggestions before the Christmas in 2016 will always be of great worth to me.

With Dr. Pavel KADERAVEK I shared my office and apartment in Lausanne. I was happy to meet him again in Paris. The various discussions with him on different cultures, on politics, on religion and secularism, on Tibet, and so forth, have not only widened my vision of Western culture but also urged me to think about my Asian

background.

When it comes to the group members in Paris, I would first like to thank Dr. Philippe PELUPESSY for his detailed examples on the set-up and application of CYTHON for numerical simulation and data visualisation in Linux system. I have also benefited a lot from his rich experience in polarisation transfer between nuclear manifolds.

I cannot thank Dr Daniel ABERGEL enough for his invaluable help in searching for an accommodation in Paris and his wise insight into the stochastic world.

It is my pleasure to have the opportunity to work with the group Paris-en-Resonance: Dr. Fabien FERRAGE, Dr. Guillaume BOUVIGNIES, Dr. Emeric MICLET, Dr. Dennis KURZBACH, Aditya JHAJHARIA, Aude SADET, Emmanuelle WEBER, Julien BOUCLON, Nicolas BOLIK-COULON and Sina MARHABAIE. I thank them deeply for our agreeable atmosphere in the centre of Paris. I would like to thank Sina and Aditya again for the cafés and dinners we have taken together.

I would like to thank all my friends outside the NMR communities in Lausanne and in Paris. They make my four-year Ph.D. life lively and colourful.

在此，特别感谢给予我帮助与支持的费兆福老师，钟伟师兄，薛林师兄。你们的鼓励与开导让我受益良多。

感谢於邱黎阳、夫妇，杨野，罗智、丁晓璇夫妇，赵顺在宁波饭店的陪伴。也不会忘记宁波饭店孙哥孙嫂慰藉莼鲈之思的刀工火候。

同样感谢陈沪相识十年的威士忌，高搏、李晨歌夫妇组织的桌游以及黄潘辉、潘娜的红烧肉，殷晗钧、马老师夫妇的口蘑鸡，王子晴、陈冠名的韭菜盒子、羊肉锅。还有远在千里之外屈艺的炸猪排，余文超的老五烧烤，刘畅的烤肋排，张骏青的椰子鸡，程菲、黄丰夫妇的响油鳝滑，孙西桥的涮羊肉，朱磊的老虎菜，吴雨亭的黄喉、酥肉、耗儿鱼……

最后，我要感谢家人恒久不断的支持：固然时而觉得唠叨，始终十分温暖。

Before to conclude, I feel obliged to thank Skype, 微信. Though my family is ten thousand kilometres away, you make them so close as if the distance never sets us apart.

Paris, 10 May 2017   X. JI

CURRICULUM VITAE

NAME: Xiao
SURNAME: JI

PERSONAL INFORMATION

Gender:	Male
Date of Birth:	1989/06/29
Current Address:	MB612, Ecole Normale Supérieure,
	1 Rue Maurice Arnoux,
	92120 MONTROUGE
Mobile:	(+33) 6 58 36 9 582
Email:	xiao.ji@epfl.ch/xiao.ji@ens.fr

EDUCATION

2014/02 - 2017/08	Ecole Polytechnique Fédérale de Lausanne	Nuclear Magnetic Resonance	Ph. D.
	Thesis Director: Prof. Geoffrey BODENHAUSEN (EPFL, ENS)		
	Prof. Jean-Philippe ANSERMET (EPFL)		
2011/09 - 2013/06	University Paris Sud XI	Organic Chemistry	M. Sc.
2007/09 - 2011/06	Wuhan University	Applied Chemistry	B. Sc.

RESEARCH EXPERIENCE

2014/02 - Present   Ecole Polytechnique Fédérale Lausanne, Lausanne, Switzerland
Position : Research Assistant

- Designed and validated a novel sample formulation for magnetic resonance.
- Built a numerical model to predict the time-dependent dynamics of magnetic polarisation, which directly guides the design of new apparatus of magnetic resonance in our team.
- Created a transportable technology that enhances the sensitivity of NMR/MRI experiments by around 800 times.

2016/04 - 2017/06   École Normale Supérieure, Paris, France
Position : Research Assistant

- Structrual analyse of derivatives of graphene by solid state NMR
- Designed new pulse sequence to study the carbon homonuclear dipolar coupling
- Developed new methodology to study the ^{1}H-^{14}N correlation at 60kHz MAS rate for peptides

2013/01 - 2013/06   Université Paris-Sud XI, Orsay, France
Position : Intern

- Coupled the photochemistry with continuous flow synthesis in microstructured Reactors.
- Improved the temperature control during reaction optimization, which permits the scaling-up the reaction by 10 times via parallel approach.
- Separated the regio-/stereo-isomers by HPLC/UPLC, then perform NMR tests to determine the absolute configuration of intermediates and final products.

133

2012/03 - 2012/07   Université Paul-Sabatier III, Toulouse, France
Position : Intern

- Synthesized the surfactants from natural products.
- Purified the intermediate and final products with preparative reversed-phase chromatography.
- Analysed the physical and chemical properties of the micelles of surfactants in aqueous solution.

TECHNICAL SKILLS

- Theoretical knowledge in magnetic resonance and spin dynamics.
- Set-up multi-dimensional pulse sequences in Bruker database to perform structural elucidation of small molecules in both solid and liquid state.
- Modify existing pulse sequence as well as develop new NMR experiments with Bruker syntax.
- Numerical simulation of macroscopic spin diffusion in solid with finite element method using MATLAB and COMSOL.
- Monte Carlo simulation of local magnetic field in amorphous spin glass with C++.
- Experimental design and statistical analysis of experimental results.
- Quantitative data analysis and data visualisation with Python and Mathematica.
- Microsoft Office and *LaTeX*.
- Working in both Windows and Linux environments

PUBLICATIONS

- D. Carnevale, **X. Ji**, and G. Bodenhausen, *Two-way cross-polarisation for the indirect detection of nitrogen-14 nuclei in magic angle spinning NMR spectroscopy*. In Preparation.
- **X. Ji**, A. Bornet, B. Vuichoud, J. Milani, D. Gajan, A. Rossini, L. Emsley, G. Bodenhausen, and S.Jannin., *Transportable Hyperpolarized Metabolites*. **Nature Communication. 2017,** 8, 13975.
- A. Bornet, A. Pinon, A. Jhajharia, M. Baudin, **X. Ji**, L. Emsley, G. Bodenhausen, J-H.Ardenkjaer-Larsende, and S. Jannin. *Microwave-gated dynamic nuclear polarization.* **Phys. Chem. Chem. Phys., 2016,**18, 30530
- A. Bornet, M. Maucourt, C. Deborde, D. Jacob, J. Milani, B. Vuichoud, **X. Ji**, J-N. Dumez, A. Moing, G. Bodenhausen, S. Jannin, and P. Giraudeau. *Highly Repeatable Dissolution Dynamic Nuclear Polarization for Heteronuclear NMR Metabolomics.* **Anal. Chem., 2016,** 88, 6179
- B. Vuichoud, A. Bornet, F. de Nanteuil, J. Milani, E. Canet, **X. Ji**, P. Miéville, E. Weber, D.Kurzbach, A. Flamm, R. Konrat, A. D. Gossert, S. Jannin, G. Bodenhausen. *Filterable Agents for Hyperpolarization of Water, Metabolites, and Proteins*. **Chem. Eur. J., 2016,** 22, 14696.
- A. Bornet, **X. Ji**, D. Mammoli, B. Vuichoud, J. Milani, G. Bodenhausen, and S. Jannin. *Long-Lived States of Magnetically Equivalent Spins Populated by Dissolution-DNP and Revealed by Enzymatic Reactions*. **Chem. Eur. J., 2014,** 20, 17113.

134